# PROBING THE CHIRAL DOMAIN STRUCTURE AND DYNAMICS IN $SR_2RUO_4$ WITH NANOSCALE JOSEPHSON JUNCTIONS

BY

DANIEL BAHR

DISSERTATION

Submitted in partial fulfillment of the requirements
for the degree of Doctor of Philosophy in Physics
in the Graduate College of the
University of Illinois at Urbana-Champaign, 2011

Urbana, Illinois

Doctoral Committee:

Associate Professor Alexey Bezryadin, Chair
Professor Dale Van Harlingen, Director of Research
Professor Eduardo Fradkin
Assistant Professor Yann Chemla

# Abstract

Previous work on $Sr_2RuO_4$ has shown that the superconducting state is unconventional with an order parameter symmetry of $p_x \pm ip_y$. Measurements using Josephson Interferometry have shown evidence for chiral order parameter domains on the order of 1 $\mu$m in size. To further search for signatures of these domains we have fabricated Josephson junctions on clean $Sr_2RuO_4$ single crystals ($T_c$=1.5 K) ranging from 500 nm to 4 $\mu$m wide. Using an applied magnetic field, we modulated the critical current of the junctions to make phase-sensitive measurements of the order parameter of the p-wave superconductor. We observed critical current characteristics consistent with single and multiple domains being present in the junctions. We also observed hysteresis effects in the junctions similar to previous experimental and theoretical work. We explored field cooling effects in the junctions that showed possible domain wall movement along the face of the junction. We also observed switches in the critical current that are not described currently by known theory and could be an indication of vertically oriented domains. We found that our smallest (500 nm) junctions consistently showed characteristics consistent with single domain junctions and that our results are consistent with 1 $\mu$m domains.

*To my love, Michelle.*

*To dream the impossible dream*

*To fight the unbeatable foe*

*To bear with unbearable sorrow*

*To run where the brave dare not go*

*To right the unrightable wrong*

*To love pure and chaste from afar*

*To try when your arms are too weary*

*To reach the unreachable star*

*This is my quest, to follow that star*

*No matter how hopeless, no matter how far*

*To fight for the right, without question or pause*

*To be willing to march into Hell, for a Heavenly cause*

*And I know if I'll only be true, to this glorious quest,*

*That my heart will lie will lie peaceful and calm, when I'm laid to my rest*

*And the world will be better for this*

*That one man, scorned and covered with scars,*

*Still strove, with his last ounce of courage,*

*To reach the unreachable star.*

*—Don Quixote "Man of La Mancha"*

# Acknowledgments

I would like to first and foremost thank my parents James and Janet, my brother, Brian, and sister, Katie, for their love and support. Without their constant encouragement this entire process would have been much more difficult. I would also like to thank my wife Michelle for her love and extreme patience. Through her I found that sometimes quietness and peace are the greatest road to success.

My advisor Dale van Harlingen has been a wonderful source of inspiration throughout my research. His knowledge and experience has been of inestimable help. His leadership has gone a long way towards keeping me focused and happy while still driving me to work hard. Raffi Budakian has also given me extraordinarily helpful advice and encouragement. I have learned much from him and I appreciate the time he gave me while building up his laboratory here at Illinois. I would also like to thank the members of the DVH research group. First, Martin Stehno for all the training and discussions he has provided. It has truly been an adventure we have taken together. Also, Trevis Crane for teaching me how to operate a dilution refrigerator. Special thanks to Francoise Kidwingira for her excellent discussions and always cheerful advice. And finally thanks to Sergey Frolov, Joel Strand, Micah Stoutimore, Madalina Colci, Ion Moraru, Vladimir Orlyanchik, Juan Atkinson, Chris Nugroho, and Chris English for all your support. You have all made this a wonderful journey and remember to always fix the batteries.

Another wonderful influence in my career has been Eduardo Diazmuñoz, Head of the Opera Department. During my time at Illinois I performed in many productions in the Opera Department and found much inspiration in Maestro Diazmuñoz's leadership. I am

truly lucky to have found someone who believed in me so deeply and gave me such a great opportunity to grow and learn from him.

I would like to thank the other educators I had in my life. Richard Hertel has been a constant inspiration for me both in my vocal training and in helping me finish my doctorate degree. His support and encouragement was always welcome and his knowledge of the process was an excellent help during my years of study and research. I would also like to thank Ricardo Herrera and Dawn Harris for their encouragement and for the opportunities they gave me to perform and learn from them.

I would like to thank my committee for their insightful comments and excellent questions. It was a great experience to get to discuss my research with them and I greatly appreciate the time that they each gave to reviewing my research.

Finally, I would like to thank the staff of the Frederick Seitz Material Research Laboratory for all of their help and advice, especially Doug Jeffers, Mike Marshall, and Tony Banks. The entire staff's skill and attention to detail really keep this facility running. I would also like to thank our funding through DOE grant DEFG02-07ER46453, without which we would not be able to perform our research.

# Table of Contents

# List of Tables

# List of Figures

# Chapter 1

# Introduction

Since its discovery in 1911 by Kamerlingh Onnes [1], superconductivity has been one of the cornerstones of study in Condensed Matter Physics. Kamerlingh Onnes' first studies were on resistanceless current flow in mercury, but many metals were discovered to superconduct at low temperature in the following years. As some metals are cooled, they pass a certain temperature, known as the critical temperature, below which the resistance of the metal will vanish. It took nearly 50 years for a viable theory of superconductivity to be formulated after its discovery.

Ginzburg and Landau (GL) formulated a phenomenological theory of superconductivity in 1950 in Russia [2]. They solved for the free energy of the superconductor and defined a wave function for the system. This was one of the first indications of macroscopic quantum mechanics, essentially the entire superconductor was acting with a single wave function. They also discovered two seminal length scales that still define superconductors. The first is $\xi$ that defines the coherence length of the wave function. The second is $\lambda$, the penetration depth. Superconductors are perfect diamagnets and expel magnetic fields from their bulk, which is known as the Meissner effect. $\lambda$ is the length scale over which the magnetic field can penetrate into the superconductor until it is completely repelled.

Bardeen, Cooper and Schrieffer (BCS) formulated a microscopic theory of superconductivity 7 years after Ginzburg and Landau at the University of Illinois at Urbana-Champaign [3]. Their theory describes how phonons mediate the pairing of electrons. The electrons form Cooper pairs that are of opposite momentum and paired in $k$-space. The theory is specifically for s-wave superconductors, meaning the superconductor has an isotropic energy

gap. This gap forms in its energy spectrum when the metal cools into the superconducting state. For a standard superconductor, this gap is isotropic and well-defined by the BCS theory.

There are also 2 types of superconductors defined by their reaction to magnetic fields. As we stated previously, a superconductor will repel a magnetic field from its bulk, up to a certain critical field. For a Type I superconductor, when the critical field $H_c$ is reached, the superconductor transitions into a normal metal state and superconductivity is lost. For a Type II superconductor, there are two critical fields, labeled $H_{c1}$ and $H_{c2}$. When $H_{c1}$ is reached, it becomes energetically favorable for the superconductor to allow discrete amounts of magnetic field to pass through the bulk, forming what are known as Abrikosov vortices [4]. $H_{c2}$ is the field at which the superconductivity is lost in the Type II superconductor. $H_{c1}$ in Type II superconductors is usually smaller than $H_c$ for Type I superconductors. Conversely, $H_{c2}$ is usually much larger than $H_c$, on the order of a few Tesla.

Recently, new superconductors have been discovered that do not have isotropic energy gaps and are defined by much higher critical temperatures than had previously been found in standard superconductors. GL theory still can describe these new superconductors, however the pairing mechanisms seem to not be exactly the same as in s-wave superconductors, and thus require an as yet undiscovered microscopic theory. The most famous of the unconventional superconductors are the cuprates. The crystal structure of the cuprates contain crystal planes of CuO, such as YBCO, BSCCO, and LSCO. The first cuprate superconductor discovered was Ba-La-Cu-O by Bednorz and Müller [5]. This discovery opened a new field of superconductivity and earned them the Nobel Prize in Physics. The high critical temperature of the cuprates was a mystery as it could not be predicted by any theory at the time. In the years since their discovery, the cuprates have become almost synonymous with unconventional superconductivity. It had been shown that Yttrium Barium Copper Oxide (YBCO) could possibly be a d-wave superconductor [6], specifically having the order parameter symmetry $d_{x^2-y^2}$. Wollman *et al.* then showed experimentally using phase sensitive

SQUID and Josephson Interferometry that this pairing symmetry was indeed correct [7]. This discovery opened the frontier, with much debate, of other order parameter symmetries in superconductors.

In our research group, we have previously studied the unconventional superconductor $Sr_2RuO_4$ [8, 9]. This superconductor has a crystal structure similar to the cuprates, but contains RuO planes instead of CuO. It has many other interesting characteristics which we will explore in Chapter 2. Most notably, it is believed to be a p-wave superconductor. In Chapter 3 we will discuss the Josephson effect and SQUID and Josephson Interferometry in depth. Chapter 4 will outline our sample fabrication technique, which is unique. We have developed a way to fabricate 500 nm to 4 $\mu$m Josephson Junctions on large $Sr_2RuO_4$ single crystals. Finally, in Chapter 5 we will review our experimental findings and discuss the evidence we have found of the existance of chiral domains in $Sr_2RuO_4$.

# Chapter 2

# A Brief History of $Sr_2RuO_4$

Our discussion of $Sr_2RuO_4$ will mostly follow a review written by Yoshiteru Maeno and Andrew Mackenzie [10]. We will attempt to add to the discussion with recent discoveries and further experiments that have been performed to highlight new developments, especially those pertaining to the order parameter domain structure that we believe exists in this crystal.

## 2.1 Crystal Structure and Evidence of Triplet Superconductivity

A superconducting transition was first discovered at Hiroshima University in polycrystalline $Sr_2RuO_4$ below 1K. Initial interest in the crystal revolved around measurements of the de Haas-van Alphen effect [11] but the interest in the crystal quickly grew after Rice and Sigrist suggested that the pairing symmetry of the order parameter could be triplet [12]. $Sr_2RuO_4$ has a perovskite crystal structure with alternating planes of SrO and RuO, similar to the structure of the cuprate LBCO. The superconductivity is believed to be in the RuO planes and thus we label these planes as the *ab*-plane as seen in Figure 2.1.

The normal state properties of $Sr_2RuO_4$ may offer us a little insight into its superconducting properties, so we will summarize them for completeness. $Sr_2RuO_4$ is metallic above its critical temperature and the metal is a strongly two-dimensional Fermi liquid. The Fermi surface has three slightly corrugated sheets as seen in Figure 2.2. The $\alpha$ sheet is the dark

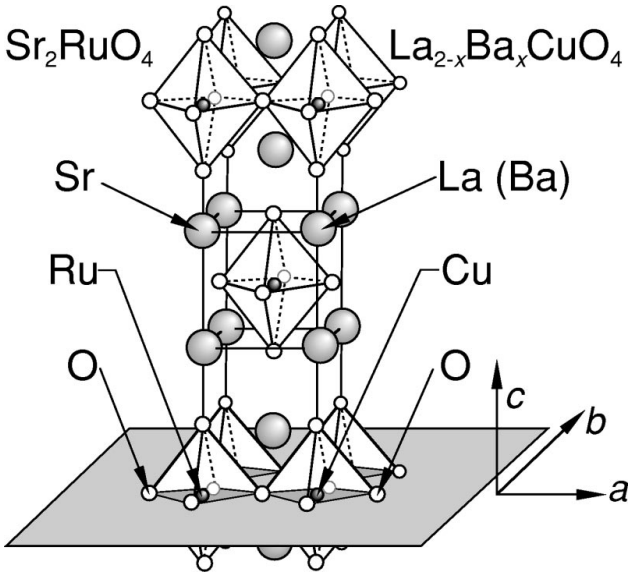


Figure 2.1: Perovskite crystal structure of $Sr_2RuO_4$. From [10]

cylinders on the corners. The $\beta$ sheet is the central pillar and is nested in the $\gamma$ sheet [10]. The corrugation has been enhanced in the figure to better show the effect. The actual deviations are actually tiny compared to a perfect cylinder. There is also significant mass enhancement, especially in the $\gamma$ sheet, where it can be as much as $16m_e$ [13].

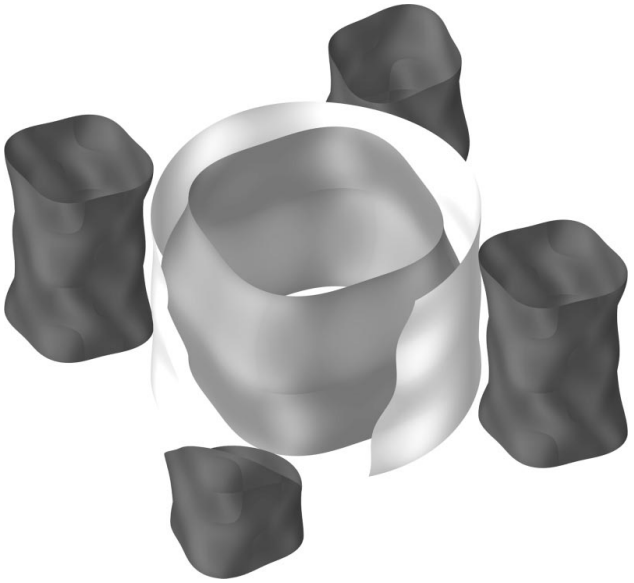

Figure 2.2: Fermi Surfaces of $Sr_2RuO_4$. The two electron sheets are nested in the center with the four hole pockets around the outside. The corrugation of the sheets have been exaggerated for effect. From [10]

As stated above, the superconducting transition was first discovered to be below 1K, but as the crystal quality increased, the critical temperature, $T_c$, eventually rose to around 1.5K for pure single crystals. The first suggestion of spin triplet pairing in $Sr_2RuO_4$ came from a paper by Rice and Sigrist [12] based on its similarity to liquid $He^3$. They suggested that NMR Knight shift measurements would show the triplet pairing and Ishida *et al.* performed such an experiment [14]. We can see from Figure 2.3 that the spin-singlet result that is traced by the dotted and dashed lines is not followed below $T_c$ of the crystal. In fact, both oxygen sites measured in this experiment show no suppression of their spins when they enter the superconducting state, a fairly clear sign of spin-triplet pairing in $Sr_2RuO_4$.

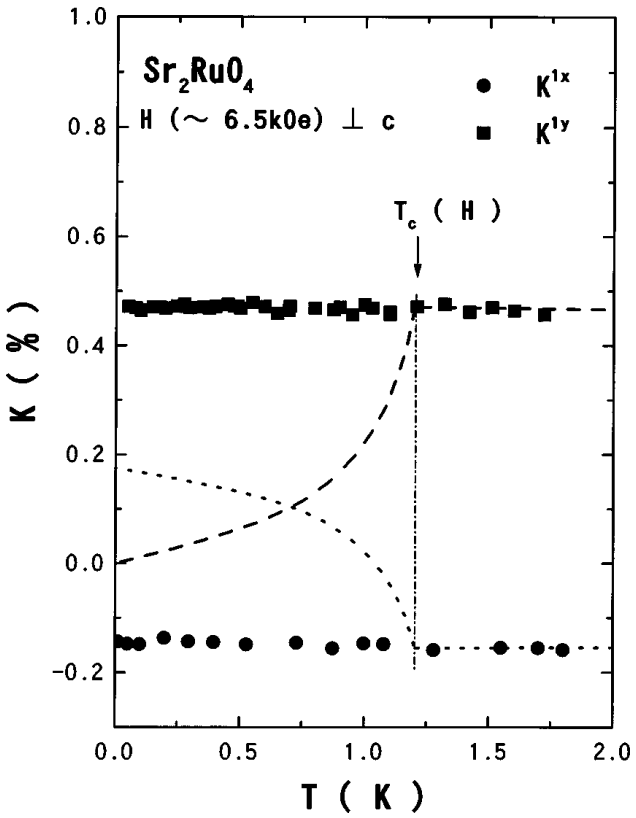


Figure 2.3: Knight Shift data from two Oxygen Sites in $Sr_2RuO_4$. Crystal is cooled through $T_c$ as marked on graph. The dashed and dotted lines represent expected behavior for spin-singlet Knight Shift response. From [14].

The other indicator that pointed toward a spin-triplet order parameter was based in the fact that $Sr_2RuO_4$ is very susceptible to non-magnetic impurities. In the cuprates and s-wave superconductors, this fact is generally not true, but one would not expect them to be as susceptible because they are uneffected by elastic scattering [15]. However, elastic scattering is very detrimental to a spin-triplet superconductor. Mackenzie *et al.* studied this problem by adding non-magnetic impurities to $Sr_2RuO_4$ crystals and saw a significant decrease in $T_c$ as shown in Figure 2.4. The data also gives a predicted upper $T_c$ of 1.5K [16, 17].

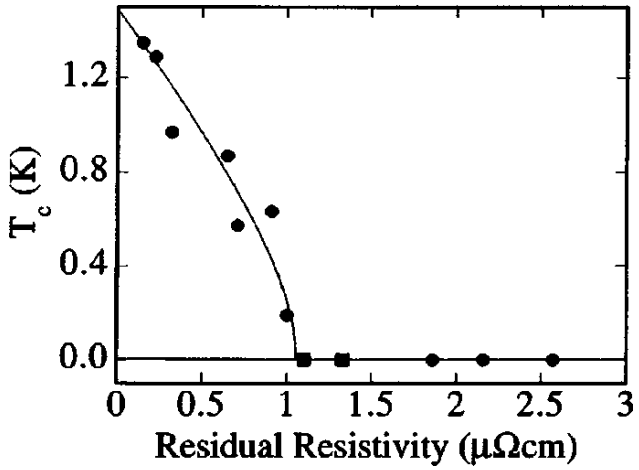


Figure 2.4: There is a significant decrease in the critical temperature of $Sr_2RuO_4$ when elastic scatterers are added to the crystal. The data also predicts a maximum $T_c$ of 1.5K [16, 17].

What we see from these experiments is a clear picture of a crystal with a new type of superconductivity. Its analogue to $He^3$ gives us an extraordinary head start on understanding this superconductor. Let us continue by further characterizing the supderconducting state based on the experiments that have been carried out with respect to the order parameter symmetry.

## 2.2 TRS Breaking and Chiral Domains

Superconductors are generally defined by their order parameter, $\Delta(\mathbf{k})$, which describes the pairing in the condensate. For s- and d-wave superconductors this expression is sufficient

definition, as $\Delta_{\uparrow\uparrow} = \Delta_{\downarrow\downarrow} = 0$ and $\Delta_{\uparrow\downarrow} = \Delta_{\downarrow\uparrow} = \Delta_s$, meaning there is only pairing for opposite spin states in k-space. For spin-triplet, we have pairing of same spin states, thus $\Delta_{\uparrow\downarrow} = \Delta_{\downarrow\uparrow} = \Delta_0$. This allows us to define a $d$-vector as follows:

$$\Delta(\mathbf{k}) = \begin{bmatrix} \Delta_{\uparrow\uparrow} & \Delta_0 \\ \Delta_0 & \Delta_{\downarrow\downarrow} \end{bmatrix} = \begin{bmatrix} -d_x + id_y & d_z \\ d_z & d_x + id_y \end{bmatrix} \tag{2.1}$$

where $\mathbf{d}(\mathbf{k}) = [d_x(\mathbf{k}), d_y(\mathbf{k}), d_z(\mathbf{k})]$ is the general form of the $d$-vector [10]. The direction the $d$-vector points is perpendicular to the the equal spin pairing, so it is a convenient way of defining the order parameter in p- and f-wave superconductors. However, we caution the reader that using the term $d$-vector in no way implies d-wave superconductivity and is simply a term that has unfortunately become the standard vector term to describe the pairing state.

There are many states that are possible for a p-wave superconductor and most are defined by the direction of $\mathbf{d}(\mathbf{k})$. Mackenzie and Maeno list the possibilities in a table in their review that is replicated in Table 2.1. We can see from this table that determining the direction of $\mathbf{d}(\mathbf{k})$ along with whether it is unitary and if time-reversal symmetry is broken should be sufficent to define the state. However, the previous experiments performed on the crystal, namely the Knight shift NMR experiment, are not in themselves sufficient to define the direction of $\mathbf{d}(\mathbf{k})$. Mackenzie and Maeno point out that the Knight shift is unchanged when B$\|ab$ implies that $\mathbf{d}(\mathbf{k})$ is along the c axis [10]. Mackenzie and Maeno go further and argue that it is most likely to be a Unitary state due to the larger condensation energy of such states for weak coupling and in the absence of any symmetry-breaking fields [10]. Thus, we narrow the field to one of a few choices in Table 2.1.

Some of the states in Table 2.1 include Time-reversal Symmetry (TRS) breaking, which is usually thought of as a magnetic effect. One might expect, then, that as the superconductor is cooled through $T_c$ the crystal would obtain a magnetic moment. However, the Meissner effect cannot be violated in a superconductor by small fields, so there will be screening

| Unitary states | | | | |
|---|---|---|---|---|
| $\mathbf{d}/\Delta_0$ | $\Delta/\Delta_0$ | Node | Time-reversal symmetry | $^3$He |
| $\hat{\mathbf{x}}k_x + \hat{\mathbf{y}}k_y$ | $\sqrt{k_x^2+k_y^2}$ | | | BW |
| $\hat{\mathbf{x}}k_y - \hat{\mathbf{y}}k_x$ | $\sqrt{k_x^2+k_y^2}$ | | | |
| $\hat{\mathbf{x}}k_x - \hat{\mathbf{y}}k_y$ | $\sqrt{k_x^2+k_y^2}$ | | | |
| $\hat{\mathbf{x}}k_y + \hat{\mathbf{y}}k_x$ | $\sqrt{k_x^2+k_y^2}$ | | | |
| $\hat{\mathbf{z}}k_x$ | $\lvert k_x\rvert$ | line | | |
| $\hat{\mathbf{z}}(k_x + k_y)$ | $\lvert k_x + k_y$ | line | | |
| $\hat{\mathbf{z}}(k_x \pm ik_y)$ | $\sqrt{k_x^2+k_y^2}$ | | broken | ABM |
| Nonunitary states | | | | |
| $\hat{\mathbf{x}}k_x + i\hat{\mathbf{y}}k_y$ | $\lvert k_x + k_y\rvert \uparrow\uparrow$ | | broken | |
| | $\lvert k_x - k_y\rvert \downarrow\downarrow$ | | | |
| $\hat{\mathbf{x}}k_y - i\hat{\mathbf{y}}k_x$ | $\lvert k_y - k_x\rvert \uparrow\uparrow$ | | broken | |
| | $\lvert k_x + k_y\rvert \downarrow\downarrow$ | | | |
| $\hat{\mathbf{x}}k_x - i\hat{\mathbf{y}}k_y$ | $\lvert k_y - k_x\rvert \uparrow\uparrow$ | | broken | |
| | $\lvert k_x + k_y\rvert \downarrow\downarrow$ | | | |
| $\hat{\mathbf{x}}k_y + i\hat{\mathbf{y}}k_x$ | $\lvert k_x + k_y\rvert \uparrow\uparrow$ | | broken | |
| | $\lvert k_y - k_x\rvert \downarrow\downarrow$ | | | |
| $(\hat{\mathbf{x}} + i\hat{\mathbf{y}})(k_x + k_y)$ | $2(\lvert k_x + k_y\rvert) \uparrow\uparrow$ | line | broken | |
| | $0 \downarrow\downarrow$ | | | |
| $(\hat{\mathbf{x}} + i\hat{\mathbf{y}})(k_x + ik_y)$ | $2\sqrt{k_x^2+k_y^2} \uparrow\uparrow$ | | broken | A1 |
| | $0 \downarrow\downarrow$ | | | |

Table 2.1: Reprint of allowed $p$-wave states on a cylindrical Fermi Surface. From [10, 12, 18]

currents in the superconductor and the bulk of the sample will still see no magentic field. Similar to a magnetic crystal, the superconductor could form domains to reduce the energy of the circulating fields required to suppress the magnetic moment. However, due to defects in the crystal, there will also be a small magnetic moment that can be detected [18].

The first experiment that was performed to determine if $Sr_2RuO_4$ breaks TRS was muon spin rotation ($\mu$SR). The experiment essentially implants muons into the crystal, and then the muons decay into positrons, and the positrons are emitted in a direction that correlates to the magnetic spin at the implantation site [19, 20]. Luke *et al.* found a normal distribution of dipole moments, but then also found an extra relaxation that appeared around $T_c$ of the crystal, as shown in Figure 2.5. When the muon beam was applied perpendicular to the c-axis and a 50 G magnetic field was applied inplane, the effect was completely suppressed,

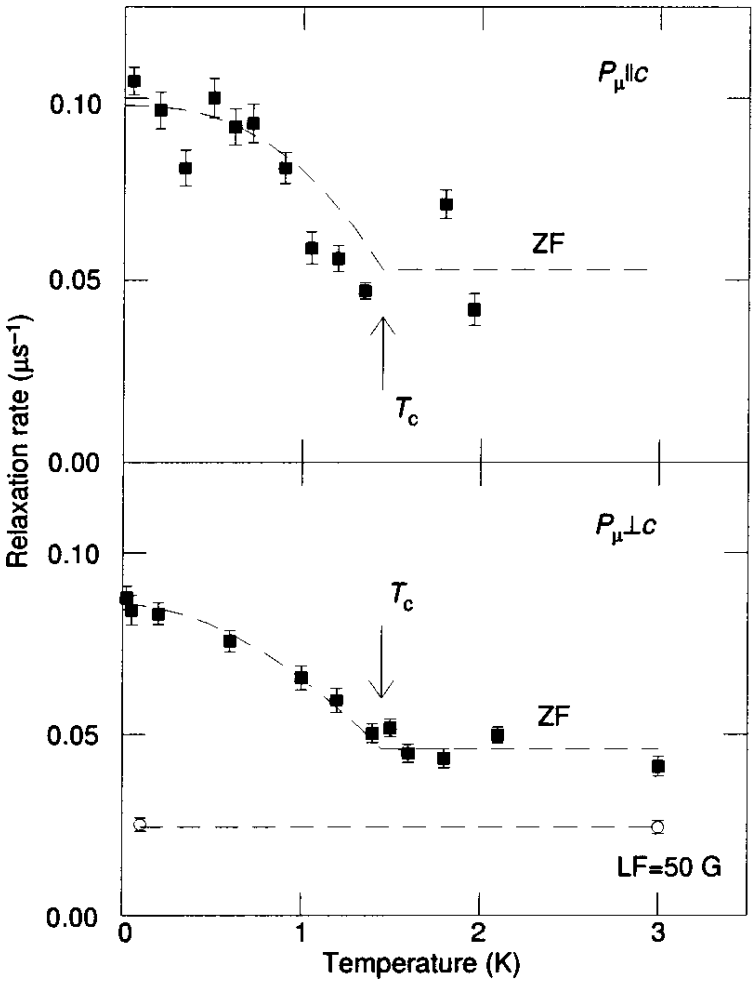


Figure 2.5: Muon spin relaxation of $Sr_2RuO_4$ as it is cooled through $T_c$. Data is from beams incident both perpendicular and parallel to the c-axis. On the perpendicular graph, there is also data from a suppressing field being applied in the *ab*-plane. From [19].

adding more weight to the idea that the spins are in the RuO planes of the crystal. The signal can be interpreted as coming from spontaneous moments in the crystal, and are a sign that there is TRS-breaking in the crystal [19, 20]. They also report that there were signs of local imperfections in the spin signal which could come from domain walls in the crystal. The domains were on the order of 2 $\mu$m in size or less.

More recently, Xia *et al.* performed Polarized Kerr Effect (PKE) measurements on high quality single crystals of $Sr_2RuO_4$. PKE is specifically sensitive to TRS-breaking and was an ideal system for searching for this effect after the $\mu$SR experiments. Figure 2.6 shows the onset of a symmetry breaking signal at $T_c$ of the crystal. This signal unambiguously

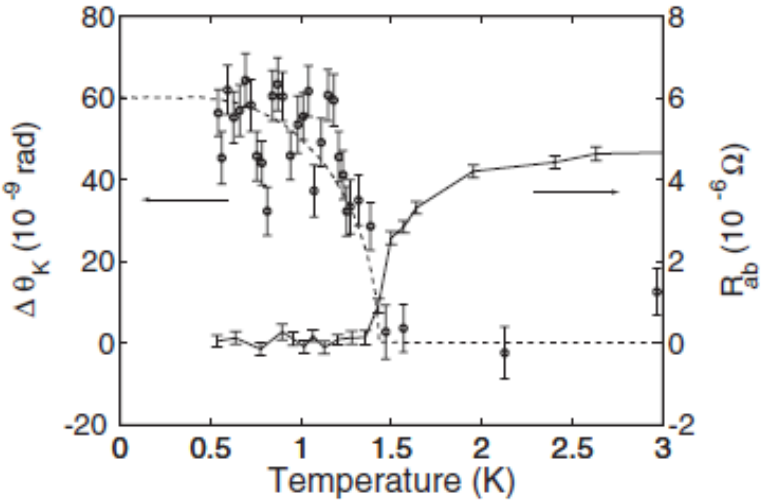


Figure 2.6: Polarized Kerr Effect measurement on zero-field cooled $Sr_2RuO_4$. There is also an electrical measurement of the crystal to show the onset of superconductivity. From [21].

displays TRS-breaking in $Sr_2RuO_4$, however they also found something even more telling. Using an applied field, they were able to train the chirality of the signal either positive or negative, showing the possible existance of chiral domains in the system [21]. However, this experiment sets the possible chiral domain size at $>50$ $\mu$m, where the $\mu$SR system predicts much smaller.

Based on these experiments, the best fit for a the $d$-vector representation is $\mathbf{d}(\mathbf{k}) = \hat{\mathbf{z}}[k_x \pm ik_y]$. This vector is the current agreed upon representation for $Sr_2RuO_4$ in the literature and fits the models and experiments the best at this point in time.

Another development that has added some weight to the argument against domains is measurements of $Sr_2RuO_4$ using a scanning SQUID microscope. A SQUID (Superconducting QUantum Interference Device) is a very sensitive flux detector, and with a fixed pickup loop, is thus a very sensitive magnetometer. The pickup loop is scanned across the surface of the crystal and any penetrating magnetic field can be detected by the SQUID. Kathryn Moler's group at Stanford has lead in this effort and have a series of measurements attempting to constrain the size of the domains [22, 23, 24]. Figure 2.7 shows a scan of a $Sr_2RuO_4$ crystal taken using a SQUID with a pickup loop of 3.2 $\mu$m. Using the results of Matsumoto and

Sigrist [25], they calculate that the domains should have induction peaking of 10 to 20 G [24]. They see no signal consistent with this and constrain the size of periodic domains to 0.5 $\mu$m and much smaller if the domains are random. There is, however, some anomolous alignment of the vortices in lines parallel to the crystal edge, as shown in Figure 2.7. It is possible that the order of magnitude of the surface fields could be much smaller than calculated by Matsumoto and Sigrist which would make their detection nearly impossible to detect using current SSM technology.

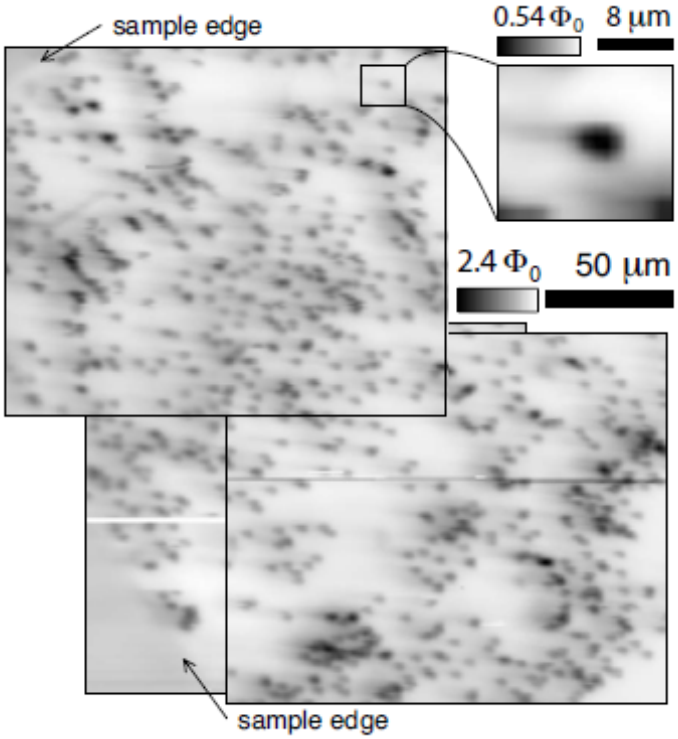


Figure 2.7: Scanning SQUID image of vortices in $Sr_2RuO_4$. There is a lack of signal consistent with a domain structure in the crystal. From [24].

## 2.3 Spin Currents and Half-Quantum Vortices

In recent years there has been increased interest in Majorana quasiparticles and topologically protected states as they pertain to quantum computation. Specifically in $Sr_2RuO_4$, such a state is possible due to its spin-triplet pairing and more specifically due to its $p_x \pm ip_y$ order

parameter symmetry. Such a state would manifest as a half quantum vortex (HQV) due to the possibility of energy being in both the current and a spin current. Such states were proposed for the $^3$He A-phase [26, 27] and since $Sr_2RuO_4$ is a possible analogue to that system, it is also possible that such states exist in this crystal.

Jang *et al.* recently performed measurements on small crystals of $Sr_2RuO_4$ to search for such states, along with looking for circulating currents due to domains. The measurements are performed using cantilever magnetometry, where the crystal is glued to the end of a cantilever as shown in Figure 2.8. The cantilever's natural frequency is extremely sensitive to the dipole moment of the crystal. The cantilever is driven at its natural frequency and changes in the the drive are proportional to the dipole moment [28].

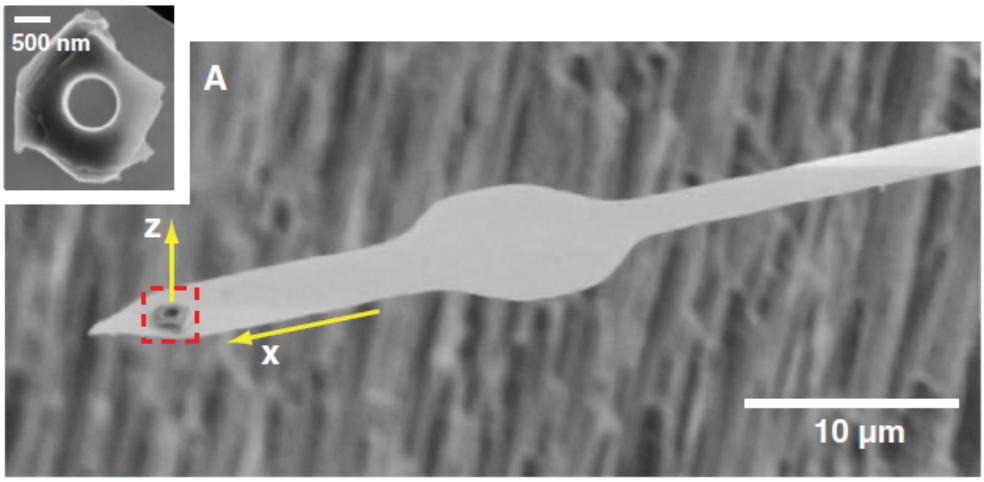


Figure 2.8: Electron Microscope image of a cantilever with a $Sr_2RuO_4$ crystal glued to the end. Magnetic field application axes are as shown. From [28].

Figure 2.9 shows the evolution from a single vortex entering the hole in the crystal to HQV entry. They further explain that the application of an inplane field helps to differentiate the inplane spins, increasing the population of one over the other. With this imbalance, HQVs are more likely to form, and thus they see half steps in their data [28].

Overall, what we have observed is there are many interesting features exhibited by $Sr_2RuO_4$, namely spin-triplet pairing, signatures of chiral domains and the nucleation of half quantum vortices. In the next section we will discuss Josephson Interferometry, and

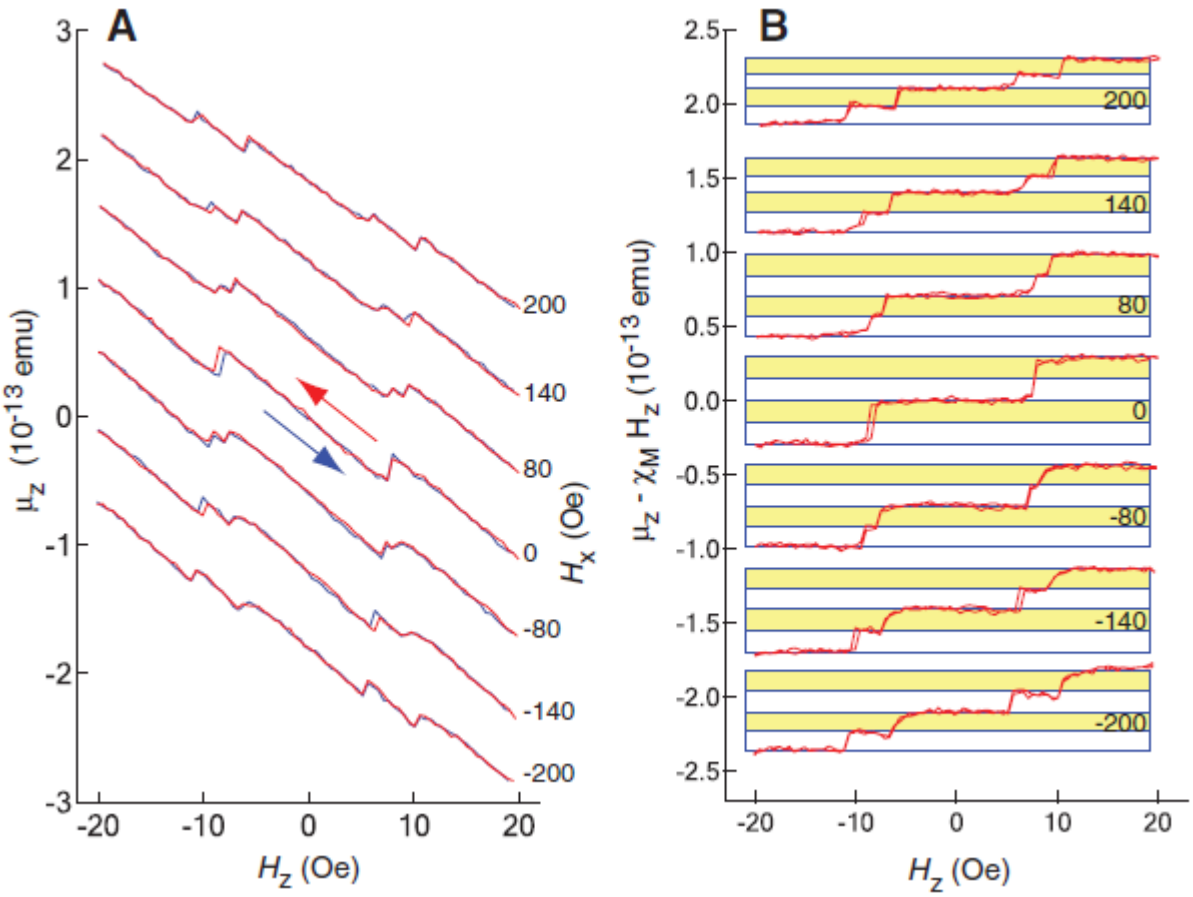


Figure 2.9: Data showing HQV evolution in $Sr_2RuO_4$ as a c-axis field is applied. (B) shows Meissner subtracted data with lines showing half and full vortex steps. Each curve indicates a different amount of in-plane field, as indicated on the left side of the graphs. From [28].

by extension SQUID Interferometry. This is the technique we will use to search for domain structures in $Sr_2RuO_4$, but on a much smaller scale than previously studied.

# Chapter 3

# Josephson Interferometry

As we have stated previously, the main thrust of this research project was to use Josephson junctions as a means to search for domain structure in $Sr_2RuO_4$. In this chapter, we will briefly discuss the physics of the Josephson effect, specifically how it relates to measuring phase in an unknown superconductor. This type of measurement has been termed Josephson Interferometry and was first proposed by Geshkenbein and Larkin [29] and Leggett [7] for axial p-wave superconductors and then later by Sigrist and Rice [30] as an experiment for d-wave. We will also explore experiments using this technique on $Sr_2RuO_4$ performed by Nelson [31] and Kidwingira [8].

## 3.1 Josephson Junctions in Magnetic Field

We shall follow the formalism set out by Barone and Paterno in their book [32], but we will paraphrase heavily to highlight the important aspects of the Josephson effect without clouding the specific effects we are looking to use in our experiments. For a more formal treatment, I would encourage Barone and Paterno's book to the reader.

In Figure 3.1 we have set out the problem. We have two superconductors that are weakly coupled by a barrier. The barrier can be of many different types of materials, such as an insulator(SIS), pure metal(SNS), a ferromagnet(SFS), or a superconducting "pinch"(Ss'S). In all these cases, the tunneling through the barrier may be slightly different, but the essential point is that the wave function of the two superconductors overlaps in the barrier, facilitating the tunneling of electrons. For our understanding of the Jospehson effect, let us assume the

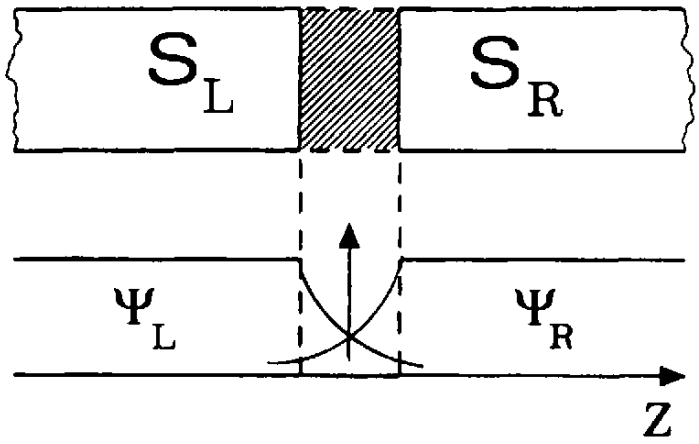


Figure 3.1: Schematic of a typical Josephson Junction. The wavefunction overlaps in the barrier, leading to a tunneling potential across the barrier. From [32].

barrier is insulating. However, in the experiments we undertake in Chapter 5, the junctions are normal metals. An SNS junction will act in a similar fashion to a resistively shunted SIS junction, and their critical current characteristics are identical.

Brian Josephson [33] postulated the following equation for the current passing through the barrier

$$I_s = I_c \sin \phi \tag{3.1}$$

where $I_s$ is the 1-dimensional supercurrent, $I_c$ is the critical current above which the junction becomes normal, and we define $\phi$ as the gauge invariant phase across the junction

$$\phi = \Delta\varphi - \left( \frac{2\pi}{\Phi_0} \int \mathbf{A} \cdot ds \right) \tag{3.2}$$

$\Delta\varphi$ is the phase difference between the two superconductors, $\varphi_L - \varphi_R$. $\mathbf{A}$ is the usual vector potential and $\Phi_0 = h/(2e)$ is the flux quantum. This is the basic form of the Josephson effect and without magnetic fields a supercurrent will flow across the junction with an applied DC voltage $V$ such that

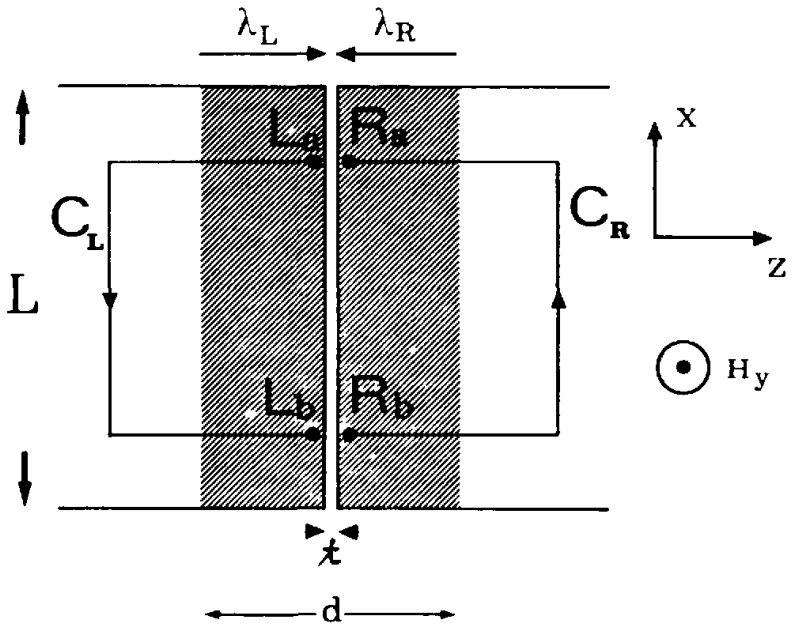


Figure 3.2: Schematic for contour integration when a magnetic field is applied to the Josephson Junciton. The field is applied out of the plane and penetration depth of each superconductor is as marked. From [32].

$$I_s = I_c \sin\left(\varphi_0 + \frac{2\pi}{\Phi_0} V t\right) \tag{3.3}$$

which we get from integrating $\frac{\partial \varphi}{\partial t} = \frac{\pi V}{\Phi_0}$ and subbing into Equations (3.2) and (3.1). This is known as the AC Josephson effect and the frequency associated with Equation (3.3) is called the Josephson frequency, where $\omega = \frac{2\pi V}{\Phi_0}$. This frequency is usually in the microwave regime and can produce Shapiro steps in the current versus voltage (I-V) characteristic of the junction.

When a uniform magnetic field $H$ is applied to the junction, we can write the phase difference across the junction as

$$\nabla \varphi_{L,R} = \frac{2e}{\hbar c}\left(\frac{mc}{2e^2\rho}\mathbf{J}_S + \mathbf{A}\right) \tag{3.4}$$

and our vector potential $\mathbf{A}$ has the usual relation to the applied field $\nabla \times \mathbf{A} = \mathbf{H}$. If we integrate along the contours in Figure 3.2 we get

$$\varphi_{Ra}(x) - \varphi_{Rb}(x+dx) = \frac{2e}{\hbar c}\int_{C_R}\left(\mathbf{A} + \frac{mc}{2e^2\rho}\mathbf{J}_S\right)\cdot\mathbf{dl} \tag{3.5}$$

$$\varphi_{Lb}(x+dx) - \varphi_{La}(x) = \frac{2e}{\hbar c}\int_{C_L}\left(\mathbf{A} + \frac{mc}{2e^2\rho}\mathbf{J}_S\right)\cdot\mathbf{dl} \tag{3.6}$$

Assuming that the penetration depth is shorter than the film thickness, which is generally the case, the contour can extend outside that length as noted in Figure 3.2. Combining this with the assumption that the barrier is small, we have

$$\varphi(x+dx) - \varphi(x) = \frac{2e}{\hbar c}\oint \mathbf{A}\cdot\mathbf{dl}$$

From our definition of $\mathbf{A}$ we can rewrite the integral as

$$\oint \mathbf{A}\cdot\mathbf{dl} = H_y(\lambda_L + \lambda_R + t)dx$$

where t is the thickness of the barrier and $\lambda_L$ and $\lambda_R$ are the London penetration depth of the two superconductors. Thus, we have have the differential equation

$$\frac{d\varphi}{dx} = \frac{2e}{\hbar c}(\lambda_L + \lambda_R + t)H_y \tag{3.7}$$

We can then define $d = (\lambda_L + \lambda_R + t)$. We can now integrate Equation (3.7) and substitute into the 2 dimensional version of Equation (3.1) to get

$$\varphi = \frac{2e}{\hbar c}dH_y x + \varphi_0$$

$$J = J_c \sin\left(\frac{2e}{\hbar c}dH_y x + \varphi_o\right) \tag{3.8}$$

which is the standard form of the Josephson current density.

We can solve this equation analytically for two different, fairly standard forms of a

junction. The first is a normal, single junction of width L in a static, uniform field H as pictured in Figure 3.2. In this case, the solution is

$$I_1(H) = I_1(0) \left| \frac{\sin \pi \frac{\Phi}{\Phi_0}}{\pi \frac{\Phi}{\Phi_0}} \right| \tag{3.9}$$

where $\Phi = HLd$. This equation gives rise to the pattern shown in Figure 3.3a and since its form is the same as optical interference, we call this a Fraunhofer pattern.

The other standard solution is two junctions that are multiply connected, which is also called a Superconducting QUantum Interference Device (SQUID), as we discussed previously. The solution here is slightly different and takes the form

$$I_{SQUID} = 2I_1 \left| cos\pi \frac{\Phi_\ell}{\Phi_0} \right| \tag{3.10}$$

where $\Phi_\ell$ is the flux contained in the superconducting loop. A graphical solution is given in Figure 3.3b. This solution is an analog to the double slit diffraction pattern in optical interference.

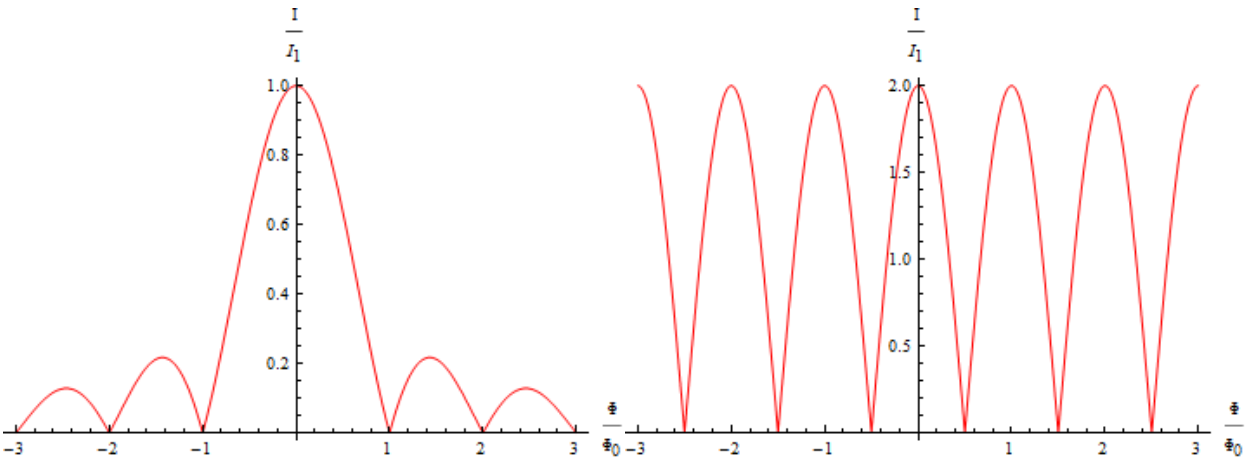


(a) Single Junction (b) SQUID

Figure 3.3: Solutions of Equations (3.9) and (3.10)

## 3.2 SQUID and Corner Junction Geometries and Measurements

Now that we have a basic understanding of the Josephson effect, we can discuss Josephson Interferometry. As we can see from Equations (3.1) and (3.2), if there is a phase difference along the junction, or in the case of a SQUID, between the the two junctions, it will be detectable since the current is sensitive to phase. Let's first look at the SQUID geometry.

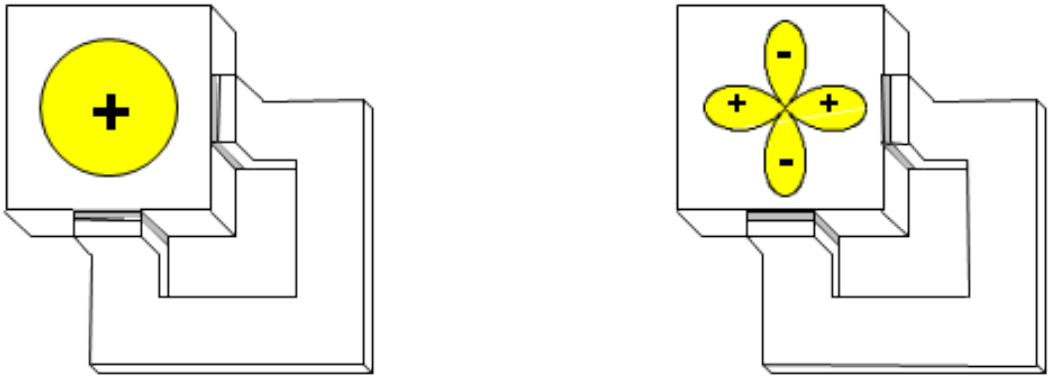


(a) (b)

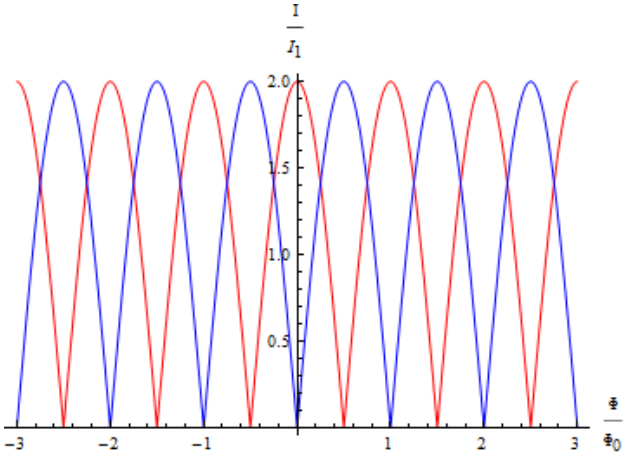


(c)

Figure 3.4: (a) and (b) SQUID Interferometer geometry for 2 different types of superconductors. (c) Red trace is an s-wave (a) superconductor. Blue trace is a d-wave ($\pi$ shifted, (b)) superconductor.

The junctions of the SQUID Interferometer are different faces of the crystal and any difference in the phase they tunnel into in k-space will be evident. However, this method of interferometry can suffer greatly from background fields. The superconducting loop is sensitive to any background fields, therefore extremely good shielding is required. The usual method for making measurements using this method is to make multiple SQUIDs on a single crystal, some that span crystal faces and others that are on the same face to identify whether there is a phase shift in the SQUID.

Another aspect of this measurement system is it usually requires taking data at multiple temperatures. As the system is cooled, there is a slight phase shifting in the SQUID. By taking multiple traces at various temperatures, one can then identify the phase shift in the junction. As this may not be entirely clear, let us look at a SQUID Interferometry measurement taken by Nelson *et al.* on $Sr_2RuO_4$ as an example.

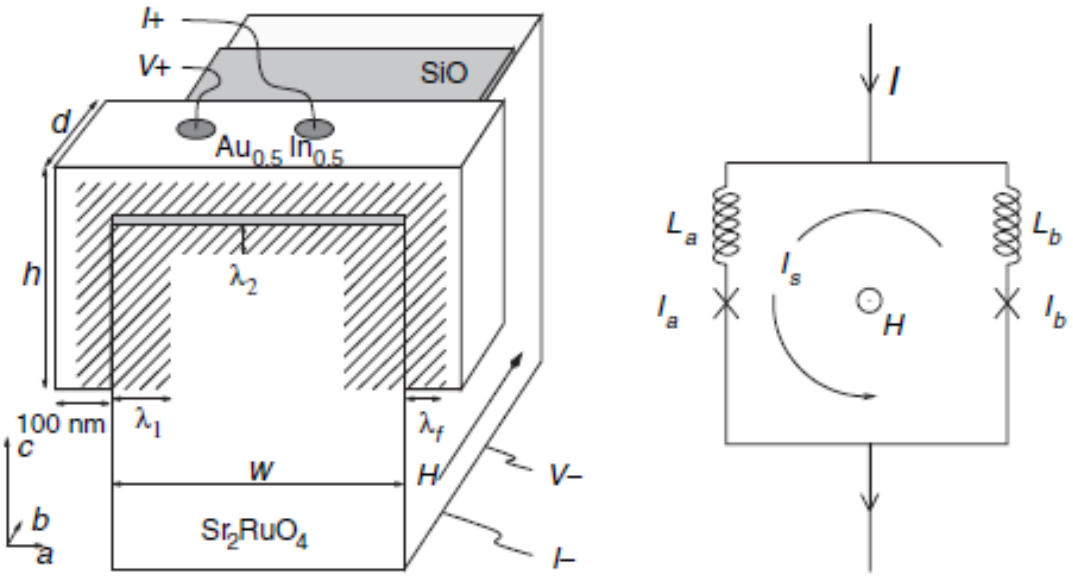


Figure 3.5: Design details of a SQUID Interferometer deposited on $Sr_2RuO_4$. The junctions are on the sides of the crystal with the top of the crystal insulated by SiO. The metal deposited to form the junctions is 1:1 AuIn. The shaded regions indicate the penetration depth of each superconductor, giving an indication of the size of the SQUID loop. A schematic is shown for clarity. From [31].

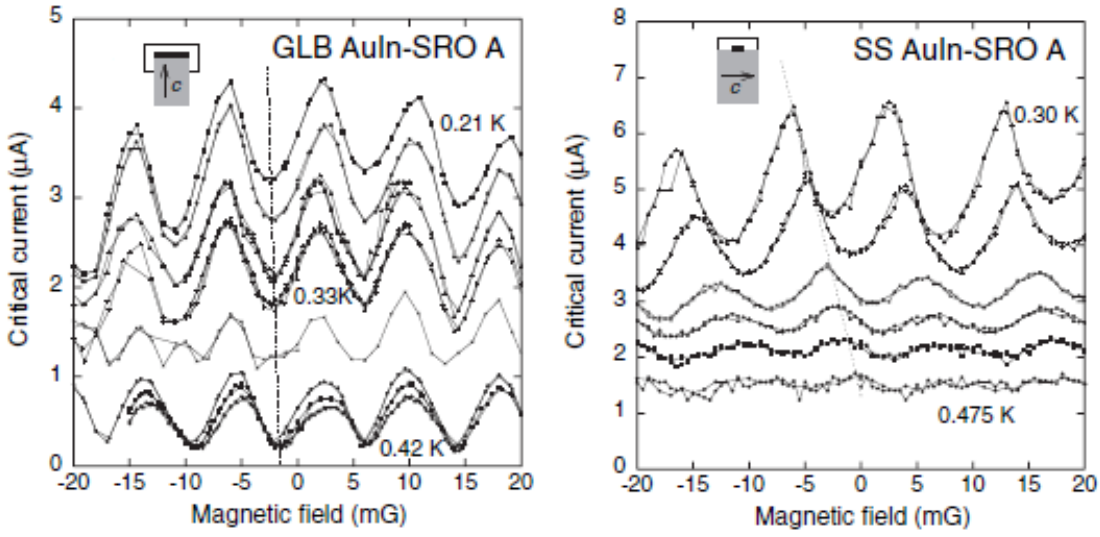


Figure 3.6: Data taken by Nelson *et al.* [31] on SQUID Interferometer. Both a SQUID spanning the sample (left) and a single side SQUID (right) were measured. From [31].

As shown in Figure 3.5, the junctions are on either side of the crystal and the top of the crystal is insulated to form a loop. There are leads on the metal film and the crystal to facilitate measuring the voltage and applying current. The junctions are all fairly large, on the order of 0.5 mm $\times$ 0.5 mm. The reasoning behind the placement of the junctions is that for p-wave superconductors, the lobes of opposite sign are at 180° rather than 90° as in d-wave superconductors.

From the data in Figure 3.6 they show that for junctions on opposite sides of the crystal the minimum of the critical current extrapolates to zero, whereas the junctions that are on the same side have a peak that extrapolates to zero. This is similar to Figure 3.4c. It is interesting to note that the lines do not come perfectly to zero, nor do they show a histogram in their paper of multiple samples showing similar results. Similar SQUID Interferometry studies usually will have a histogram of some sort to show the distribution of these lines around zero to establish that the data is in fact indicating a phase shift [7, 34] and that there isn't trapped flux or that the authors were very fortunate in their data taking. These data are a good indication that there is some phase change across the crystal, but without

more statistics, it seems clear that a single SQUID Interferometry measurement does not uniquely describe the phase information in the unknown crystal.

Let us now look at a different type of measurement that involves a single Jospehson Junction. We will begin by considering a Josephson Junction on the corner of an unknown crystal. For an s-wave superconductor as depicted in Figure 3.7a, there should be no difference and we will see the same Fraunhofer pattern as a normal Josephson Junction. If there is a phase difference between the two faces, then we expect something different. Let us assume the unknown crystal is a d-wave superconductor. In this case, we obtain a dip in the critical current at zero field due to interference between the phases into which the junction is tunneling, as shown in Figure 3.7c. Therefore, we have a technique that is extremely sensitive to the phase of an unknown crystal, but unlike SQUID Interferometry, we can obtain the information directly from the critical current characteristic of the junction. This fact is true whether or not the junction is a corner junction or an edge junction.

## 3.3 Simulations of Junctions

Before we move on to our experiment, we wish to explore some standard solutions to the domain picture that has been proposed by Kidwingira *et al.* and others [8, 35]. The junctions we will be using are all edge junctions, but they are still sensitive to the phase across the junction, similar to the corner junction. Therefore, if there are phase changes associated with the domain structure or the chirality of the crystal, we should be able to observe it. Kidwingira *et al.* proposed that the domains are on the order of 1-10 $\mu$m [8] and were able to see some dynamics that they believed originated from both their existance and movement of the domain walls. These assertions were supported by Bouhon and Sigrist [35], and it is this theory we will briefly explore in this first section.

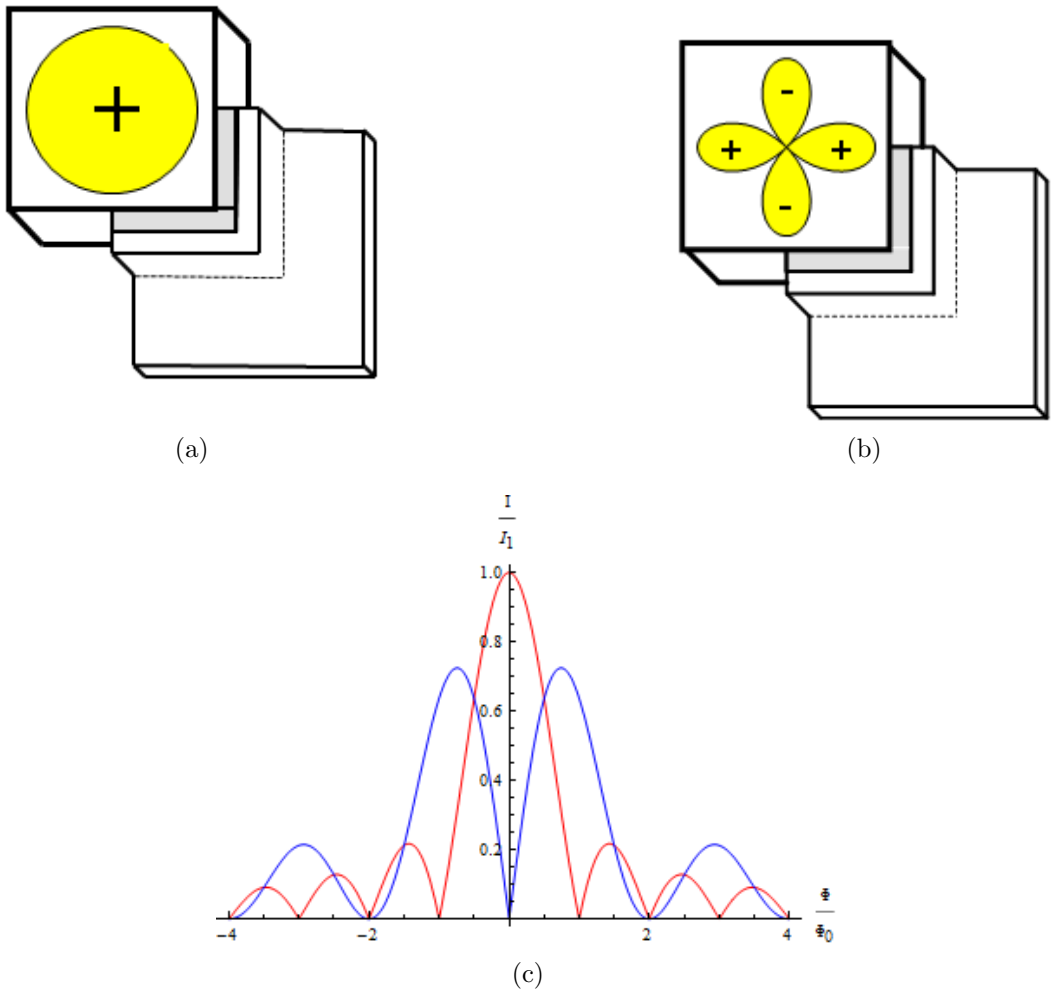


(a) (b) (c)

Figure 3.7: (a) and (b) are examples of corner junctions on s- and d-wave superconductors. (c) Critical current characteristic of s-wave (Red) and d-wave(Blue) Junction.

### 3.3.1 The Effect of Chiral Domains on Larger Junctions

Bouhon and Sigrist setup the problem of the domains such that the walls come in nearly perpendicular to the junction barrier, and they define a chirality to each side of the junction, as in Figure 3.8. They treat the phase drop across the junction as a step function, as the junctions Kidwingira *et al.* used were on the order of 50-80 $\mu$m wide and nearly 100 $\mu$m tall [8, 9], thus containing many domains.

They solve the free energy of this system and discover that there are metastable states that could allow the domain walls to rotate slightly around a pinning point, and thus change the phase drop across the domain wall.

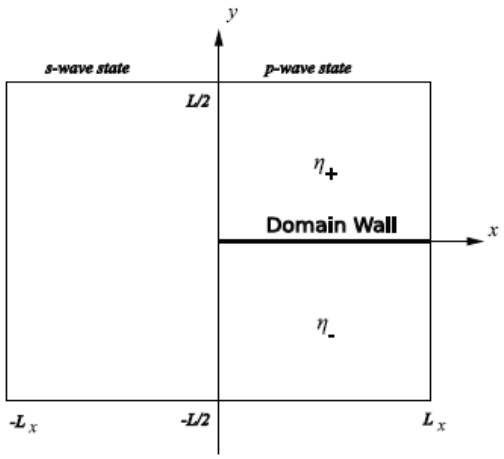


Figure 3.8: Domain wall schematic as described by Bouhon and Sigrist [35]. $\eta_+$ and $\eta_-$ are the two different chiral windings of the order parameter $\mathbf{d}(\mathbf{k}) = \hat{\mathbf{z}}(k_x \pm ik_y)$.

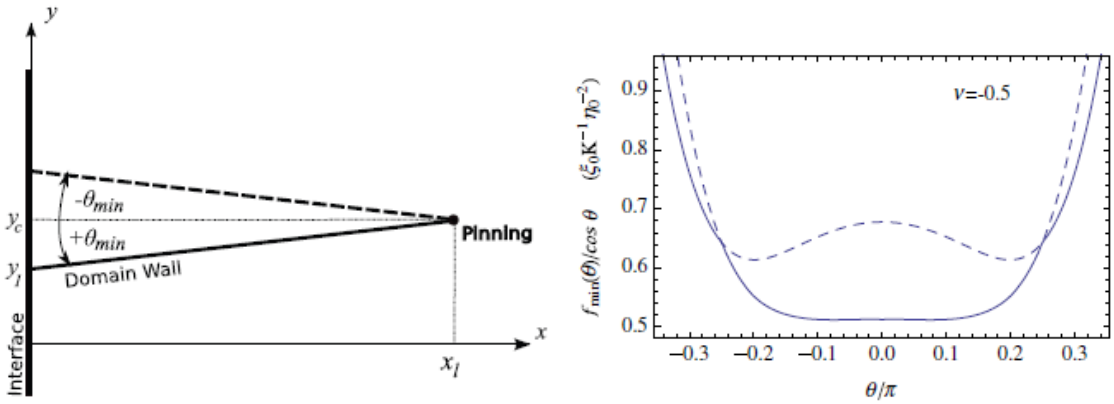


Figure 3.9: Schematic of Domain wall movement around a pinning point in the crystal. Graph is of both the stable (solid) and metastable (dashed) branches of the free energy. Metastable branch has 2 minima, corresponding to the angles in the schematic. From [35].

With a model of the domain wall in place, they go on to define $\phi(y)$ and then solve for the critical current in the junction. The critical current characteristic they develop from this model is Fraunhofer with very little variance in the pattern as shown in Figure 3.10.

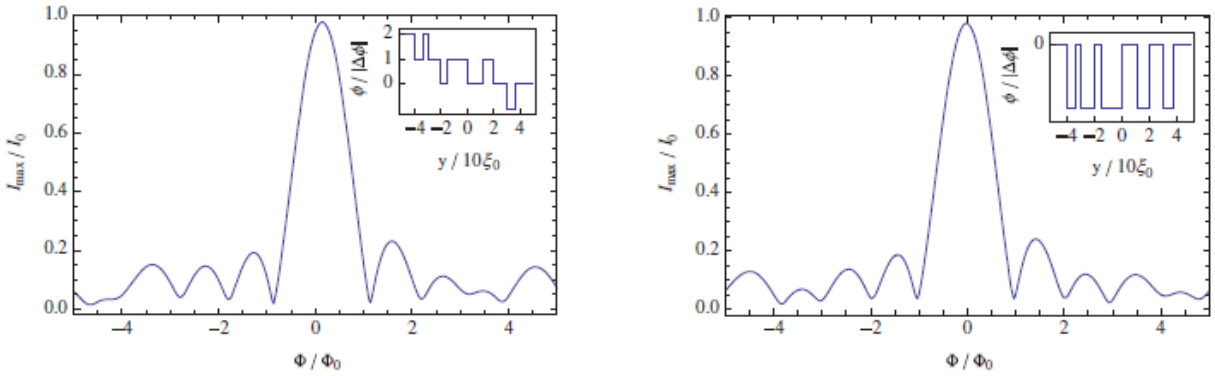


Figure 3.10: Two different Interference patterns as modeled by Bouhon and Sigrist [35]. The right pattern has 0 total phase shift across the junction, where as the left one has a phase difference of $2\Delta\phi$.

The more interesting information that came out of this work was the ability to model the hysteresis seen in Kidwingira's data [8]. The hysteresis was a very interesting effect that is normally associated with magnetic properties and Bouhon and Sigrist's ability to model it makes their theory intriguing. Essentially, they state that if all the domain walls in the junction are shifted to the maximum angle, it will shift the pattern slightly right(left) based on the maximum positive(negative) magnetic field. Figure 3.11 shows side by side the model and the data.

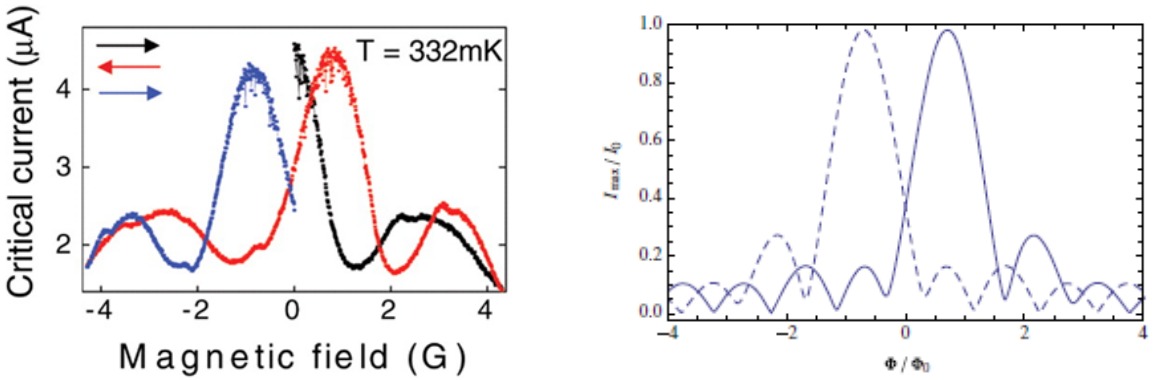


Figure 3.11: Comparison of hysteresis pattern to model by Bouhon and Sigrist [35]. The critical current characteristic on the left is from Kidwingira *et al.* [8] and is representative of the hysteresis they saw in their edge junctions on $Sr_2RuO_4$.

Bouhon and Sigrist also developed a way to identify the number of domains in the junction based on the hysteresis pattern. Essentially, they identify that the maximum shift

in the field will correspond to the number of domains in the following manner

$$\frac{2\pi\Phi_{mc}}{\Phi_0} \approx -\sum_{i=1}^{N} \Delta\phi_{i\mu} = -(\phi(L/2) - \phi(-L/2)) = -N\Delta\phi \tag{3.11}$$

$$N \approx -\frac{2\pi\Phi_{mc}}{\Delta\phi\Phi_0} \tag{3.12}$$

where $\Phi_{mc}$ is based on the maximum field that hysteresis pattern reaches. Bouhon and Sigrist find from this that the domain size ranges from 4-10 $\mu$m in Kidwingira's junctions.

### 3.3.2 Small Junctions with Domains

One of the assumptions that Bouhon and Sigrist made in their previous argument was that the junctions were large in comparison to the domains. However, the goal of this project is to shrink the size of the junctions to around the size of the domains. Therefore, some of this previous theory will not be applicable to these junctions. From a theoretical viewpoint, however, these junctions should be an easier system to model.

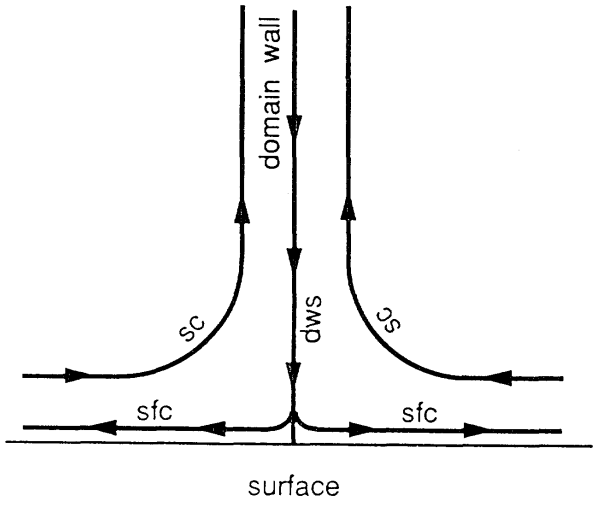


Figure 3.12: A possible current flow schematic for a domain wall intersecting the surface of $Sr_2RuO_4$. From [36].

One theory of the physics near a domain wall was developed by Sigrist *et al.* [36]. Figure

3.12 shows their model of counterflowing currents. This flow diagram could imply a node at the domain wall where no current could flow across the junction, and similarly, near the domain wall the current could be suppressed. Using this we can look at some examples of possible domain structure we may see in our measurements.

The simplest case is when the junction is smaller than the domain structure, where we should see a standard Fraunhofer pattern as there is no phase change along the junction face. Figures 3.13, 3.14, and 3.15 show several other common possible domain structures, for reference. We have specifically included the domain boundaries and the critical current density plots with each interference pattern plot. The last two pairs of plots depict $\pi/2$ phase differences across the domain boundary rather than $\pi$ as in the other plots. This is to allow the reader to see this possibility as it will present itself later in the data. For all of the simulations, we have used the most basic form of the critical current density as set out previously and integrated that across the junction width. We then simply evaluated the functions for the flux span as presented to obtain the interference patterns.

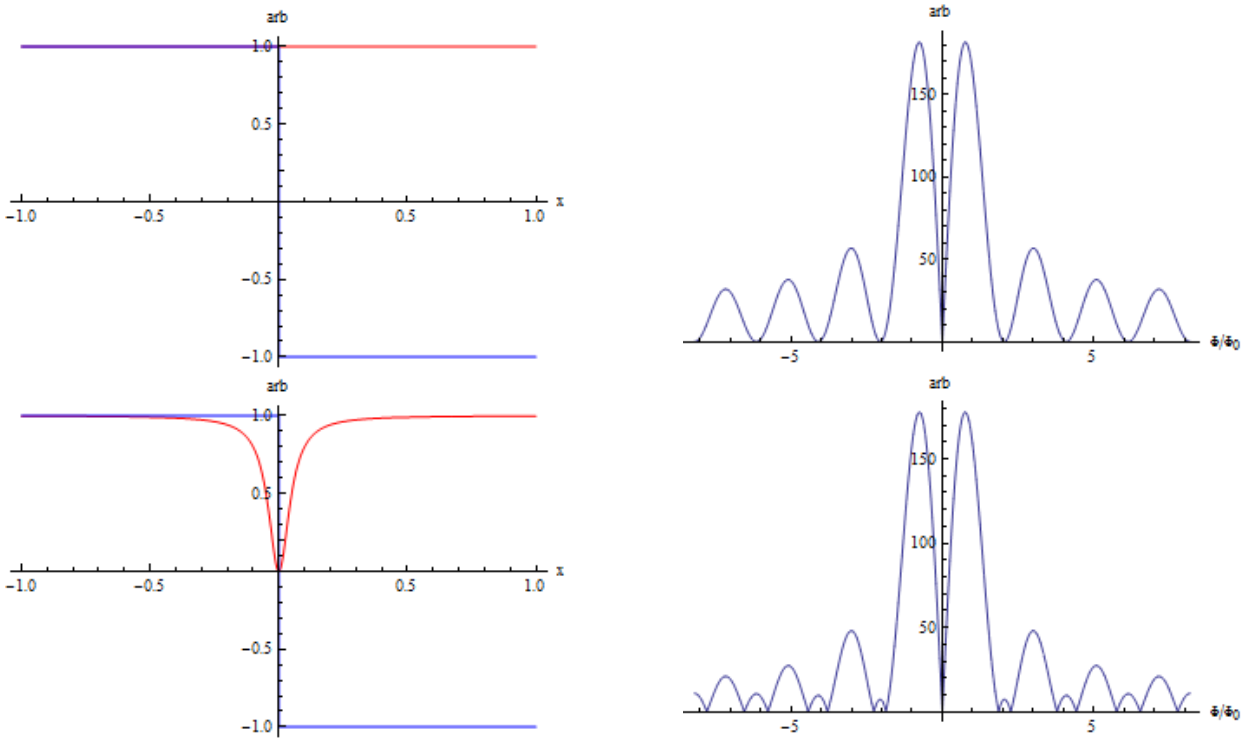


Figure 3.13: Simulations of domain structures with a 2 domains and a domain wall centered on the junction. The phase difference across the domain wall is $\pi$. The junctions are 2 $\mu$m in size. The second set contains a drop in the critical current density near the domain wall. The domain structure(blue) and critical current densities(red) are in the graphs on the left. The critical current characteristic is on the right.

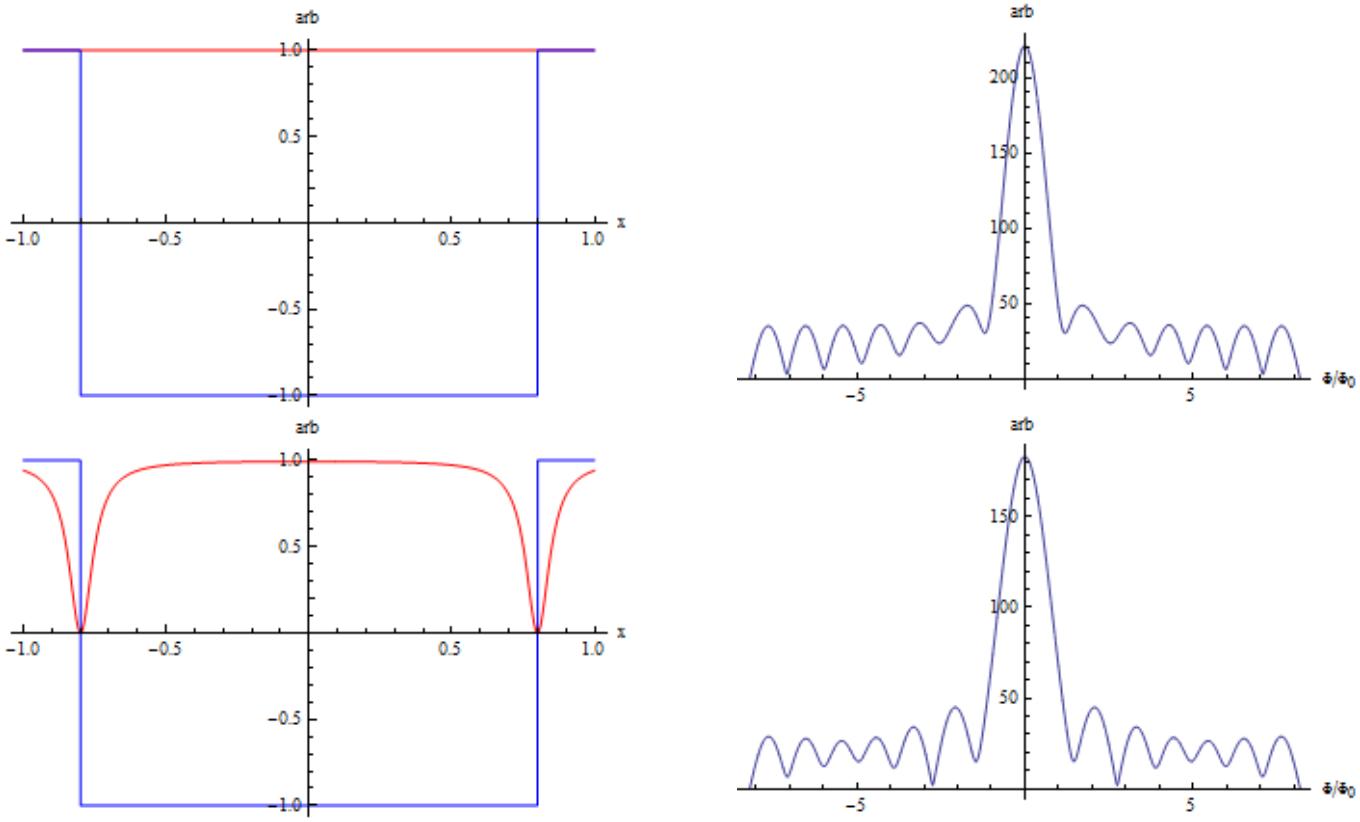


Figure 3.14: Simulations of domain structures with a 3 domains and domain walls near the edge of the junctions. The junctions are 2 $\mu$m in size. The second set contains a drop in the critical current density near the domain wall. The domain structure(blue) and critical current densities(red) are in the graphs on the left. The critical current characteristic is on the right.

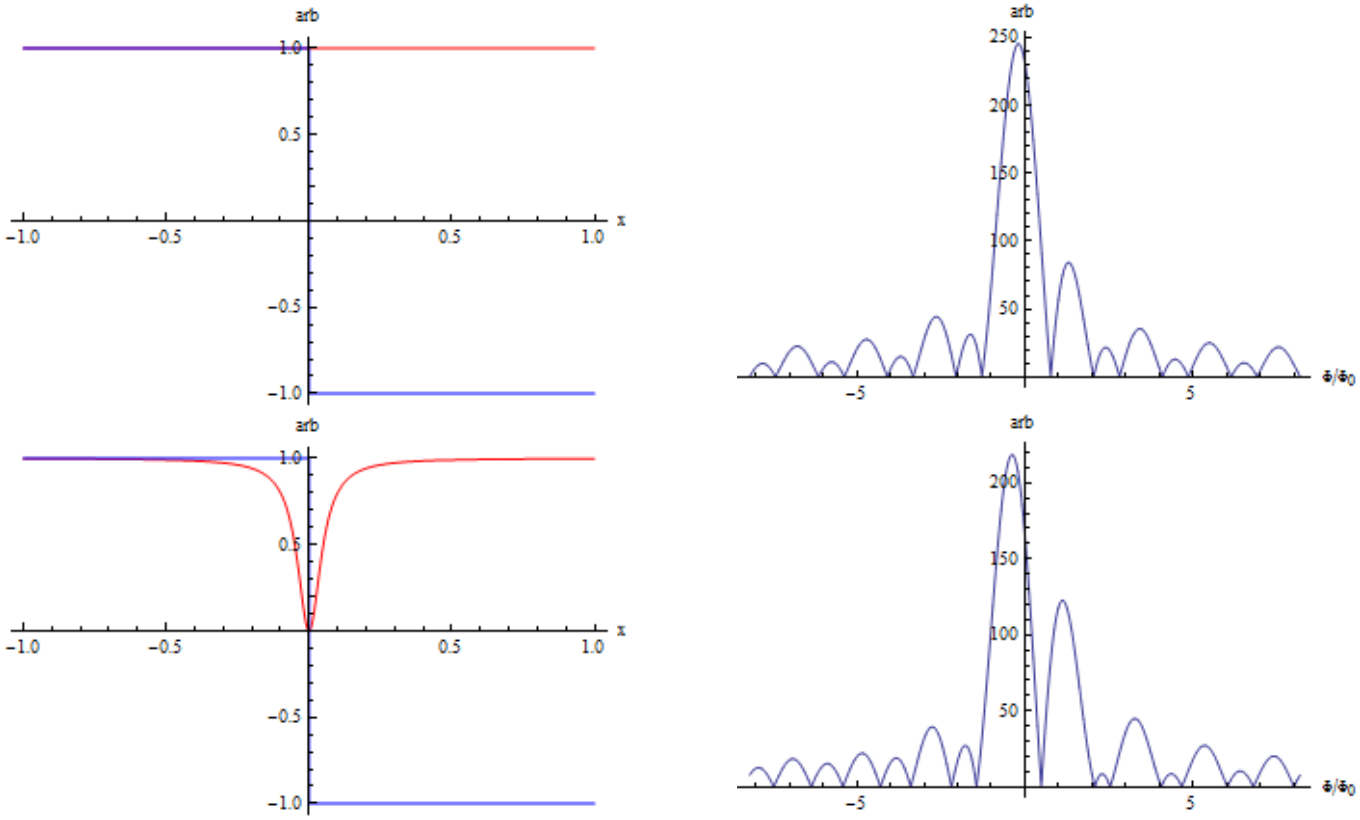


Figure 3.15: Simulations of domain structures with a 2 domains and a domain wall centered on the junction. In this case, the phase drop over the domain wall is considered to be $\pi/2$. The junctions are 2 $\mu$m in size. The second set contains a drop in the critical current density near the domain wall. The domain structure(blue) and critical current densities(red) are in the graphs on the left. The critical current characteristic is on the right.

# Chapter 4

# Fabrication of Samples

## 4.1 Crystal Growth

Due to the previously discussed necessity for very clean single crystals of $Sr_2RuO_4$, Yoshitero Maeno's research group at Kyoto University developed a method of growing very clean single crystals using a Floating Zone technique in a commercial image furnace [37]. A feed rod made from $SrCO_3$ and $RuO_2$ is brought close to a seed material, single crystal or sintered polycrystalline $Sr_2RuO_4$. A molten zone is formed at the bottom of the feed rod and the seed material is raised into this molten zone. The feed rod and the seed are kept counter-rotating at approximately 33 rpm and the entire structure is lowered such that the molten zone moves up the feed rod and grows the crystal out of the seed. The entire process is crucible free and the amounts of Ba and Na are kept to a minimum in the feed rod due to their negative effect on the $T_c$ of the resulting crystal [37, 10].

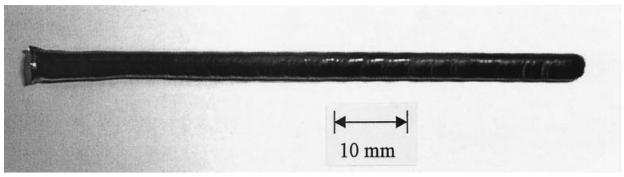


Figure 4.1: Single crystal rod of $Sr_2RuO_4$ grown at Kyoto University. From [37].

With crystals grown using this method, Maeno *et al.* found that the crystals were very high quality, characterized by $T_c$ close to $T_{c0} = 1.5$ K. They also characterized crystals in slightly less than ideal conditions. When the ratio $2N(\mathrm{Ru})/N(\mathrm{Sr})$ is $\geq$1.2 rather than the nominal value of 1.1, Ru metal would solidify into islands in the core of the crystal as shown

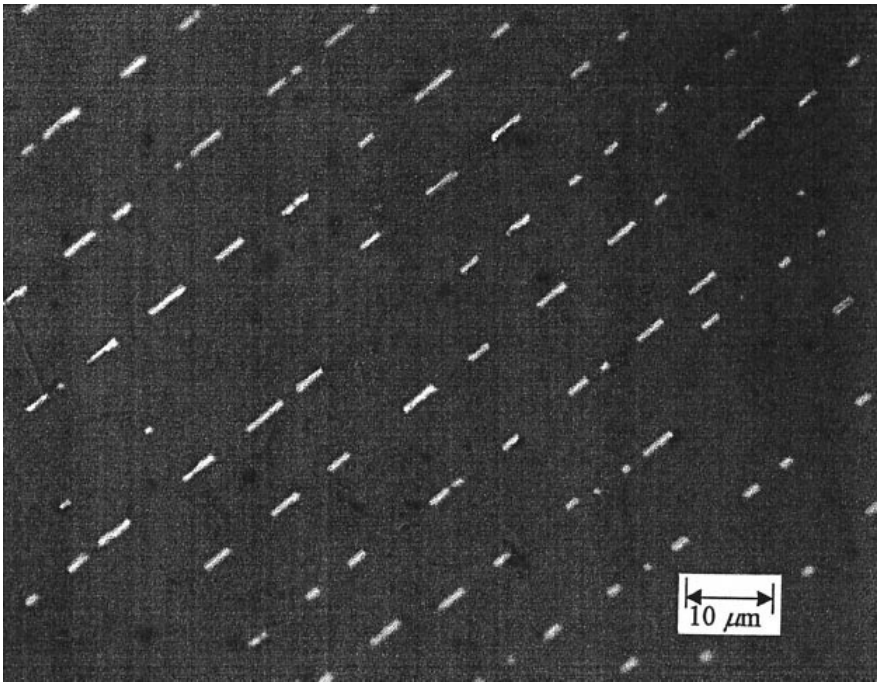


Figure 4.2: Optical Microscope image of *Ru* inclusions along the core of a cleaved $Sr_2RuO_4$ crystal. From [37].

below. This eutectic solidification was detrimental to the $T_c$ of the crystal.

For cases where the velocity between the feed rod and the growth rod was reduced and the partial pressure of Oxygen was increased slightly, a different impurity phase was produced. Large amounts of $Sr_2RuO_3$ formed around the cleavage planes of the crystal, which is easily seen under an optical microscope.

For large partial pressures of Oxygen and Ru-rich feed rods, the growth was especially poor. An insulating layer formed on the outside of the rod along with a second phase of Ru-rich islands forming inside the rod. This growth method was highly unsuitable to growing clean single crystals.

## 4.2 Sample Preparation

The crystals used in these experiments required a fair amount of preparation due to the fact that the Josephson Junctions needed to tunnel into the *ab-plane* of the crystal. In

our early attempts we cleaved the crystals along the $c$ axis, essentially breaking the crystal along a plane. It had been shown in previous work [9] that cleaving could lead to higher tunneling supercurrents and thus an easier measurement environment. However, due to the large amount of turnover inherent in this process, we decided to use polishing instead.

We selected $Sr_2RuO_4$ crystals that already had fairly straight, cleaved faces and polished them to remove any blemishes or defects in the surface. The polishing consisted of first using a 1 $\mu$m alumina grit polishing sheet to get a "rough" polish on the surface. We then used a 0.03 $\mu$m alumina grit polishing sheet to give the surface a mirror-like finish. It had been previously observed [9] that the polishing procedure can disorder the surface of the crystal and form a dead layer due to the disorder and oxygen depletion. We annealed the crystals in air at 900 °C for 24 hours to remove any defects caused by the polishing.

Using a procedure developed in our group by David Wollman [7], the crystals were then glued down to a glass substrate, specifically frosted glass to better promote adhesion. We used polyimide, a photoresist, because it easily wets to the surface of the crystal and the glass substrate, forming a smooth meniscus at the glue-crystal interface. Polyimide also has a smooth surface after baking, survives cryogenic temperatures, and is easy to remove in the case of gluing errors. For these reasons we find it to be a superior adhesion agent for the crystals.

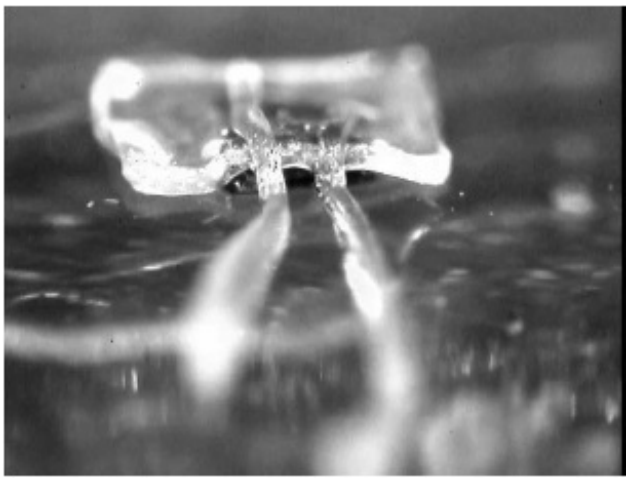

Figure 4.3: Riston masking on a $Sr_2RuO_4$ crystal. From [9].

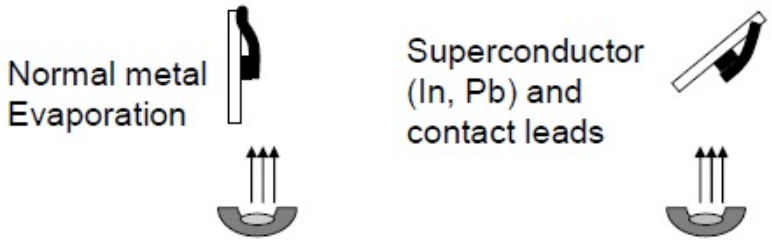


Figure 4.4: Schematic of Josephson Junction evaporation process. From [9]

After the glue has set, we use a material called Riston to mask the sample for evaporation. For these crystals, we masked two large leads that contacted the outer most edges and sides of the crystal to act as leads with low resistance. Then a large junction is masked in the center with a few leads that break out into pairs of leads for each individual junction that will be cut later using a Focused Ion Beam. The masked leads come close to the crystal without actually touching the vertical crystal face. In this manner, we minimized the distance we needed to pattern the junctions using the Focused Ion Beam without compromising the face of the crystal.

We then mounted our samples in a Commonwealth Thermal Evaporation system that is outfitted with both thermal evaporation sources and a 8 cm Ion Mill. Both *Cu*, to be used as the junction barrier, and *PbIn* were loaded into Tungsten boats for the thermal evaporation. The system was evacuated to a pressure of $3 \times 10^{-7}$ and the crystal face was cleaned using low power ion milling. We then oriented the crystal face towards the evaporation sources and deposited $25nm$ of *Cu* on the face of the $Sr_2RuO_4$ crystal. Then *PbIn* was deposited on the face and the sample stage was slowly rotated to make a continuous film of *PbIn* to form the lead pattern that was masked on the glass as indicated in Figure 4.4. A finished evaporation is shown in Figure 4.5(a) with an SEM image of an uncut large junction in Figure 4.5(b).

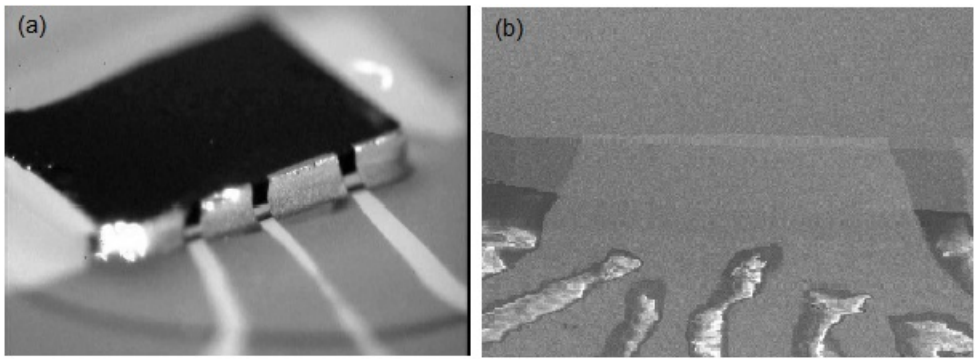


Figure 4.5: (a) Image of a crystal after evaporation and removal of Riston masking. From [9]. (b) SEM image a junction before FIB fabrication of junctions.

## 4.3 Focused Ion Beam Etching of Junction

We previously developed a method of selectively etching Josephson Tunnel Junctions from a larger patterned junction using a Focused Ion Beam (FIB) for studying angular changes in the order parameter in $UPt_3$ [38, 39]. The FIB that was used in this project was developed by FEI Company and uses dual Ion and Electron beams for etching and imaging samples. The Ion bean is a focused beam of Gallium ions that are accelerated at 30 kV towards the sample. Incidental damage due to the beam is small, on the order of 15 nm along the beam direction and 5 nm lateral, which is 1% of the smallest junctions we attempted to cut. Also, condsidering the presence of 1 $\mu$m of *Pb* covering the junction, any *Ga* implantation should not be in the $Sr_2RuO_4$ crystal and should not effect the superconductivity of the crystal.

As was stated previously, the goal of this technique was to fabricate Jospehson Junctions on the order of the predicted domain size in $Sr_2RuO_4$. With the ability to cut lines as small as 20 nm, the FIB is uniquely suited to this task. In our first attempt to cut junctions, we used a fabrication scheme where we halved the size of the junction for each successive one that was cut along the length of the face as seen in Figure 4.6. The smallest junction in this series is 500 nm, doubling as you move to the right.

The goal for each junction cut was to attempt to keep both the width of the junction and the height, as measured from the glue line up the crystal face, approximately the same. This

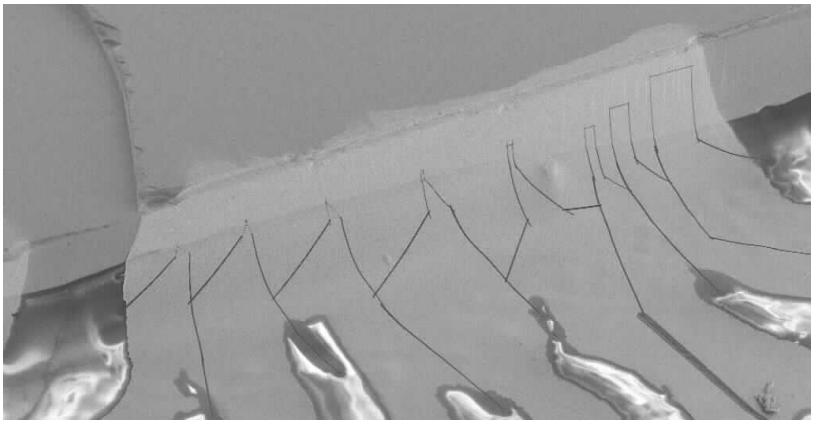

Figure 4.6: Initial attempt at fabricating Josephson Junctions using Focused Ion Beam Technology. Smallest junction on left is 500 x 500 $nm^2$ and each successive junction is doubled in size.

becomes much more difficult to achieve at smaller junction sizes, simply because you want to make sure to have enough contact with the crystal and not risk there being an undetectable layer of glue under the junction. We will discuss the results of this prototype later, however some of the junctions turned out to be too large to easily measure without using a SQUID potentiometer, due to their very small normal state resistance.

We restricted ourselves to the 4 smallest junctions sizes, as they pertained more closely to our search for both single and multiple domain junctions. Therefore, we mainly fabricated junctions which we label as 500 nm ($500 \times 500$ $nm^2$), 1 $\mu$m ($1 \times 1$ $\mu m^2$), 2 $\mu$m ($2 \times 2$ $\mu m^2$), and 4 $\mu$m ($4 \times 4$ $\mu m^2$) as our nominal junction sizes. We expect that this should easily span the crossover point between single and multiple domain junctions. In Figure 4.7 you can see a typical large junction that has been cut with one of each of these junctions, including closeups of the junctions in the figures that follow. Much care was taken in the location of the junctions to keep them in areas that were free of defects.

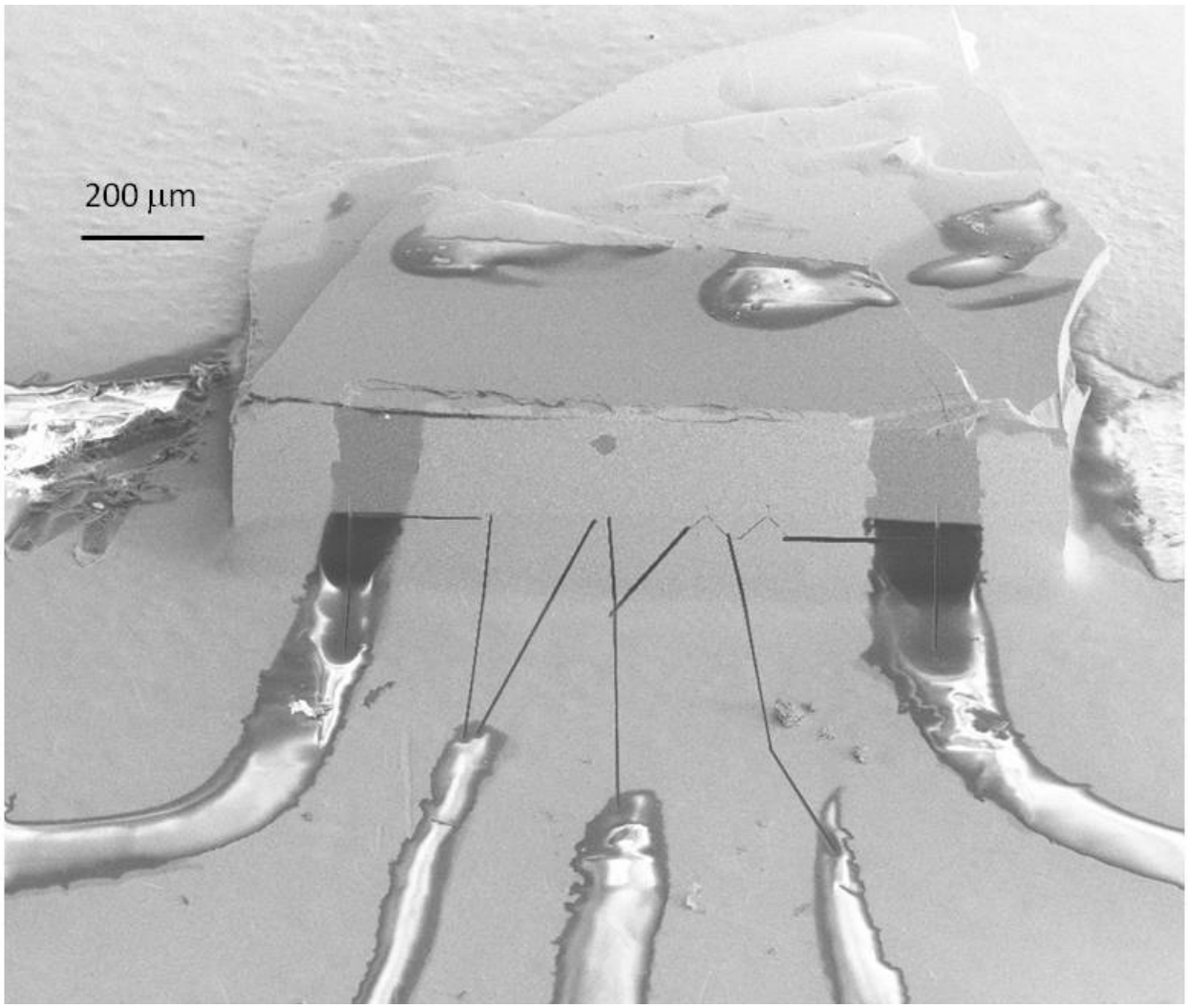


Figure 4.7: Full View of a junction that has been patterned using the FIB. Image is zoomed out to show side leads and entirety of the crystal.

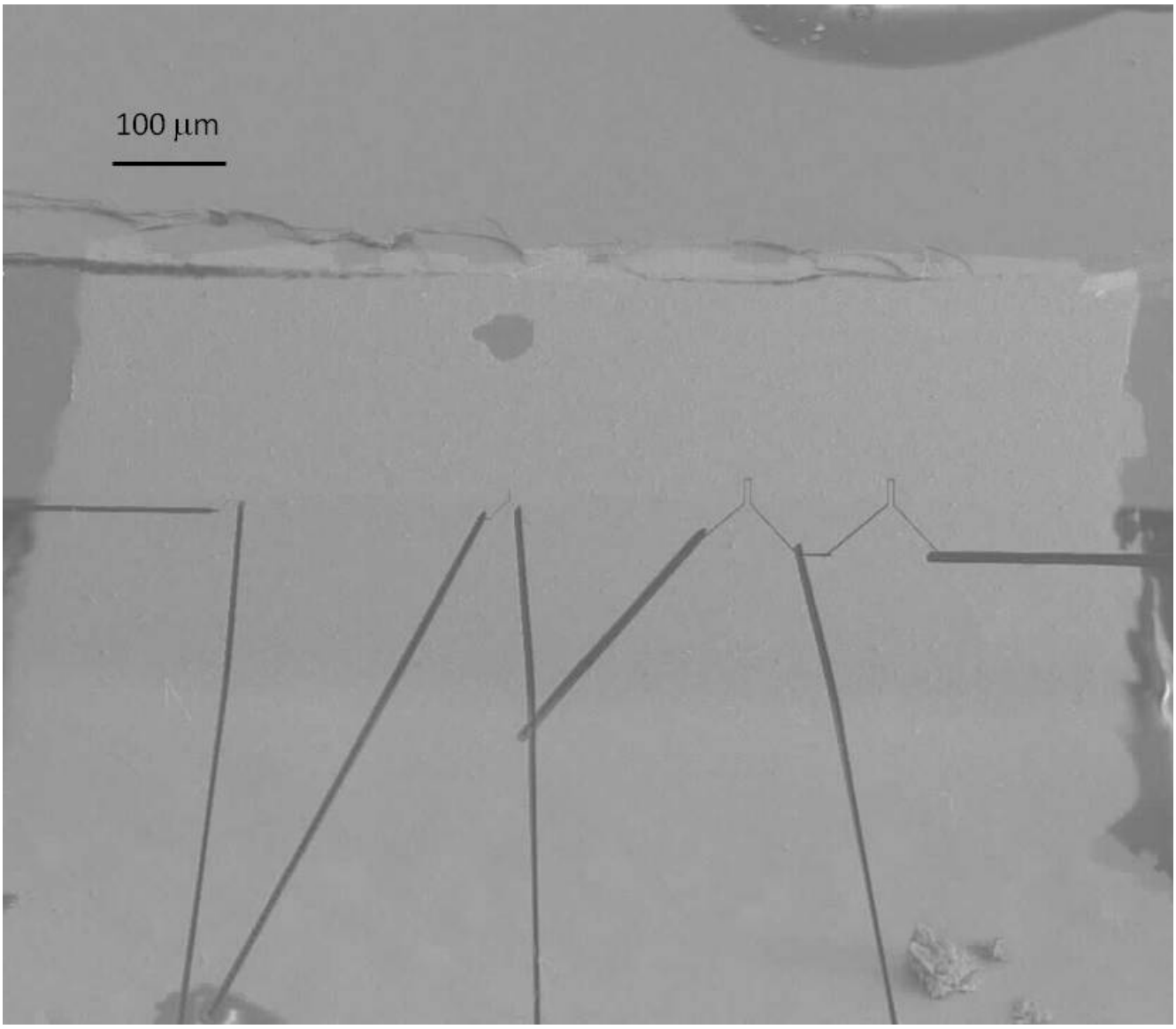


Figure 4.8: Closer view of all junctions on same crystal as previous figure. Spacing of junctions is kept fairly even across face, to help reduce the likelyhood of any anomalies due to local irregularities

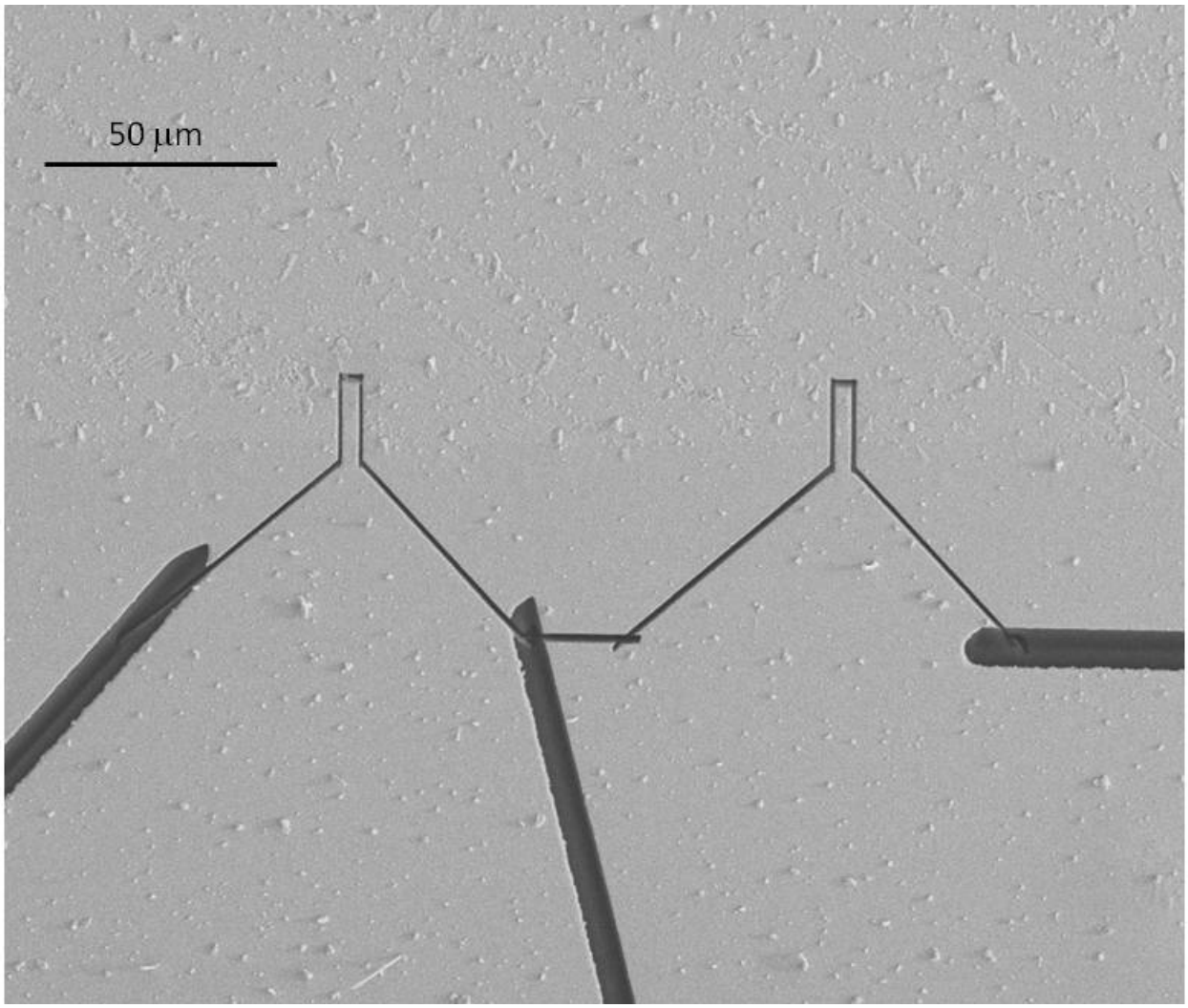


Figure 4.9: Zoomed in view of two 4$\mu$m junctions from previous crystal. Both junctions were written with the same image file on the FIB.

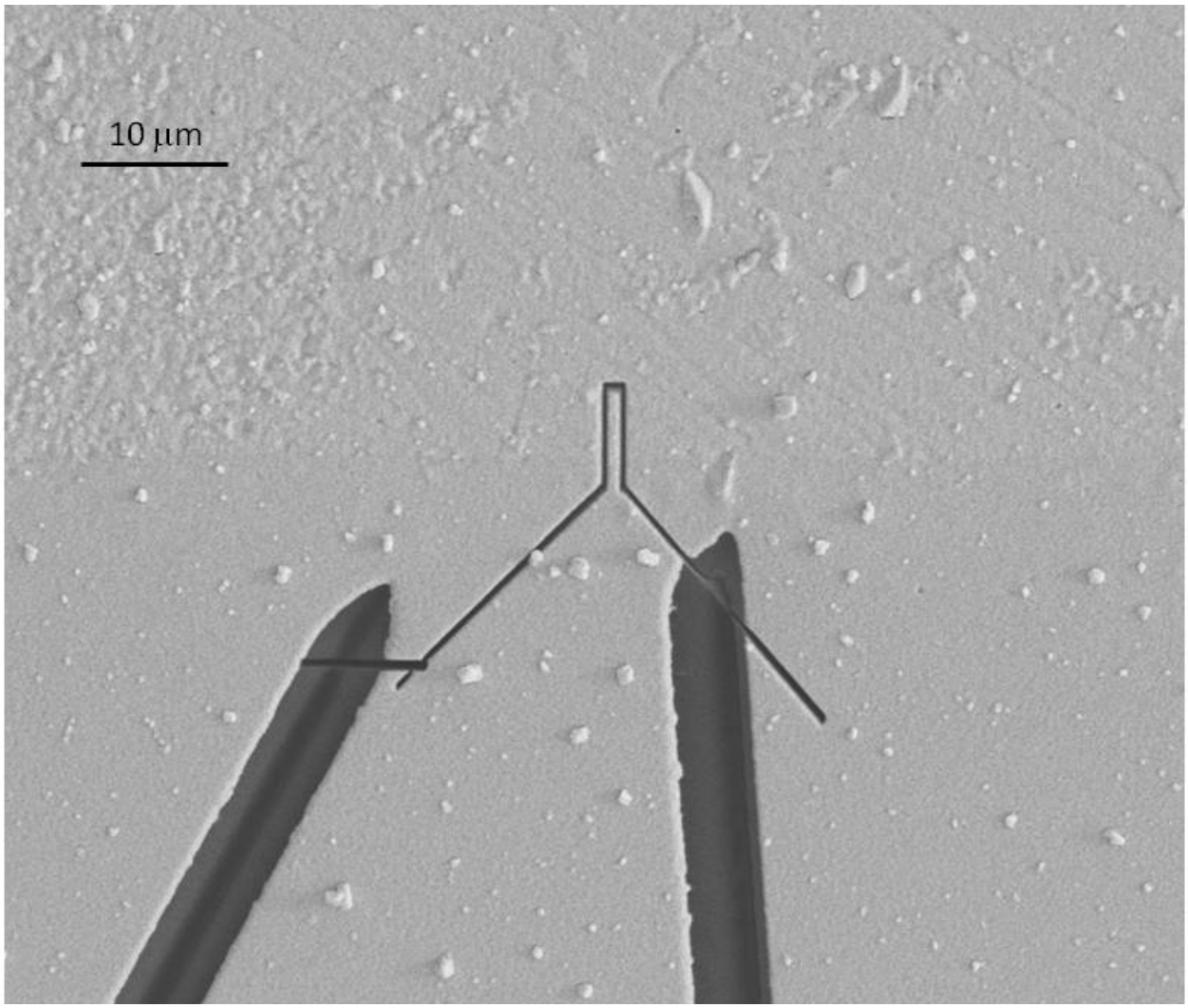


Figure 4.10: Close in view of a 1 $\mu$m junction. Of note is the extremely clean junction area. Great care was taken to avoid any film or crystal defects in the placement of junctions.

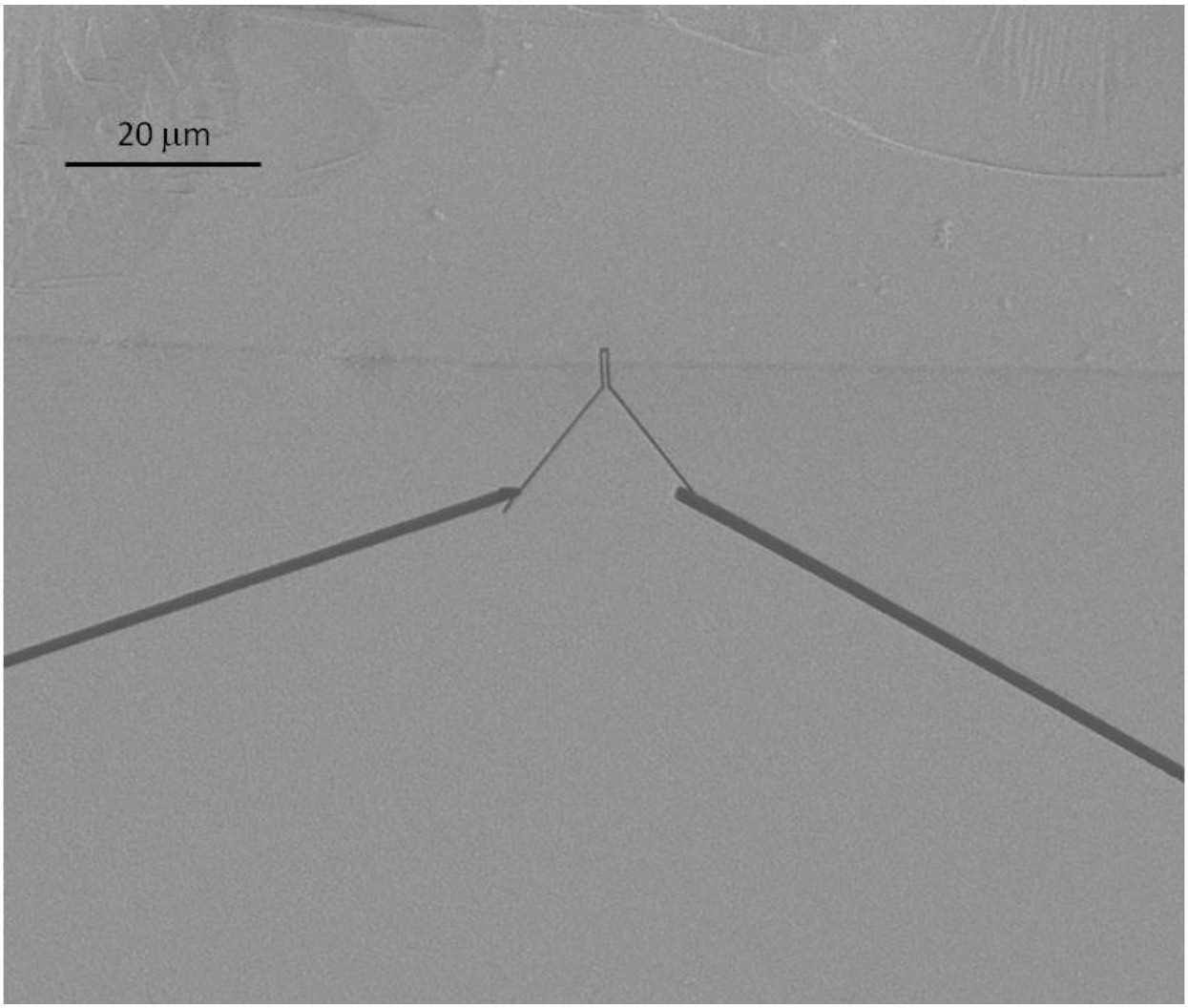


Figure 4.11: Close in view of a 500 nm junction from a different crystal. View is slightly zoomed out to give an impression for the magnitude of these junctions.

# Chapter 5

# Measurements of Domains in Nano-Junctions on $Sr_2RuO_4$

## 5.1 $^3$He Measurement System

To reach well below the $T_c$ of our $Sr_2RuO_4$ crystals at 1.4 K, we used a $^3$He single-shot refrigerator. The refrigerator sits in a $^4$He bath with a vacuum space around the sample. $^4$He can be drawn into a chamber inside the vacuum can and pumped on to bring the temperature down the 1.5 K through evaporative cooling. This "1K pot" is then used to cool $^3$He that is in a closed system, with a collection space at the top of the insert for the gas phase, and a chamber at the bottom, "$^3$He pot", for the liquid phase when it is condensed through the 1K pot. There is also a sorbtion pump, essentially activated charcoal, in the closed system for pumping on the liquid $^3$He, allowing the system to cool to approximately 300 mK. The system can stay at base temperature for 5 hours with low amounts of applied power.

The stage used in these measurements is Oxygen-Free High Conductivity (OFHC) Copper that is bolted to the $^3$He Pot. A Helmhotz coil is attached to the stage to supply magnetic field in the axial direction. In this case, the Helmoltz coil is only loosely coupled to the $^3$He Pot, but more tightly coupled to the 1K Pot due to heating concerns and better base temperature on the $^3$He pot and stage.

## 5.2 Setup of Electrical Measurements

The wiring for each junction is split on chip to allow for the application of current and measurement of voltage on each seperate junction with minimal contact resistance. Copper wires are attached to the sample using Indium dots pressed onto the *PbIn* leads. The copper wires are heat sunk to the OFHC Copper stage at pins. The wire from this point up through the refrigerator is constantan and is heat sunk to both the 1K pot and to the 4 K bath. The wiring terminates in a shorting box at the top of the refrigerator. The box is connected to a secondary breakout box that allows for addressing individual wires. We were careful to make measurements on twisted pairs of wires to reduce noise and stray magnetic fields in the refrigerator whenever possible. The Helmholtz coil is seperately wired on all copper leads to help increase current, and thus the magnetic field, that can be applied to the coil. Its wiring is heavily sunk to the 1K pot to reduce the load on the $He^3$ pot.

Our main measurement procedure was to first measure the critical current, $I_c$, of each junction on the chip to determine which junctions were working and which did not survive processing or cooldown. Due to the interesting geometry of these junctions, there was significant turnover of the samples. Also, there is a limited number of cooldowns a sample can withstand before failures in the glue or interlayer stresses in the crystal tend to destroy the junctions. Later procedures using annealing seem to alleviate much of the crystal stress failure mode.

To measure the critical current, we used a current supply designed and built in our laboratory. It uses a feedback amplifier to monitor the current across a fixed resistance with a push-pull transistor network in series with the output to help drive large currents when necessary. The current supply has a range of 100 nA to 500 mA, with decade settings for different ranges (10 $\mu$A, 100$\mu$A, 1 mA, 10 mA, 100 mA) and a 1, 2, and 5 multiplier to give us the most flexibility possible in our applications. The current is also actively monitored *in situ* by a buffered amplifier that can be directly fed to the computer.

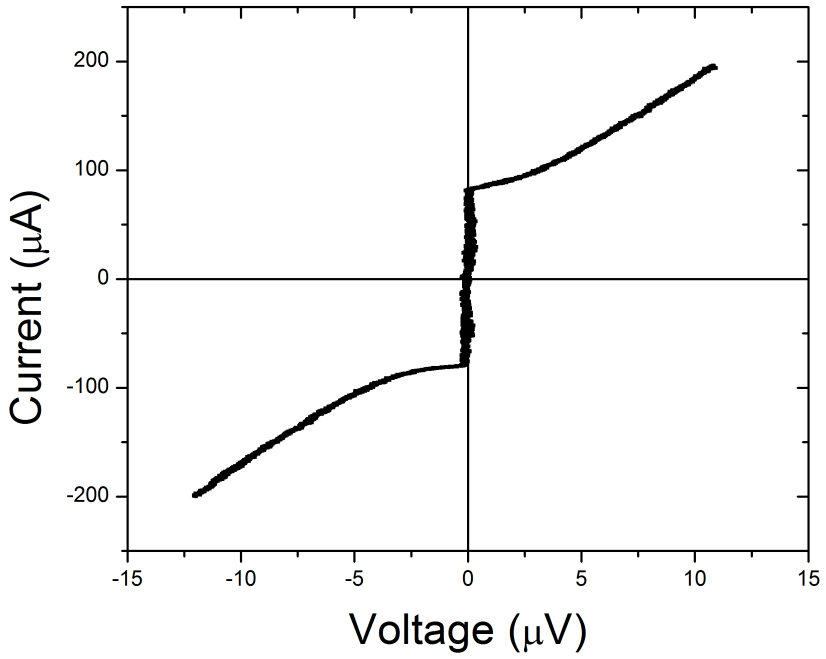


Figure 5.1: A typical IV curve for our Jospehson Junctions. The current is swept and the voltage is measured using a preamplifier.

The voltage portion of the readout is across a seperate set of leads, as indicated previously. An Ithaco preamplifier is used to monitor the voltage signal and buffer it from the computer inputs, to reduce noise. Also, the preamplifier has built-in bandpass filtering which is helpful for reducing noise. The preamplifier has gain settings ranging from 1 to 5000 and we typically used a setting of 100 to 500 for our measurements.

Figure 5.1 is a typical IV characteristic taken from one of our junctions. The critical currents ranged from a few $\mu$A to at most 1 mA in size. Critical currents above that range usually indicate a superconducting short somewhere in the circuit, usually through the junction barrier.

As discussed previously, another feature of Jospehson Junctions that is central to our measurements is the modulation of the critical current with a magnetic field. Using the Helmholtz coil, we can apply a magnetic field to the sample while actively monitoring the

critical current in a couple ways. Whether the critical current modulates or not can also be a good indication of whether we are dealing with a good junction or a superconducting short.

Our first technique for measuring critical current as a function of applied magnetic field is to apply a fixed current to the junction that places the junction in the voltage state. Then we measure the voltage across the junction as the magnetic field is swept through a bipolar function, starting from zero and going to the same value of both positive then negative magnetic field. As long as the applied static current is large enough to keep the junction in the voltage state, the voltage will be proportional to the critical current. The benefit of using this method is that very fast changes in the critical current are easily measured due to the low amount of averaging required. Also, there is no need to lock to any current or voltage value which can give feedback problems with large switching. However, this technique suffers from the issue that it is not easy to correlate the voltage to the critical current. The sensitivity of the measurement is also dependent on the applied current. If the current is setup for reading the maximum critical current over the range, the smaller critical current values tend to wash out as the voltage signal is fairly constant for these values of critical current. The opposite is also true, if the current is set too low, the features at low critical current will become apparent, however details around the critical current peak will be washed out as the junction will enter the superconducting state. Essentially, there is a trade-off between sensitivity around the peak, or sensitivity in the arms of the pattern.

For most of our measurements we were more interested in actually measuring the critical current as a function of field. We use a PID (Proportional-Integral-Derivative) program written in Labview to assist our measurements of the critical current. We set the PID program to lock on to a set voltage from the preamplifier, usually around 0.02 mV with a gain of 200, such that the junction is barely in the voltage state. The PID controls the output of the current supply that is feeding current into the junction to hold the voltage setpoint. We then can measure the current from this current supply as the critical current of

the junction, since as we stated before, we are barely in the voltage state. The PID actively monitors this voltage as the Helmholtz magnetic field is swept and we can actively measure the critical current as a function of the magnetic field, using the same bipolar field sweep pattern as described above. This monitoring allows us to meaure details at both the peak and in the arms of the interference pattern, a distinct advantage over the voltage technique. However, due to the number of iterations required for the PID to stay locked to the voltage, this technique can wash out some fast switching effects. With tuning of the PID coefficients, much of this can be alleviated, so this technique tends to be the better measurement setup for these junctions.

## 5.3 Comparison of Junctions around Domain Size

From previous work [9] as shown in Figure 5.2, we have seen various interference patterns for junctions >50 $\mu$m. Given a domain size estimate of 1 $\mu$m, we would expect junctions that contain 1 domain or a partial domain to exhibit Fraunhofer characteristics in a critical current versus magnetic field measurement with much greater detail than in previous measurements. For junctions larger than the domain size, the interference pattern is dependent on the phase change across the domain wall or walls. Let us first inspect the results from the prototype sample. This crystal was cleaved and the critical currents were much higher than subsequent junctions.

The voltage function depicted in Figure 5.3 is generally of the Fraunhofer type discussed previously. It was taken using the constant current technique described above, so resolution in the arms is low. In comparison with the patterns taken at much larger junction sizes depicted in Figure 5.2, this pattern shows a pronounced peak with better definition than previously obtained. The data was profound enough for us to push to make more junctions of higher quality.

Figure 5.4 shows critical current characteristics of junctions of varying sizes and varying

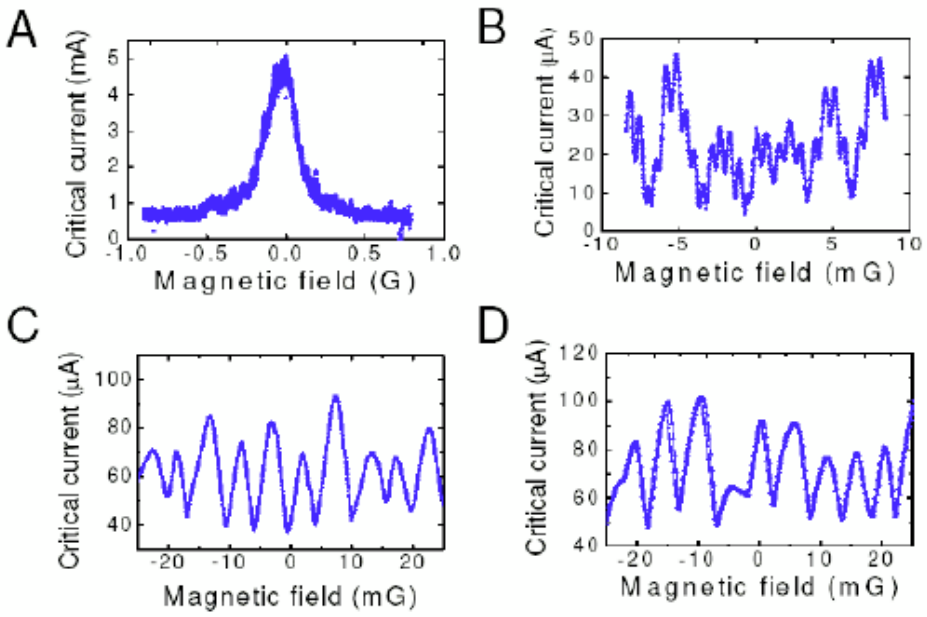


Figure 5.2: These are 3 different interference patterns taken from [9]. (A) Fraunhofer-like with no side lobes. (B) and (C) display patterns similar to a grain boundary junction, which implies many domains interfering with each other. (D) shows the same junction as (C) after a thermal cycle.

samples. Most notably, the 4 $\mu$m junctions show non-Fraunhofer characteristics, indicating a phase change across the junction. This phase change appears in 2 cases to be of order $\pi$, similar to Figure 3.13. In the third case, the raised side lobes of the pattern indicate some form of phase nonuniformity. This nonuniformity is most likely similar to a SQUID phase profile, where the bulk of the junction is of one domain with small portions near the edge consisting of domains with opposite chirality as shown in Figure 3.14.

The sub-2 $\mu$m junctions all show Fraunhofer-like patterns, the 500 nm junction being the most uniquely Fraunhofer shaped. There is also an interesting feature in that the switching on the top of the peak seems to decrease with decreasing junction size, and while some of this switching decrease may be due to increased quality in the fabrication process, there is definitely a component that is intrinsic to the junction. Whether this is due to crystalline interlayer domain switching or some other process will be explored in later discussion.

Overall, what we observe from these junctions is that there is some phase changes across

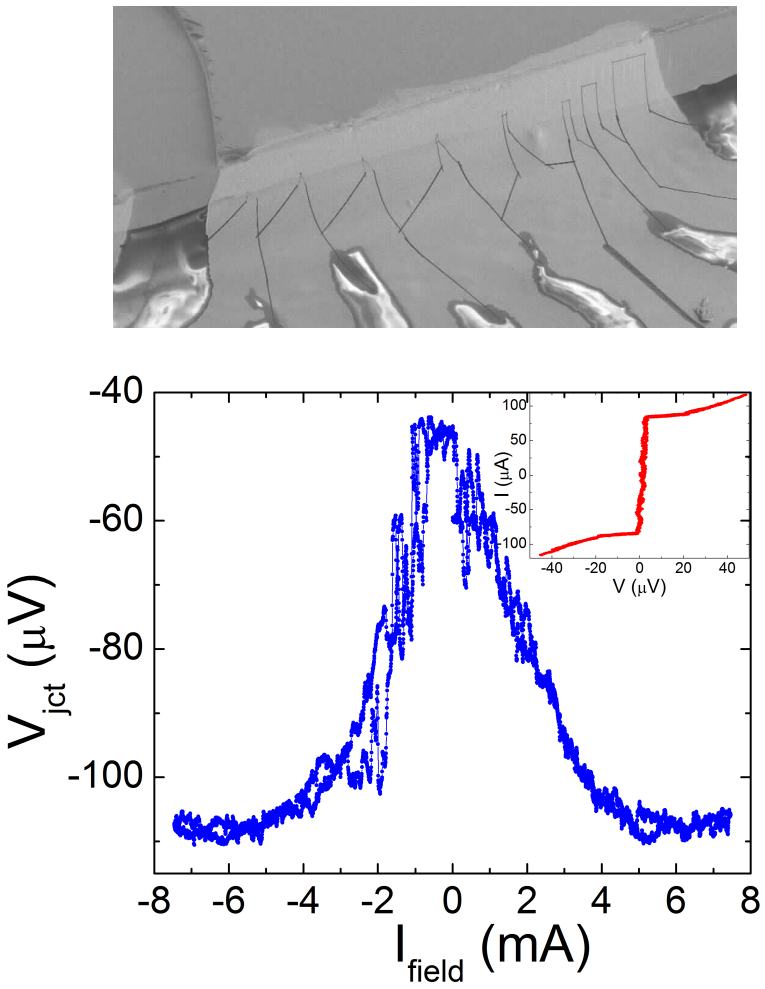


Figure 5.3: Prototype Junction with the voltage versus magnetic field measurement of the 500 nm junction. This measurement indicates that the junction is single domain.

the face of the junction that are not seen at and below 2 $\mu$m. We will explore some possibilities for these data in the coming sections, however some of these data deviate from current theory as set out by Sigrist [35, 36, 18, 30] and others.

To demonstrate the robustness of this measurement, we also compared critical current characteristics over multiple days of measuring this junctions. Over multiple cooling cycles the measurement gave similar results, as seen in Figure 5.5. There is a slight phase variation from different cooldowns, however the small amount of difference, and the junction being cooled in zero field, indicates that the junctions are not being effected by vortices during our measurements.

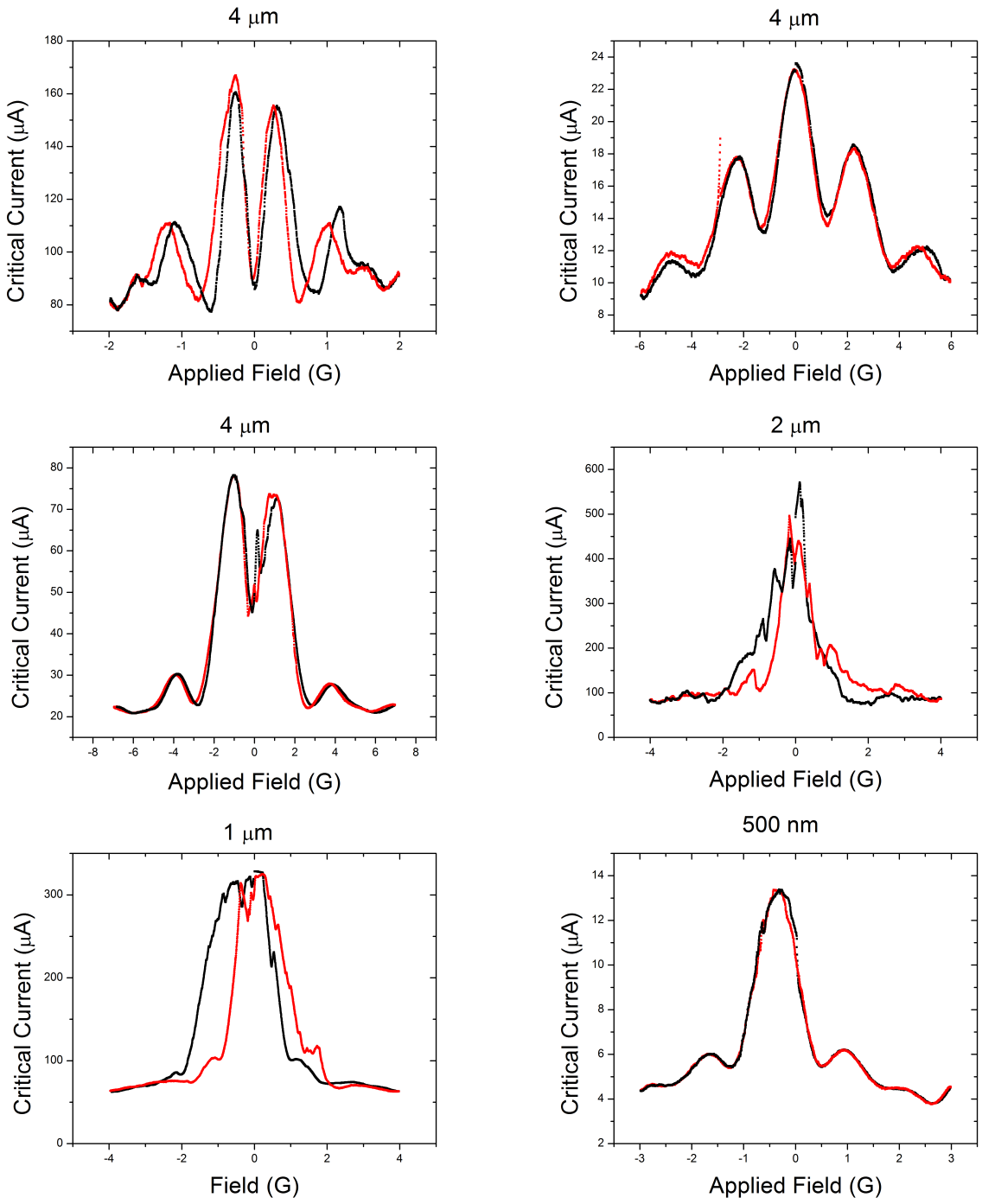


Figure 5.4: Critical current characteristics for a number of different sized junctions cooled without a magnetic field applied. Actual critical current values vary based on the method each junction was prepared. Above 2 $\mu$m the junctions no longer appear Fraunhofer-like in their critical current characteristics.

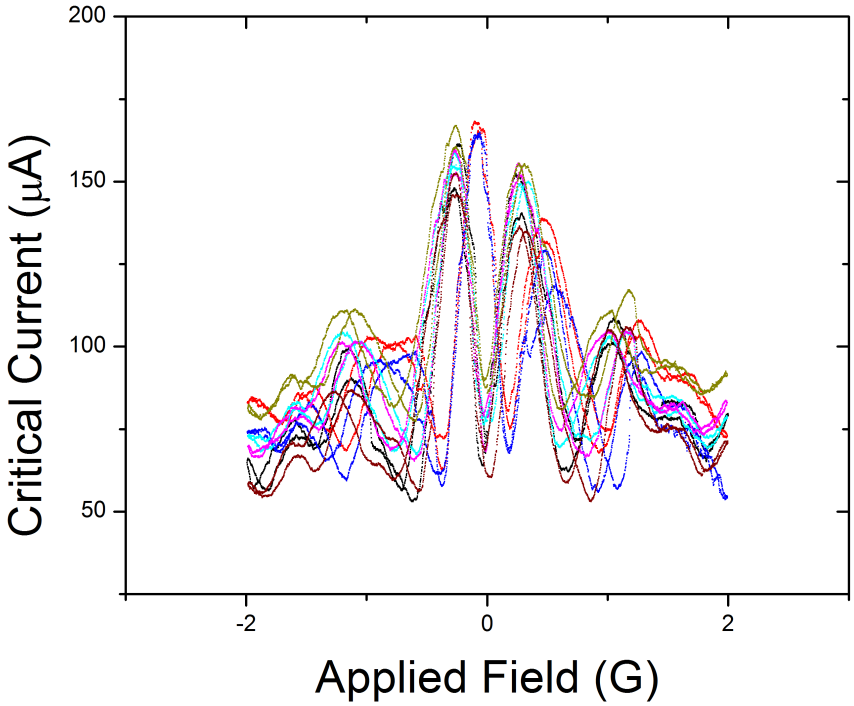


Figure 5.5: Multiple critical current characteristics taken over a four day period on the upper-left 4 $\mu$m junction in Figure 5.4. Each measurement was cooled in zero magnetic field.

### 5.3.1 Hysteresis in Critical Current Peak

One of the first interesting aspects of these junctions we noticed was similar to previous data taken on larger junctions [9, 8] as shown in Figure 5.6. The junctions showed a significant hysteresis in the placement of the critical current peak around zero field. This hysteresis seemed to be based on the span of the magnetic field scan. Our prototype junction showed a strange hysteresis signature in the 500 nm junction such that it seemed that the critical current peak was hysteretic at low fields and then switched sides as the field span was increased, as shown in Figure 5.7. The author cautions the reader that this data was specific to this junction and was never verified in other samples. We are simply showing it here to show our motivation for looking for hysteresis in these junctions. More typical hysteresis signatures will be discussed in the following pages.

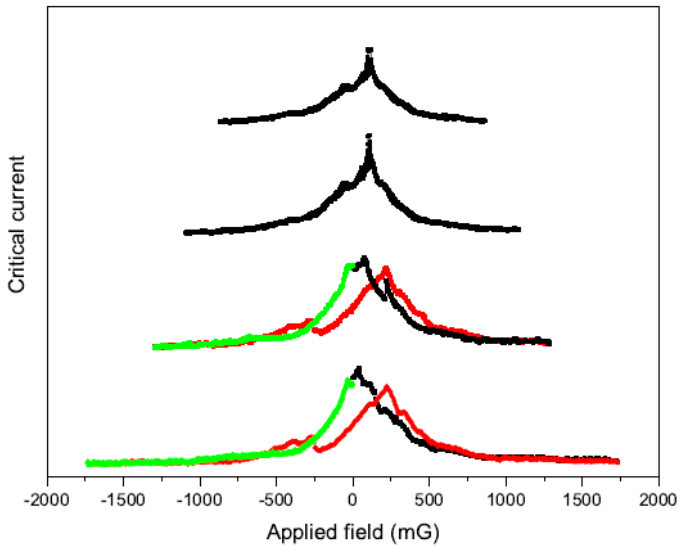


Figure 5.6: Hysteresis pattern from Kidwingira's dissertation [9]. The colored (red) curves all indicate scanning of the field in the positive (negative) field direction, or to the right (to the left). All scans begin at zero field.

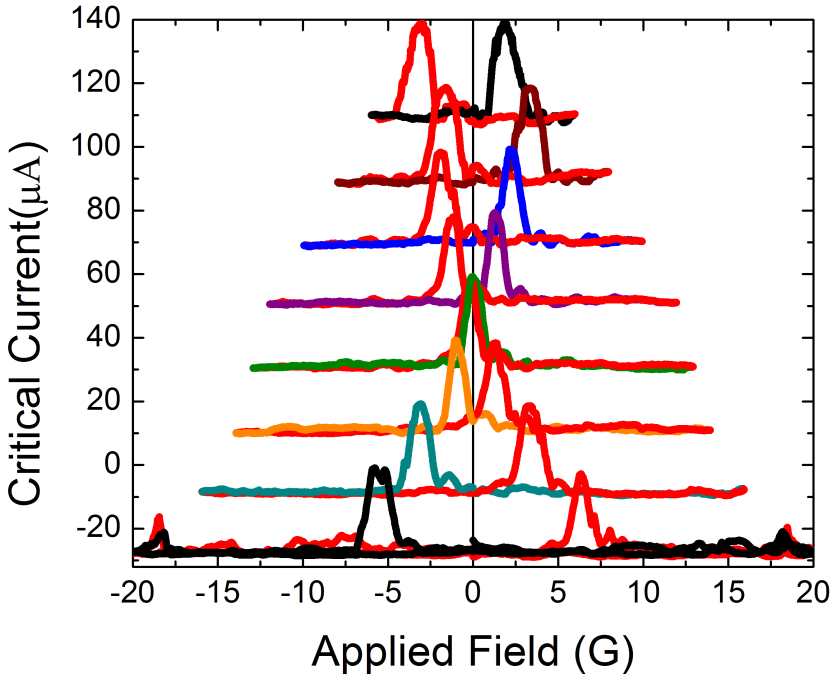


Figure 5.7: Hysteresis in the critical current of the 500 nm Prototype junction. This hysteresis signature was unique to this junction and provided motivation for further study of the hysteresis in different sized junctions. The colored (red) curves all indicate scanning of the field in the positive (negative) field direction, or to the right (to the left). All scans begin at zero field.

The hysteresis in Figure 5.7 is unique in a number of ways. First, it is the only hysteretic pattern we observed where there was hysteresis at low field spans. Typically in later samples, the patterns would retrace at low field spans and then the hysteresis grew as the span was increased. In the case of this junction at low field span, the critical current peak appeared as the magnetic field was swept up, *before* the field reached its peak, then reappeared after the field had swept down and past zero field. The behavior for field spans at and above 13 G is much more typical of the hysteretic behavior found in future samples. The critical current peak appears *after* the magnetic field has been swept to its maximum value and then appears again *after* being swept to its negative maximum.

The other feature that is anomalous in this hysteresis effect is the behavior at 20 G field span. The peak would only appear on one side for each field scan, and would alternate between which side it would appear on. Two sucessive plots were shown in Figure 5.7 to show the peak position relative to the other field spans.

Figure 5.8 shows two different sized junctions both from cleaved crystals, similar to the prototype junction. The patterns both show some interesting and similar features. The peak in the critical current in both cases seems to decrease with increasing magnetic field scans, but in the case of the 2 $\mu$m junction, it then increases again at large field values. It is also interesting to note that in both cases, there is a maximum field that is reached where the peak seems to stop moving, and then decreases in height. Bouhon and Sigrist [35] saw a similar action in their analysis of previous data [8]. From our previous discussion of their paper, we know that they surmised that the number of domains contained in a junction can be derived from this maximum field using the following equation:

$$N \approx -\frac{2\pi\Phi_{mc}}{\Delta\phi\Phi_0} \tag{5.1}$$

where $\Delta\phi$ is the phase shift across the domain wall or walls and is in the range of 0.2 - 0.5. They define $\Phi_{mc} = d_{eff}LB_{mc}$, thus for $\lambda_s = 35$ nm, $d = 25$ nm, $\lambda_p = 160$ nm we

(a)

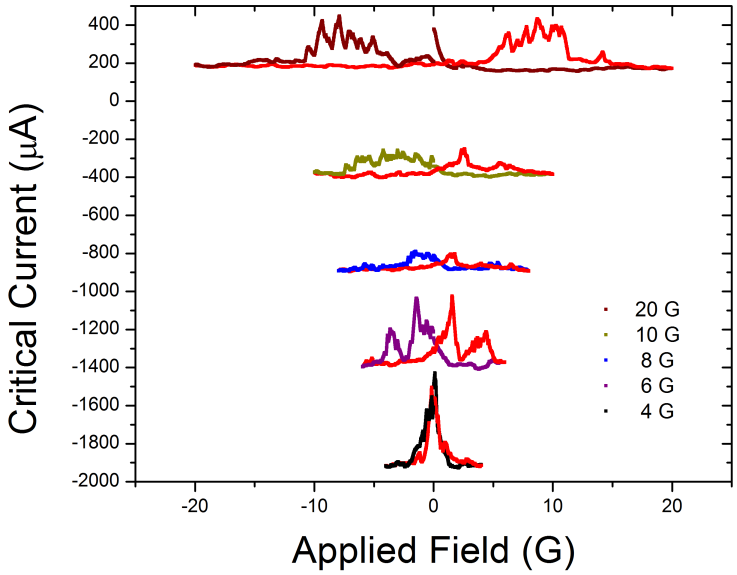


(b)

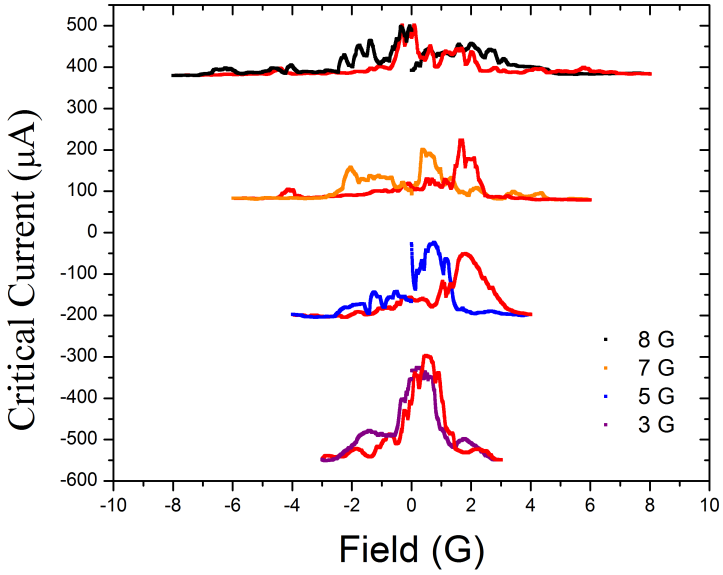


Figure 5.8: The junctions are from 2 different crystals. (a) 2 $\mu$m junction that has a well defined peak in the critical current. (b) 1 $\mu$m junction on the same crystal as the previous junction. The colored (red) curves all indicate scanning of the field in the positive (negative) field direction, or to the right (to the left). All scans begin at zero field and the field values indicated on the right of each graph define the span.

have for the 2 $\mu$m junction $\Phi_{mc} = 0.704$ G$\mu m^2 = 0.0352\Phi_0$ and for the 1 $\mu$m junctions $\Phi_{mc} = 0.132$ G$\mu m^2 = 0.0066\Phi_0$. These values give us $N_{2\mu m} \approx 0.44 \rightarrow 1.1$ domains and $N_{1\mu m} \approx 0.08 \rightarrow 0.2$ domains. However, let us take these values with some caution, as we have not determined the flux focusing in our junctions, causing these values to be slightly low. We will look at some data that helps us identify the flux focusing at the end of this section and will revise these estimates, but for now we can see that these values indicate we are in the correct size range on these junctions for observing single to multiple domain phase characteristics.

Figure 5.9 displays hysteresis effects in two 4 $\mu$m junctions fabricated on the same crystal. The crystal was polished but not annealed, so the critical current density varied across the face, as is evident in the figure. Figure 5.9a is a junction that displayed a $\pi$ phase shift across the junction that seems to remain with the hysteretic shifting of the pattern. This feature could indicate that the domain wall is near the center of the junction and slight shifts in the energy profile do not effect the overal phase shift in the junction, similar to Figure 3.13.

Figure 5.9b has a peaked critical current characteristic with high side lobes. This pattern was discussed in the previous section, but here we can see that the hyteresis tends to raise one side lobe over another, based on whether large positive or negative field has been applied. This behavior would be similar to what we would expect if the domain wall or walls were near the edges of the junction, as in Figure 3.14, and the subsequent shifting in the domain wall from high fields caused a significant phase change in the junction. Thus, the shifted patterns tend to look more like they are no longer peaked at the center.

If we again use (5.1) to define the number of domains in the junctions, we find for the Figure 5.9a that $\Phi_{mc} = 0.704$ G$\mu m^2 = 0.0352\Phi_0$ and for Figure 5.9b that $\Phi_{mc} = 0.616$ G$\mu m^2 = 0.0308\Phi_0$. This gives us domain values for these junctions of $N_{4\mu m,a} \approx 0.44 \rightarrow 1.1$ domains and $N_{4\mu m,b} \approx 0.39 \rightarrow 0.97$ domains.

Figure 5.10 shows two junctions that were deposited on a crystal that was polished and then annealed as described in Section 4.2. These junctions appear to be the cleanest

(a)

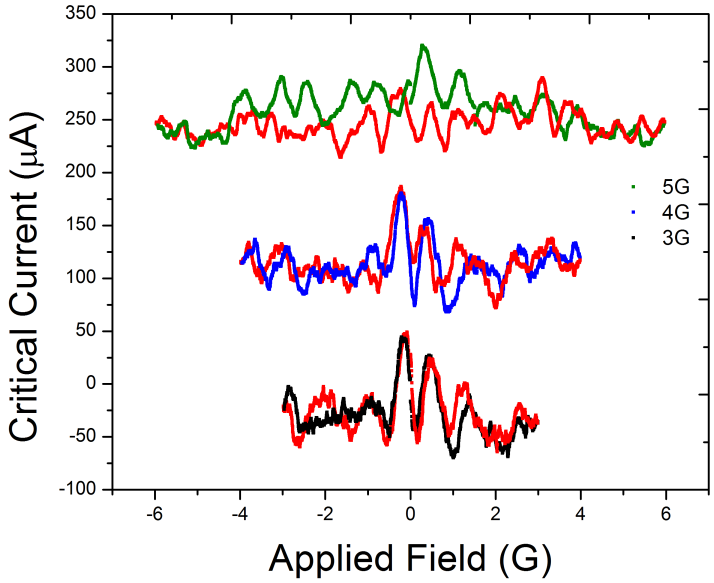


(b)

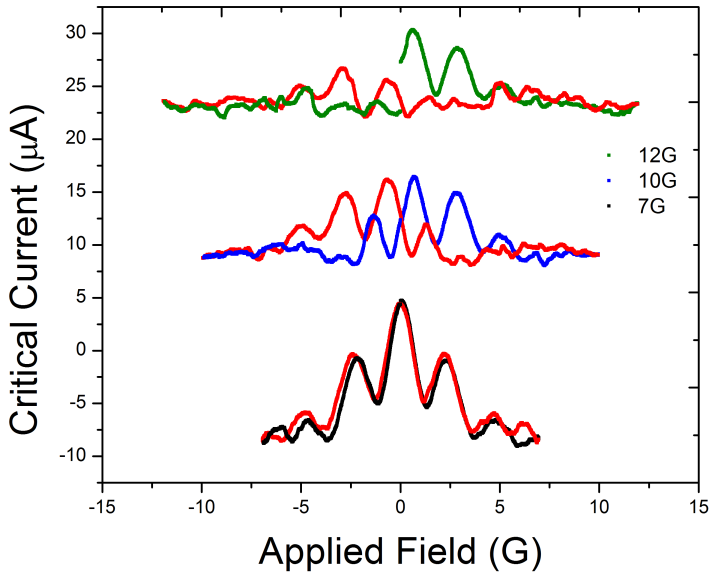


Figure 5.9: Both of the hysteresis patterns are from 4 $\mu$m junctions on that same polished crystal face. (a) has a critical current characteristic that is dipped in the center. (b) has a peaked characteristic with high side lobes. The colored (red) curves all indicate scanning of the field in the positive (negative) field direction, or to the right (to the left). All scans begin at zero field and the field values indicated on the right of each graph define the span.

(a)

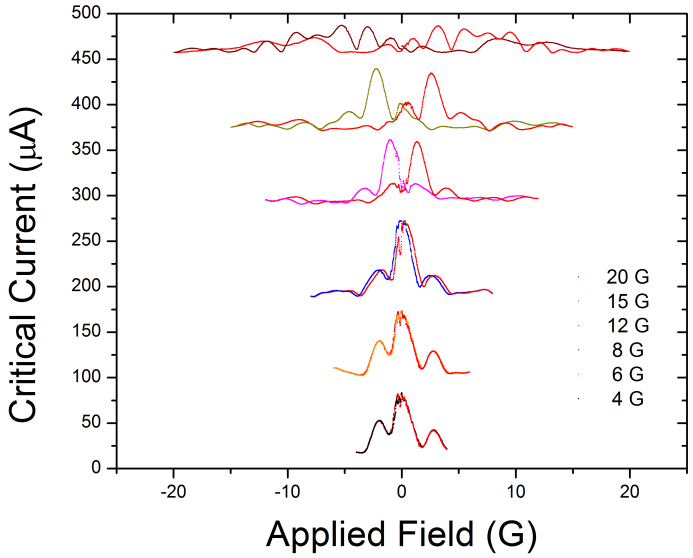


(b)

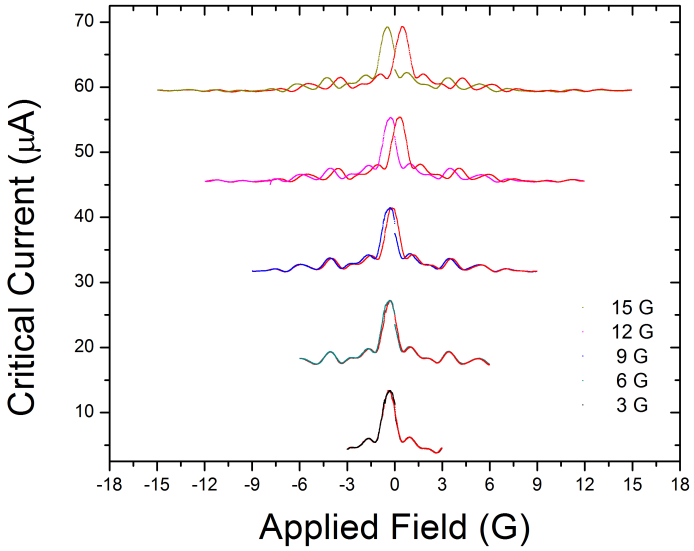


Figure 5.10: These junction were deposited on a polished and annealed crystal. (a) 4 $\mu$m junction that is peaked in center but slightly askew with high side lobes. (b) 500 nm junction which shows a very close to Fraunhofer like pattern. The colored (red) curves all indicate scanning of the field in the positive (negative) field direction, or to the right (to the left). All scans begin at zero field and the field values indicated on the right of each graph define the span.

and most well defined junctions measured during the course of this project. The hysteresis pattern in each is very distinct and Figure 5.10a shows suppression of the critical current peak with high field scans as previously observed. These junctions display most prominently the hysteresis effect in that there is a minimum field at which the junctions become hysteretic, and below this field they do not display hysteresis, contrary to what was observed in the prototype junction. It should also be pointed out that the hysteresis is much larger in the 4 $\mu$m junction with comparable field sweeps. However, it does seem that the critical field required to cause hysteresis is similar, approximately 7 G.

Before we follow through with the same analysis of the domain size as has been previously carried out, let us first look at a different data set taken on the 500 nm junction. We were interested in seeing if the hysteresis effect was due to the $Sr_2RuO_4$, or something else such as magnetic impurities in the normal metal barrier. To determine this, we decided to form a critical current characteristic where we field cooled the 500 nm junction at each point along the graph. We followed a standard procedure of warming above the $Sr_2RuO_4$ critical temperature of 1.5 K, applying the field for that point on the graph, then cooling again with the field still applied. Then we proceeded to take current versus voltage sweep and the critical current was noted. The whole process was repeated for the next field value and we built a critical current versus magnetic field plot from the data. The results are displayed below in Figure 5.11.

There is a distinct peak in Figure 5.11 but it is much wider than in previous data taken. Also, the data is very jagged and inconsistent from run to run due to flux trapping in the junction from the high fields the junction is cooled in. There is clearly some form of Fraunhofer envelope, but it is fairly obscured. However, we can see that even with these high fields applied to the crystal, there is no evidence of hysteresis. If we argue that there is flux focusing in our previous measurements, which is apparent from this measurement and generally true for most Josephson junctions, 15 G fields were shown to cause hysteresis in the crystal in our measurements and those same conditions seem to have no effect when

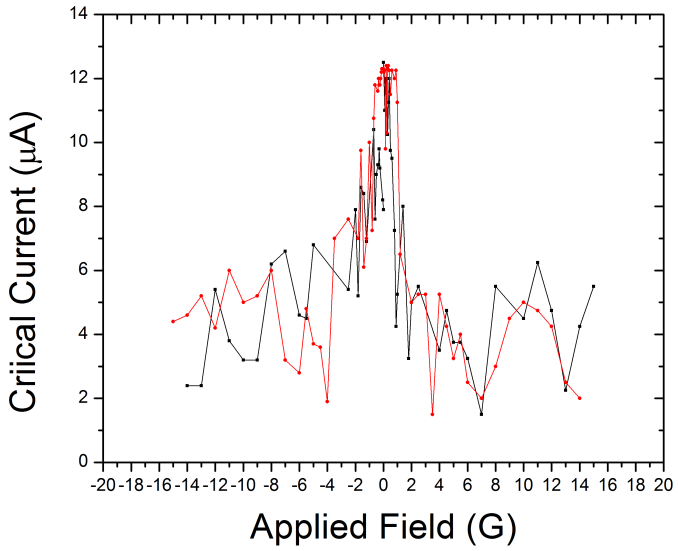


Figure 5.11: Critical current characteristic of a 500 nm junction that is field cooled at each point. There is a defined peak with only some indication of side lobes. The field sweep is large with little indication of hysteresis.

the system is field cooled. This fact leads us to the conclusion that whatever is causing the hysteresis in these systems must be from the p-wave superconductor, since it is the only parameter that was removed to make this measurement.

Let us also explore this measurement from a different angle. The data also gives us an important metric for the flux focusing in the junction. Since the field is evenly distributed during field cooling and the field can be broken into vortices in the crystal, much less magnetic field passes through the junction in this measurement than the previous measurements that were zero-field cooled. $H_{c1}^{ab}$ for $Sr_2RuO_4$ parallel to the $ab$-plane is $\sim$10 G, and $H_{c1}^{c}$ is 50G. It is interesting to note that $H_{c1}^{ab}$ is nearly the field required for hysteresis to set in for the current measurement, but the applied field direction is perpendicular. If we compare the width of the field cooled measurement to the zero field cooled measurement, we find 16G / 3.25G $\approx$ 4.5 as our flux focusing coefficient. To check this number, we know that the first trough in the interference pattern should come when a quantum of flux, $\Phi_0$, is applied to the junction. So we can calculate the flux focusing from our data as $dw\delta B_1 = \Phi_0$ where $d$ is

Table 5.1: Flux focusing values for variously sized junctions. $\delta$ is the flux focusing coefficient.

| Size | $\delta$ |
|---|---|
| 2 $\mu$m | 23 |
| 1 $\mu$m | 63 |
| 4 $\mu$m (from 5.9a) | 47 |
| 4 $\mu$m (from 5.9b) | 18 |
| 4 $\mu$m (from 5.10a) | 13 |
| 500 nm | 107 |

the effective thickness of the junction, $w$ is the width, $\delta$ is the the flux focusing coefficient and $B_1$ is the field of the first trough. We find $\delta = \frac{\Phi_0}{(220nm)(500nm)(1.75G)} \approx 107$. This fits with the idea that it should take approximately 180G to modulate a 500 nm junction. The focusing value for each junction measured is listed in Table 5.1 based on the simulations we have done in Figures 3.13 and 3.14.

We can also make an outside estimate for what the maximum flux focusing in the junctions could be based on geometry. We can assume that all of the field that is applied to the crystal is instead expelled to an an area at the edge of the crystal within a penetration depth of the surface. Under this assumption, the ratio of the areas would be equivalent to $\delta_{max}$ for our sample as the flux through the crystal must remain constant. For the crystal pictures in Figure 4.7 we have a crystal that is $\sim$1.4mm square and $\lambda_p = 160$ nm. Thus, our $\delta_{max} \approx 2200$.

In light of these coefficients, we can calculate new values for the number of domains in both the most recent junctions and the previously calculated ones. First we calculate new values for the previous samples simply by multiplying the flux by the flux focusing coefficient, and thus the number of domains by extension. Therefore, we have $N_{2\mu m} \approx 10.1 \rightarrow 25.3$ domains which corresponds to a domain size range of $L_{dom,2\mu m} \approx 79$ nm $\rightarrow 198$ nm. For $N_{1\mu m} \approx 5.04 \rightarrow 12.6$ domains, we have domain sizes of $L_{dom,1\mu m} \approx 81$ nm $\rightarrow 198$ nm.

We can also recalculate the values for the 4 $\mu m$ junctions in the same manner. For $N_{4\mu m,a} \approx 20.68 \rightarrow 51.7$ and $N_{4\mu m,b} \approx 7.04 \rightarrow 19.2$ which from the highest and lowest values gives us domains sizes ranging from $L_{dom,4\mu m} \approx 77$ nm $\rightarrow 571$ nm.

Finally, let us calculate the same values for our most recent samples. For the 4 $\mu$m junction in Figure 5.10a we have $\Phi_{mc} = 29.744$ G$\mu m^2 = 1.4872\Phi_0$. For the 500 nm junction in Figure 5.10b we have $\Phi_{mc} = 26.482$ G$\mu m^2 = 1.32\Phi_0$. These values give us domain numbers and sizes as follows:

$$N_{4\mu m} \approx 4.6 \rightarrow 10.4 \Rightarrow L_{dom,4\mu m} \approx 385nm \rightarrow 870nm \tag{5.2}$$

$$N_{500nm} \approx 3.7 \rightarrow 9.25 \Rightarrow L_{dom,500nm} \approx 54nm \rightarrow 135nm \tag{5.3}$$

These values indicate a large number of domains and do not necessarily reflect what we are seeing in our data. If our argument is that the domain shift could be $\pi$ or $\pi/2$ at the domain walls, we find different sizes associated with the domains. Table 5.2 shows some values for these various phase differences at the domain wall. We will continue to assume that $\Delta\phi = 0.2 \rightarrow 0.5$ and simply add the appropriate phase shift to it in each case.

Table 5.2: A list of various junctions that were measured with their corresponding flux focusing coefficient. We have included various phase shifts across the domain walls as listed in the column headers.

| Size | $\delta$ | $\Delta\phi = 0.2 \rightarrow 0.5$ | $\Delta\phi + \pi/2$ | $\Delta\phi + \pi$ |
|---|---|---|---|---|
| 2 $\mu$m | 23 | 79 nm $\rightarrow$ 198 nm | 124 nm $\rightarrow$ 311 nm | 248 nm $\rightarrow$ 622 nm |
| 1 $\mu$m | 63 | 81 nm $\rightarrow$ 198 nm | 127 nm $\rightarrow$ 311 nm | 254 nm $\rightarrow$ 622 nm |
| 4 $\mu$m (from 5.9a) | 47 | 77 nm $\rightarrow$ 193 nm | 121 nm $\rightarrow$ 303 nm | 241 nm $\rightarrow$ 606 nm |
| 4 $\mu$m (from 5.9b) | 18 | 208 nm $\rightarrow$ 571 nm | 327 nm $\rightarrow$ 897 nm | 653 nm $\rightarrow$ 1.8 $\mu$m |
| 4 $\mu$m (from 5.10a) | 13 | 385 nm $\rightarrow$ 870 nm | 605 nm $\rightarrow$ 1.37 $\mu$m | 1.2 $\mu$m $\rightarrow$ 2.73 $\mu$m |
| 500 nm | 107 | 54 nm $\rightarrow$ 135 nm | 85 nm $\rightarrow$ 212 nm | 170 nm $\rightarrow$ 424 nm |

We have assumed in this project that we are addressing single and multiple domain junctions and this assumption seems to be verified by the critical current characteristics we showed in Figure 5.4. From the calculations in Table 5.2 we must conclude then that the phase shift is of order $\pi$ to obtain domain sizes large enough to describe our results. This assumption is supported by the critical current characteristics we have seen, especially the ones that have a minimum at zero magnetic field. We also can conclude that there needs to be more theoretical analysis of this system as the model put forth by Bouhon and Sigrist [35] appears incomplete.

### 5.3.2 Field Cooling Effects in Junctions

Another interesting feature of our junctions reflects something seen previously in measurements of field cooled junctions, namely an enhancement of the critical current when cooled in a small field [9] as shown in Figure 5.12. In these previous measurements, junctions with small critical current peaks were shown to have a significant increase in the peak height when cooled in a very small field. It was also seen that there was a significant memory effect in the field cooling, such that there was residual enhancement of the critical current after it had been field cooled for up to a day as shown in Figure 5.13. We proceeded with some field cooling studies of our own based on these initial findings.

Let us first examine the procedure we used for field cooling the junctions. It is similar to the procedure we used in the field cooled at every point critical current characteristic from the previous subsection. We warmed the crystal above the critical temperature and then applied a small magnetic field. In this case, we never applied large fields as in the previous measurement. We then cooled the junctions to base temperature, then the field was reduced to zero. We proceeded to measure the critical current as a function of magnetic field as we had previously. However, in this case, we used field spans that attempted to keep the critical current patterns non-hysteretic. This allowed us to more easily see effects from the actual cooling without adding in more complexity from hysteresis in the patterns.

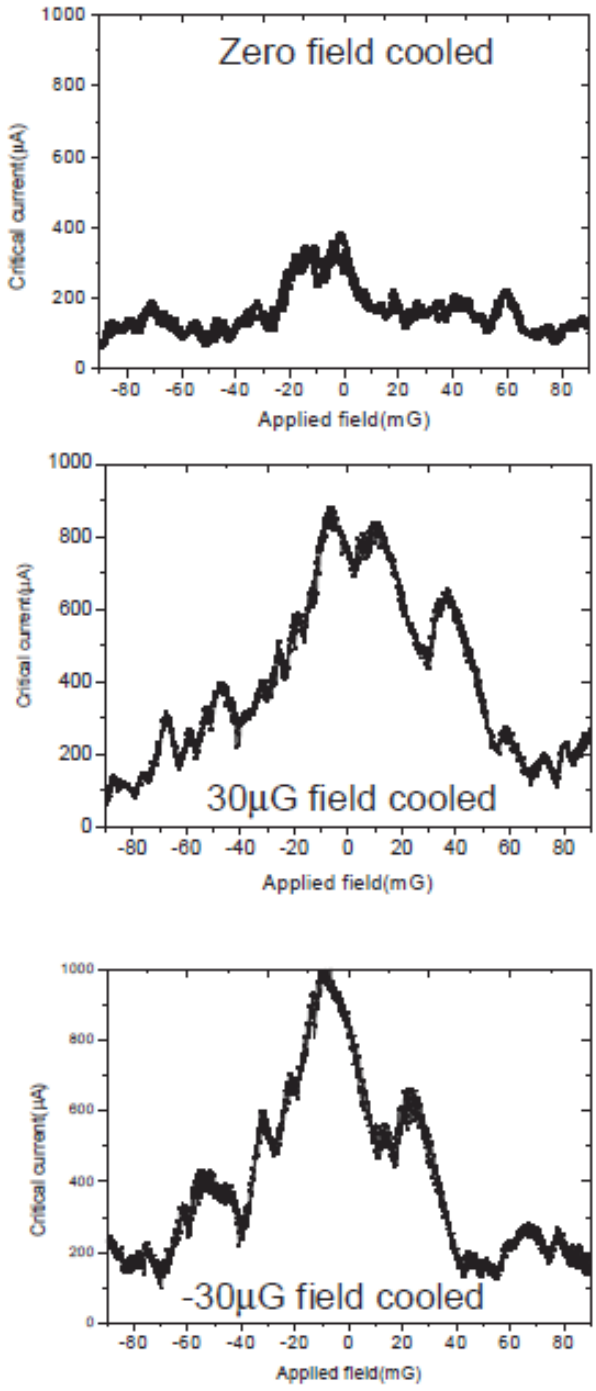


Figure 5.12: Field Cooling data from [9]. The critical current is enhanced with field cooling in the directions shown on the graphs.

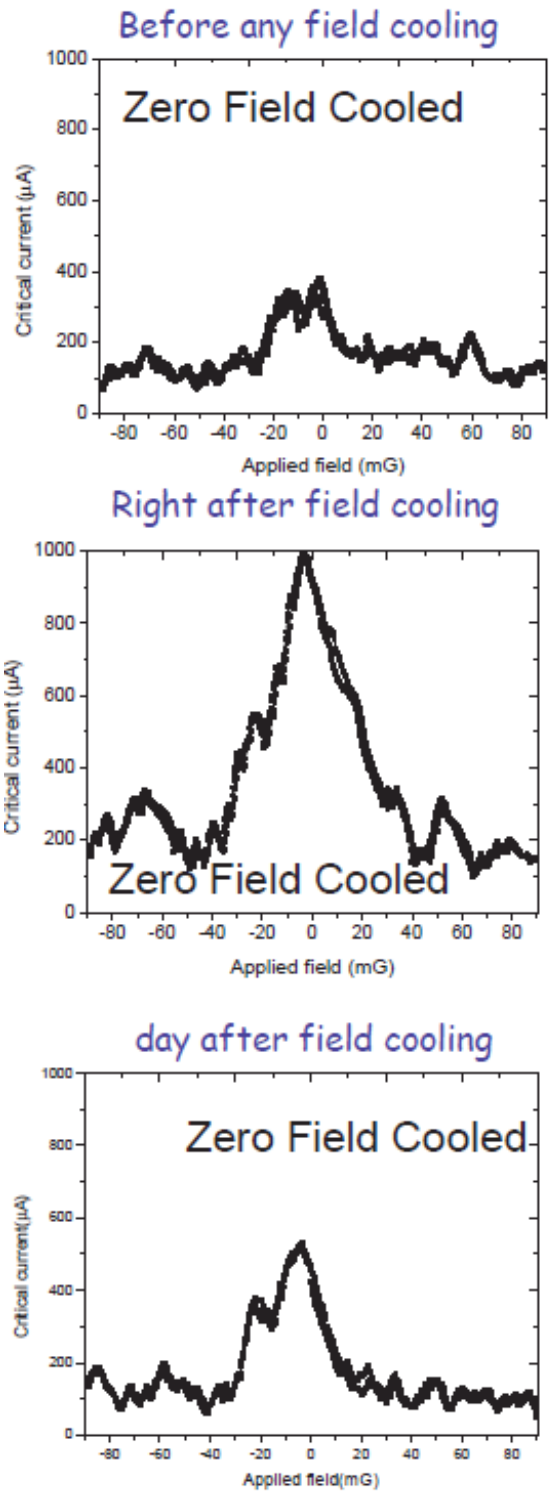


Figure 5.13: Field Cooling memory effect as shown in [9]. The critical current enhancement could last up to a day.

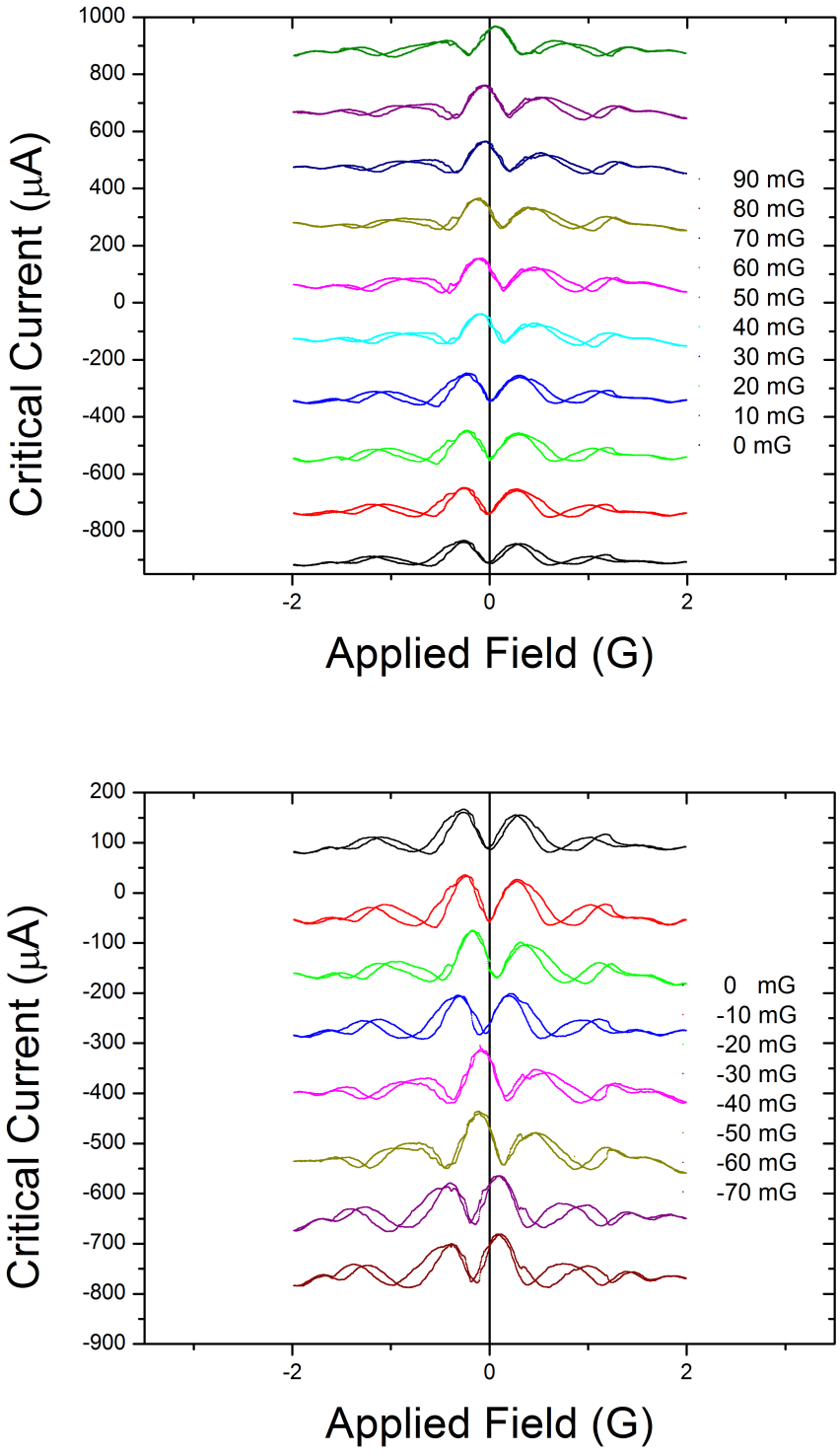


Figure 5.14: Field cooled critical current characteristics for a 4 $\mu$m junction. Field cooling values are listed on the right in ascending order. Significant shifts the center of the pattern are evident for different field values.

Figure 5.14 displays a typical field cooled 4 $\mu$m junction. There is no enhancement of the critical current as in previous experiments on larger junctions. However, we do see a shift in the center of the pattern as the field cooling value is increased. Over successive runs, the center of the pattern moves from being low critical current to higher critical current. This aspect indicates a change in the phase across the junction. Most intriguing is that in both cases, this phase shift change is large, going from what would be considered a $\pi$ total phase shift at 0 mG field cooling to 0 total phase shift at 90 mG field cooling.

We also observe that this change in the phase shift is not continuous, but instead has a step like feature. In both positive and negative field cooling values, the first four characteristics are nearly the same, as are the next two. After this the phase shift is no longer similar, but this indicates that there is some sort of energy threshold that is required to change the phase shift across the junction. The fact that there seems to be little difference in the field cooling direction up to 50 mG is surprising.

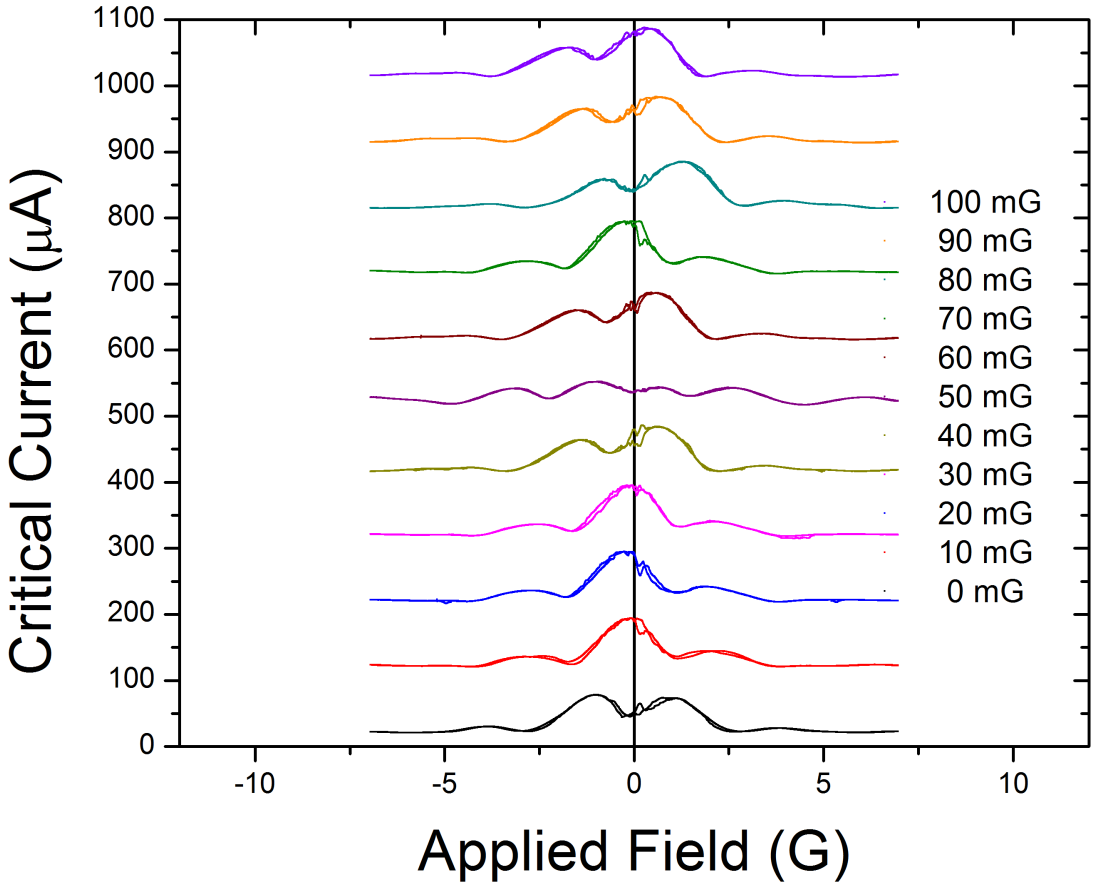


Figure 5.15: Field cooled polished/annealed 4 $\mu$m junction as shown in Figure 5.10a. Field steps only in positive direction. Same junction as was measured above in hysteresis measurements.

Figure 5.15 is similar to the previous data set in some interesting ways. It appears that the initial zero field cooled characteristic was not entirely stable as a small field was able to change it to a Fraunhofer-like pattern. Taking this into account, we can then see that again, this sample has similar characteristics up to about 30 mG and then the pattern changes. It is interesting that the pattern seems to melt at 50 mG and then reform, as 50 mG was also the field that the previous data seemed to diverge between positive and negative field coolings, and the patterns again become much less stable above that value.

It should also be noted that there is a hysteretic switching effect around 100 mG during

the field scan, and this event does not move as the pattern shifts. We simply point this out to show that though there may be some mobility in what is happening with the phase, there is something deeper at work here that has little to do with the phase shift across the junction. In a later section, we will examine these switches more closely, but we wanted to highlight this feature now as it will be relevant to our domain discussion.

Figure 5.16 shows field cooling effects on 500 nm junctions, which should be smaller than the domain size based on our previous analysis. Before we analyze this data, let us first point out that the field cooling range is much larger in this case than the previous. We were interested to see if there were effects farther out than 100 mG without approaching a point where vortices might form in the crystal. In the positive field cooling we see that there is a slight shift in the phase around 80 mG, but the shift is only $\frac{\pi}{2}$ rather than the larger shift seen with the 4 $\mu$m junctions. The shift also seems to go away above 140 mG of field cooling. In the negative direction, we see something different. There are a few intermittent critical current characteristics that show a slight shift, but for the most part the pattern is mostly Fraunhofer in appearance. This feature is what we would expect for a junction without any domains. It is possible that the phase shift is due to proximity to a domain wall, but further simulations and theory is necessary to determine if proximity to a domain can cause phase shifting in a junction.

There is no current theory that can explain the phase switching we are seeing in these field cooling studies. Our intuition tells us that it is possible that it is becoming energetically favorable for the domain wall to switch to a different pinning site depending on the magnetic field it is cooled in, but without a better model this is only conjecture. However, we see no possible way that we could replicate this result without these junctions addressing very few domains.

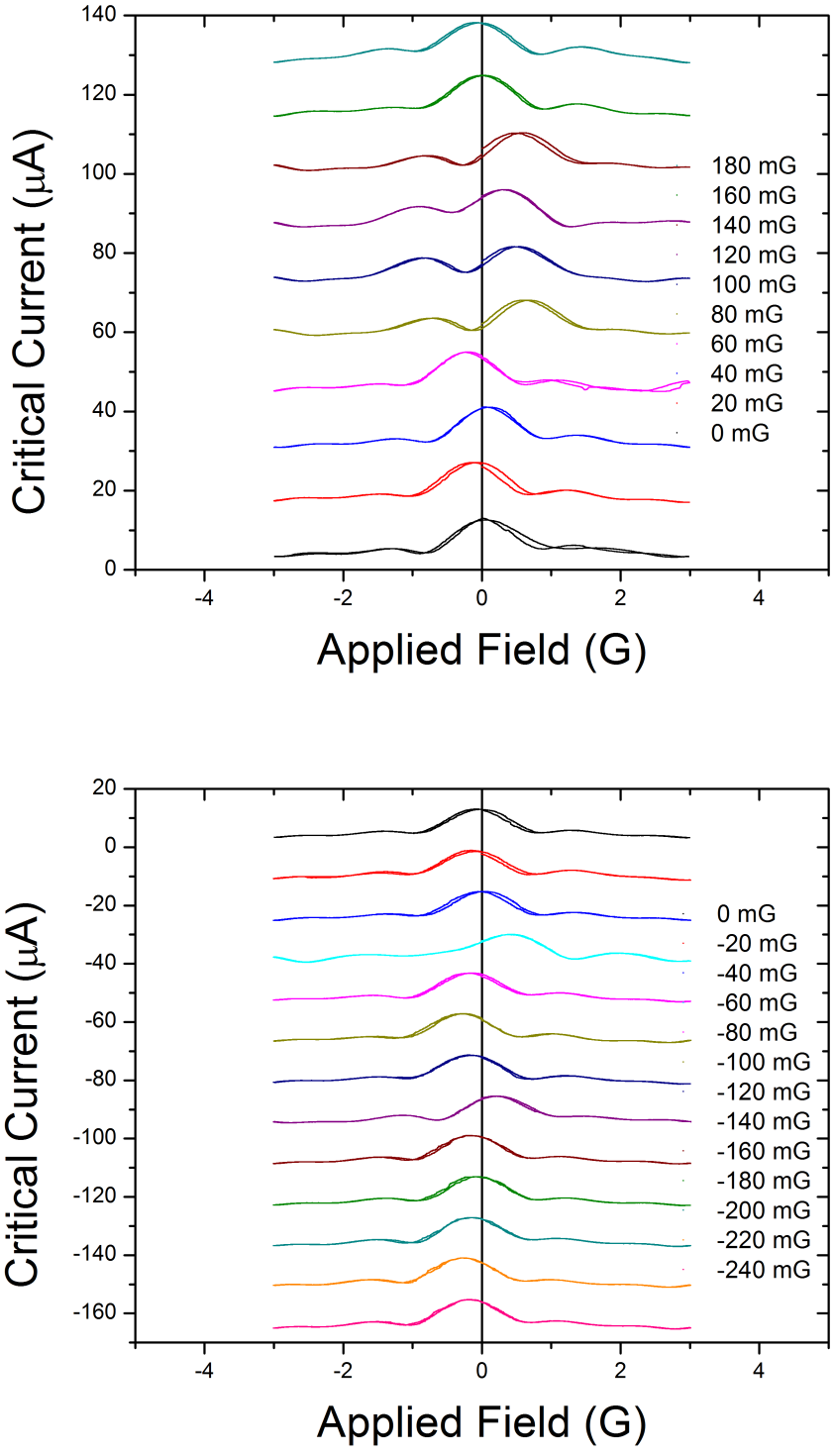


Figure 5.16: Field cooled critical current characteristics of a 500 nm junction also shown in Figure 5.10b. Field steps in this case are larger and the field cooling spans a larger range. The smaller junction has much more stable patterns with field cooling.

### 5.3.3 Switching in Junctions

The final aspect of these junctions we wish to discuss is switching around the peak of the critical current. If we look closer at Figure 5.3 there is some switching features around the peak. Figure 5.17 is a small scan around this peak and highlights this switching behavior.

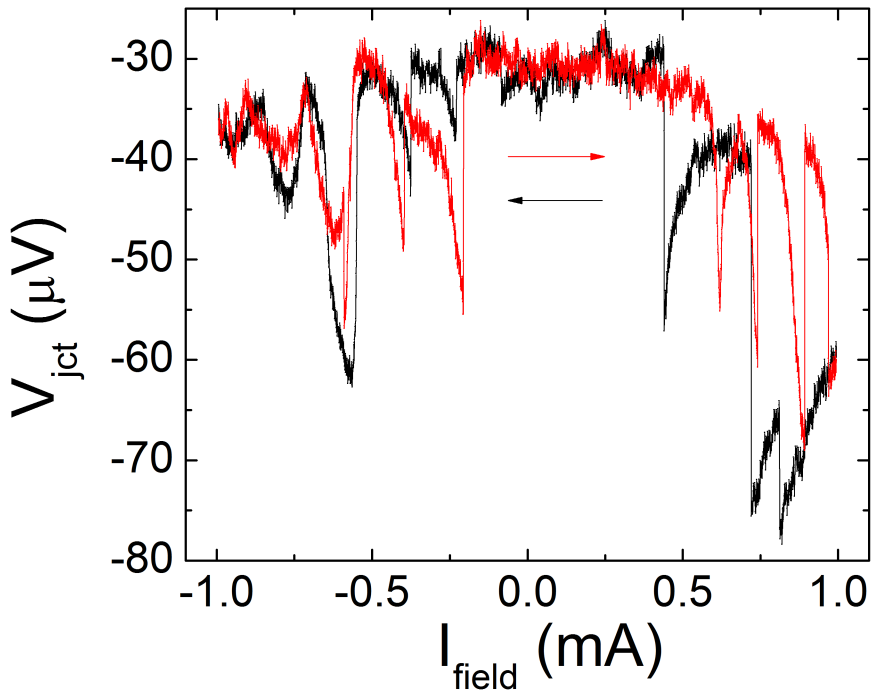


Figure 5.17: Small scan of peak of the 500 nm prototype junction from Figure 5.3. Voltage scan shows anomolous switching around critical currnet peak that could be associated with vertical domain alignment.

The switching behavior in Figure 5.17 is reminiscent of magnetic switching effects in S-F heterostructures [40]. It also is similar to vortex entry in the junction. There have been some comments that the domains exist in the crystal plane and that interlayer domains may not be exactly lined up. These switches could also be a signature of these domains realigning, but without further analysis we can only speculate. Instead let us look at the various features of these junctions to better define the problem.

In Figure 5.18 we compare two scans taken over the same range. The switching features

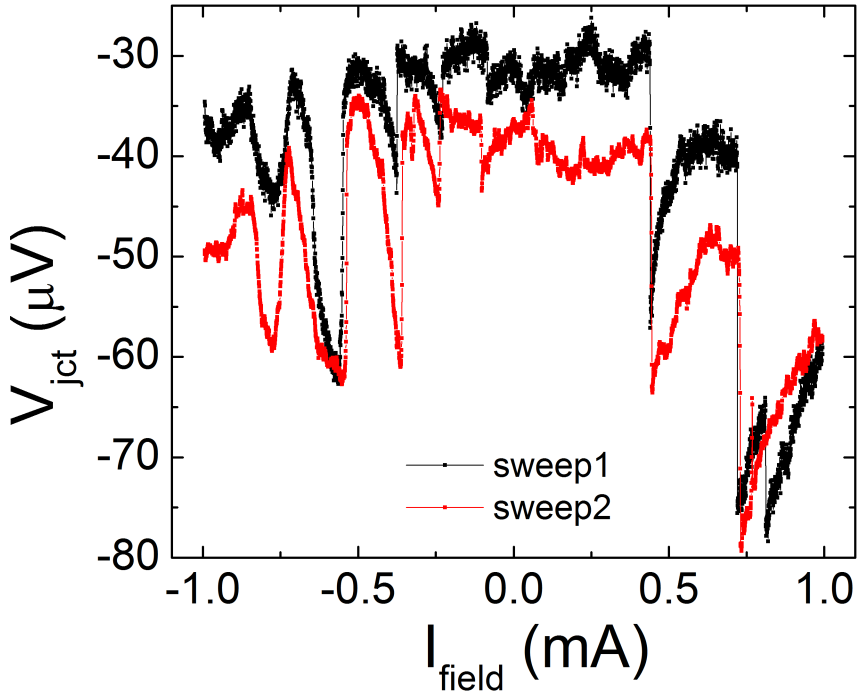


Figure 5.18: Multiple positive direction sweeps taken on the critical current peak of the 500 nm junction from Figure 5.3. Though the magnitude of the switchess tends to change between scans, the placement of the is nearly the same.

are identical between the two scans though the magnitude of the effect seems to change slightly from run to run. These data seem to verify that the effect is robust and intrinsic to the junction. If the switches were random noise or due to something in the setup, they would not necessarily repeat so dramatically at the same field values. Particularly interesting is the initial positive field switch, as both traces appear to jump nearly the same amount. With these switches being so robust, we decided to attempt to zoom in on single jumps to characterize them better.

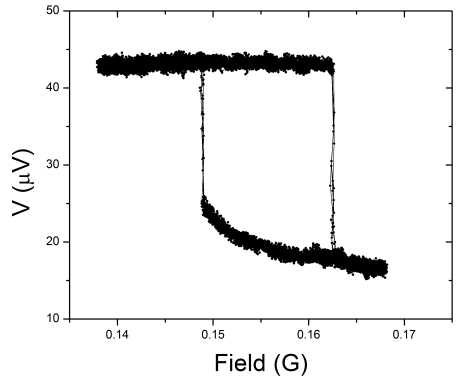


(a)

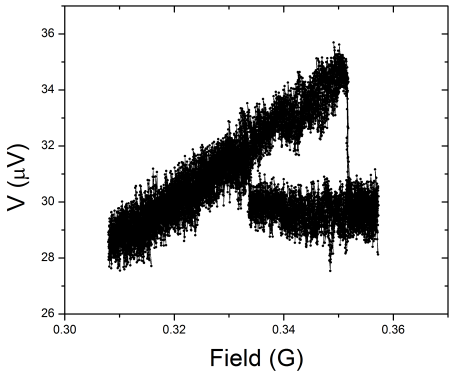


(b)

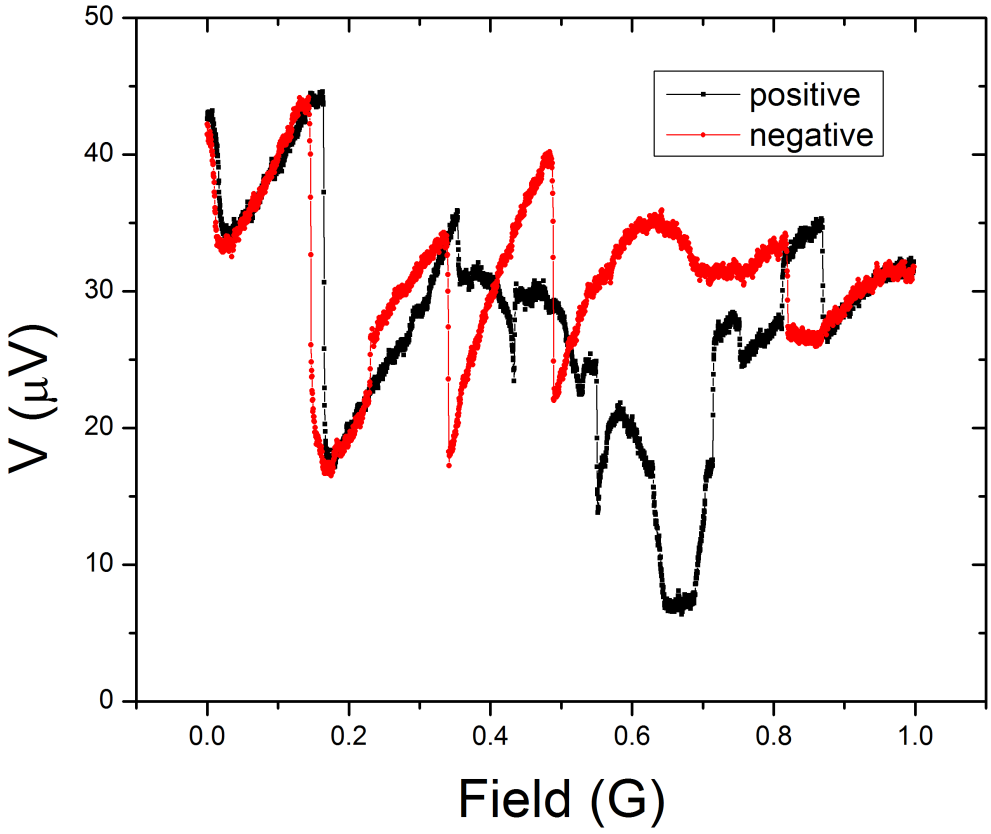


(c)

Figure 5.19: Scans from the critical current peak from Figure 5.8b of a 1 $\mu$m junction. (a) and (b) are typical hysteretic switches. Each switch was ramped over 5 times. (c) Larger scan showing the same region as the switches in (a) and (b). Of note, switch (a) is very distinctly the left hysteretic switch on the large scan.

The switches in Figure 5.19a and 5.19b are from scans across the top of the critical current peak of the 1 $\mu$m junction in Figure 5.8b. Each switch was scanned across 5 times to measure how robust the switch was. In both cases, the switches show no change in the switch point. The larger scan across the top is also interesting. On the left side of the scan we can see the switch from Figure 5.19a and both sides of it show up the same as in the smaller scan. This scan was taken a number of times and the switches it displays are of a similar robustness as the comparison graph in Figure 5.18. The only way to change this scan was by increasing the scan range to include negative field. This action changed the placement of the switches as seen in Figure 5.20.

Overall, these switching features are interesting but do not have a good explanation in current theory. It's possible that they are a signature of vortex movement through the junction, similar to something Sigrist and Agterberg described in a paper on domain walls [41]. The origin could also be from a possible c-axis misalignment of the domains. If there was slight misalignment at zero field, switching in the critical current as they align could give rise to a switching signature in the critical current. However, at this time, these data fit no real model and have not been previously observed.

## 5.4 Discussion of Results

Much of our work was motivated by the amount of measurements taken previously showing both domain signatures or null results. Catherine Kallin and A J Berlinsky recently compiled many of the experiments performed on $Sr_2RuO_4$ to date to analyze TRS-breaking [42]. Their focus was mainly on why the scanning SQUID measurements were not seeing the expected result, namely circulating screening fields around the domain boundaries. However, their paper makes a very good point; much of the data taken to date on $Sr_2RuO_4$ has been contradictory to data previously taken using other techniques. We would also like to highlight that specifically the $\mu$SR and Polarized Kerr Effect seem to be the hardest results to overlook.

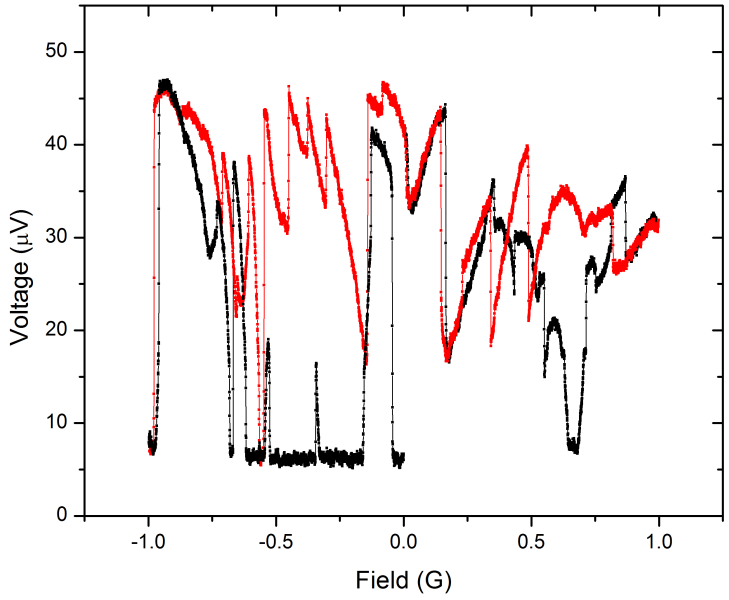


(a)

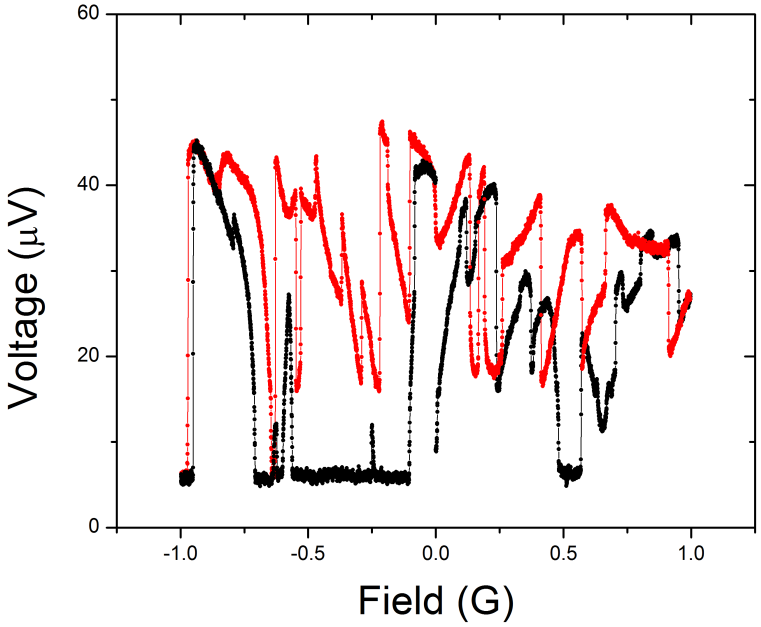


(b)

Figure 5.20: Two scans of the same critical current peak of 1 $\mu$m junction in Figure 5.8b. Of note is that the positive side of (a) is the same as Figure 5.19c. The switching changes in (b), which was taken immediately after (a).

Whether domains exist, as we believe, the fact that the order parameter is TRS breaking seems to be a solid conclusion. Table 5.3 is a recreation of a table Kallin and Berlinsky put in their paper, and adding our data to this table seems to indicate that there is a lot of data supporting both TRS breaking and a small domain size.

Table 5.3: Comparison of experiments on $Sr_2RuO_4$ TRS Breaking. From [42] with our experimental findings added.

| Experiment | TRSB? | Estimated Domain Size |
|---|---|---|
| $\mu$SR | Yes | $< 2\mu$m |
| Polar Kerr Effect | Yes | $> 50\mu$m (15-20 $\mu$m) with (without) field cooling |
| Scanning Hall Probe | No | $< 1\mu$m |
| Scanning SQUID | No | $< 2\mu$m |
| Josephson Junction Tunneling | Yes | $< 1\mu$m ($0.5\mu$m dynamic) |
| Josephson Nano-Junction Tunneling | Yes | 200nm$-1.5\mu$m |
| SQUID Tunneling | Parity | $> 10 - 50\mu$m |
| SQUID Corner Junction | Yes | $> 10\mu$m |

In the end, our results seem to back up the results obtained by Kidwingira *et al.*, though in some ways are more sensitive and provide a cleaner picture of the domains. Our data indicates a possible $\pi$ shift across the domain walls. As we compare our data to the simulations from Figures 3.13 and 3.14, we can only conclude that we are addressing a few to possibly one domain in many of these instances.

# Chapter 6

# Conclusions and Future Work

We have presented here more evidence for chiral domains in $Sr_2RuO_4$. Our small junctions were able to probe what we believe were single domain and two domain structures, along with possible multiple domain structures. We see evidence for this in the graphs in Figure 5.4. The junctions that are above 2 $\mu$m in size show interesting non-Fraunhofer characteristics in their interference patterns. The junctions at and below 2$\mu$m show closer to a Fraunhofer envelope, with the 500 nm junction looking most distinctly like a Fraunhofer pattern. These facts lead us to conclude that we successfully interacted with single domains in this project.

We also studied hysteresis in the junctions and used it as a tool to explore both the domain size and flux focusing. It is possible that this hysteretic behavior is coming from the mechanism proposed by Bouhon and Sigrist [35], but there are discrepencies between that model and our data that seem to indicate the theory is not complete. We observed $\pi$ phase shifts across domain walls, indicating that phase changes across the domain walls could be large. In some cases, we also observed significant shifting in the phase of the interference pattern when the pattern became hysteretic. Overall, there is still much that needs to be understood about the hysteresis in these junctions. We attempted to show that the hysteresis was due to $Sr_2RuO_4$ by making field cooled measurements at every point along the critical current characteristic. This measurement showed no hysteresis and we conlude that the hysteresis is due to a mechanism in the p-wave superconductor. We also used the hysteresis to constrain the domain size to $\leq$1$\mu$m, and possibly as small as 200 nm.

An interesting project that would further narrow the cause of this hysteresis would be to apply fields to the junction that are also parallel to the *ab*-plane, rather than perpendicular.

If the interference pattern was non-hysteretic in these applied fields, we could conclude that hysteresis is due to effects in the *ab*-plane. A new measurement setup with two perpendicular Helmholtz coils would be required to perform this experiment.

Our field cooling data shows a significant divergence from previous work by Kidwingira [8, 9], namely we see no enhancement of the critical current. Instead, as the junctions are field cooled and then the critical current interference pattern is measured, we see a change in the phase of the interference pattern. It is possible that this phase change orignates from the domain walls switching to new pinning sites, but we have no theoretical support for this conjecture. We can conclude that the junctions must be addressing very few domains for these results to be so defined and reproducible.

We have also looked at switching behavior in these junctions. We observed reproducible switching patterns and stable hysteretic jumps in the critical current. It is possible that these effects are from misalignment of the domains along the c-axis or from flux entry into the junction as described by Sigrist and Agterberg [41]. The previous experiment that we proposed would go a long way in establishing the origin of the switching. If the switching behavior disappeared with a change in field direction it is entirely possible that the switching is coming from the domains as nature of flux flow across the junction would be completely different.

$Sr_2RuO_4$ is a very complex superconductor with many interesting features such as triplet-pairing of the order parameter, chiral order parameter domains, and signatures of half quantum vortices. We believe that we have positively added to the experimental knowledge that has been compiled thus far on the domain structure of the order parameter. The picture of the superconducting state is more clear and we have opened new avenues of study and questions for future researchers.

# References


[1] H. Onnes, "The resistance of pure mercury at helium temperatures," *Leiden Comm. 120b*, 1911.

[2] L. Landau and V. Ginzburg, "On the theory of superconductivity," *Journal of Experimental and Theoretical Physics (USSR)*, vol. 20, p. 1064, 1950.

[3] J. Bardeen, L. Cooper, and J. Schrieffer, "Theory of superconductivity," *Physical Review*, vol. 108, no. 5, p. 1175, 1957.

[4] A. Abrikosov, "Magnetic properties of superconductors of the second group," *Sov. Phys.-JETP (Engl. Transl.);(United States)*, vol. 5, no. 6, 1957.

[5] J. G. Bednorz and K. A. Müller, "Possible high $T_c$ superconductivity in the Ba-La-Cu-O system," *Zeitschrift fur Physik B Condensed Matter*, vol. 64, pp. 189–193, 1986.

[6] P. Monthoux, A. Balatsky, and D. Pines, "Toward a theory of high-temperature superconductivity in the antiferromagnetically correlated cuprate oxides," *Physical review letters*, vol. 67, no. 24, pp. 3448–3451, 1991.

[7] D. A. Wollman, D. J. Van Harlingen, W. C. Lee, D. M. Ginsberg, and A. J. Leggett, "Experimental Determination of the Superconducting Pairing State in YBCO from the Phase Coherence of YBCO-Pb dc SQUIDs," *Physical Review Letters*, September 1993.

[8] F. Kidwingira, J. D. Strand, D. J. Van Harlingen, and Y. Maeno, "Dynamical Superconducting Order Parameter Domains in $Sr_2RuO_4$," *Science*, vol. 314, no. 1267, 2006.

[9] F. Kidwingira, *Superconducting order parameter domains in $Sr_2RuO_4$ probed by Josephson Interferometry*. PhD thesis, University of Illinois at Urbana-Champaign, 2007.

[10] A. Mackenzie and Y. Maeno, "The superconductivity of $Sr_2RuO_4$ and the physics of spin-triplet pairing," *Reviews of Modern Physics*, vol. 75, no. 2, p. 657, 2003.

[11] A. Mackenzie, S. Julian, A. Diver, G. McMullan, M. Ray, G. Lonzarich, Y. Maeno, S. Nishizaki, and T. Fujita, "Quantum oscillations in the layered perovskite superconductor $sr_2ruo_4$," *Physical review letters*, vol. 76, no. 20, pp. 3786–3789, 1996.

[12] T. Rice and M. Sigrist, "$Sr_2RuO_4$: an electronic analogue of 3He?," *Journal of Physics: Condensed Matter*, vol. 7, p. L643, 1995.

[13] C. Bergemann, J. Brooks, L. Balicas, A. Mackenzie, S. Julian, Z. Mao, and Y. Maeno, "Normal state of the unconventional superconductor $Sr_2RuO_4$ in high magnetic fields," *Physica B: Condensed Matter*, vol. 294, pp. 371–374, 2001.

[14] K. Ishida, H. Mukuda, Y. Kitaoka, K. Asayama, Z. Mao, Y. Mori, and Y. Maeno, "Spin-triplet superconductivity in $Sr_2RuO_4$ identified by 17O Knight shift," *Nature*, vol. 396, no. 6712, pp. 658–660, 1998.

[15] P. Anderson, "Theory of dirty superconductors," *Journal of Physics and Chemistry of Solids*, vol. 11, no. 1-2, pp. 26–30, 1959.

[16] A. Mackenzie, R. Haselwimmer, A. Tyler, G. Lonzarich, Y. Mori, S. Nishizaki, and Y. Maeno, "Extremely Strong Dependence of Superconductivity on Disorder in $Sr_2RuO_4$," *Physical review letters*, vol. 80, no. 1, pp. 161–164, 1998.

[17] A. Mackenzie, R. Haselwimmer, A. Tyler, G. Lonzarich, Y. Mori, S. Nishizaki, and Y. Maeno, "Erratum: Extremely Strong Dependence of Superconductivity on Disorder in $Sr_2RuO_4$[Phys. Rev. Lett. 80, 161 (1998)]," *Physical Review Letters*, vol. 80, no. 17, pp. 3890–3890, 1998.

[18] M. Sigrist and K. Ueda, "Phenomenological theory of unconventional superconductivity," *Reviews of Modern physics*, vol. 63, no. 2, p. 239, 1991.

[19] G. Luke, Y. Fudamoto, K. Kojima, M. Larkin, J. Merrin, B. Nachumi, Y. Uemura, Y. Maeno, Z. Mao, Y. Mori, *et al.*, "Time-Reversal Symmetry Breaking Superconductivity in $Sr_2RuO_4$," *Arxiv preprint cond-mat/9808159*, 1998.

[20] G. Luke, Y. Fudamoto, K. Kojima, M. Larkin, B. Nachumi, Y. Uemura, J. Sonier, Y. Maeno, Z. Mao, Y. Mori, *et al.*, "Unconventional superconductivity in $Sr_2RuO_4$," *Physica B: Condensed Matter*, vol. 289, pp. 373–376, 2000.

[21] J. Xia, Y. Maeno, P. Beyersdorf, M. Fejer, and A. Kapitulnik, "High Resolution Polar Kerr Effect Measurements of $Sr_2RuO_4$: Evidence for Broken Time-Reversal Symmetry in the Superconducting State," *Physical review letters*, vol. 97, no. 16, p. 167002, 2006.

[22] P. Bj
"ornsson, Y. Maeno, M. Huber, and K. Moler, "Scanning magnetic imaging of $Sr_2RuO_4$," *Physical Review B*, vol. 72, no. 1, p. 012504, 2005.

[23] J. Kirtley, C. Kallin, C. Hicks, E. Kim, Y. Liu, K. Moler, Y. Maeno, and K. Nelson, "Upper limit on spontaneous supercurrents in $Sr_2RuO_4$," *Physical Review B*, vol. 76, no. 1, p. 014526, 2007.

[24] C. Hicks, J. Kirtley, T. Lippman, N. Koshnick, M. Huber, Y. Maeno, W. Yuhasz, M. Maple, and K. Moler, "Limits on superconductivity-related magnetization in $Sr_2RuO_4$ and $PrOs_4Sb_12$ from scanning SQUID microscopy," *Physical Review B*, vol. 81, no. 21, p. 214501, 2010.

[25] M. Matsumoto and M. Sigrist, "Quasiparticle States near the Surface and the Domain Wall in a $p_x \pm ip_y$-Wave Superconductor," *Journal of the Physical Society of Japan*, vol. 68, no. 3, pp. 994–1007, 1999.

[26] G. Volovik and V. Mineev, "Line and point singularities in superfluid He 3," *JETP Lett*, vol. 24, no. 11, 1976.

[27] M. Cross and W. Brinkman, "Textural singularities in the superfluid A phase of 3 He," *Journal of Low Temperature Physics*, vol. 27, no. 5, pp. 683–686, 1977.

[28] J. Jang, D. Ferguson, V. Vakaryuk, R. Budakian, S. Chung, P. Goldbart, and Y. Maeno, "Observation of half-height magnetization steps in $Sr_2RuO_4$," *Science*, vol. 331, no. 6014, p. 186, 2011.

[29] V. Geshkenbein, A. Larkin, and A. Barone, "Vortices with half magnetic flux quanta in"heavy-fermion"superconductors," *Phys. Rev. B: Condens. Matter;(United States)*, vol. 36, no. 1, 1987.

[30] M. Sigrist and T. Rice, "Paramagnetic Effect in High $T_c$ Superconductors-A Hint for d-Wave Superconductivity," *Journal of The Physical Society of Japan*, vol. 61, no. 12, pp. 4283–4286, 1992.

[31] K. Nelson, Z. Mao, Y. Maeno, and Y. Liu, "Odd-parity superconductivity in $Sr_2RuO_4$," *Science*, vol. 306, no. 5699, p. 1151, 2004.

[32] A. Barone and G. Paternò, *Physics and Applications of the Josephson Effect*. John Wiley and Sons, 1982.

[33] B. Josephson, "Supercurrents through barriers," *Advances in Physics*, vol. 14, no. 56, pp. 419–451, 1965.

[34] A. Mathai, Y. Gim, R. Black, A. Amar, and F. Wellstood, "Experimental Proof of a Time-Reversal-Invariant Order Parameter with a $\pi$ shift in $YBa_2Cu_3O_{7-\delta}$," *Physical review letters*, vol. 74, pp. 4523–4526, 1995.

[35] A. Bouhon and M. Sigrist, "Influence of the domain walls on the Josephson effect in $Sr_2RuO_4$," *New Journal of Physics*, vol. 12, 2010.

[36] M. Sigrist, T. Rice, and K. Ueda, "Low-field magnetic response of complex superconductors," *Physical review letters*, vol. 63, no. 16, pp. 1727–1730, 1989.

[37] Z. Q. Mao, Y. Maeno, and H. Fukazawa, "Crystal growth of $Sr_2RuO_4$," *Materials Research Bulletin*, 2000.

[38] J. D. Strand, D. J. Bahr, D. J. Van Harlingen, J. P. Davis, W. J. Gannon, and W. P. Halperin, "The Transition Between Real and Complex Superconducting Order Parameter Phases in $UPt_3$," *Science*, vol. 328, no. 1368, 2010.

[39] J. Strand, *Determining the Superconducting Order Parameter of $UPt_3$ With Josephson Junction Interferometry*. PhD thesis, University of Illinois at Urbana-Champaign, 2010.

[40] Z. Jiang, J. Aumentado, W. Belzig, and V. Chandrasekhar, "Transport through ferromagnet/superconductor interfaces," *Theory of Quantum Transport in Metallic and Hybrid Nanostructures*, pp. 57–66, 2006.

[41] M. Sigrist and D. F. Agterberg, "The Role of Domain Walls on the Vortex Creep Dynamics in Unconventional Superconductors," *Progress of Theoretical Physics*, vol. 102, no. 5, 1999.

[42] C. Kallin and A. Berlinsky, "Is $Sr_2RuO_4$ a chiral p-wave superconductor?," *Journal of Physics: Condensed Matter*, vol. 21, p. 164210, 2009.